Power Output Assessment of TetraSpar Floating Demonstrator

A Comparative Analysis between Actual Performance and Model Predictions

Master Thesis Report

Georgios Kotsiras

September, 2024

TU Delft Delft University of Technology

RWE

Power Output Assessment of TetraSpar Floating Demonstrator

A Comparative Analysis between Actual Performance and Model Predictions

by

Georgios Kotsiras

to obtain the degree of Master of Science in Sustainable Energy Technology
at Delft University of Technology.

Wind Energy Group, Faculty of Aerospace Engineering, Delft University of Technology
Faculty of Electrical Engineering, Mathematics and Computer Science, Delft University of Technology
Resource Assessment Delivery, RWE Offshore Wind Netherlands B.V.

Student number: 5729556
Project duration: December, 2023 – September, 2024
Supervisors: Prof. dr. ir. Axelle Viré, TU Delft
Justin Burstein, RWE

Cover: TetraSpar Demonstrator in full operation (Photo credit: The TetraSpar Demonstrator Project ApS)

TU Delft

RWE

Acknowledgments

This thesis report was written as the final step to obtain the Master of Science in Sustainable Energy Technology at Delft University of Technology. During the project, I expanded my knowledge in the field of floating offshore wind turbines. For the completion of this project, I would like to express my gratitude to all who contributed to it.

Firstly, I would like to thank RWE for giving me the opportunity to work on such an innovative project as the TetraSpar demonstrator. Specifically, I extend my heartfelt thanks to my daily supervisor, Justin Burstein, for sharing his knowledge with me, guiding me and providing invaluable feedback. It was a great experience working with him.

Secondly, I would like to thank my university supervisor, Prof.dr.ir. Axelle Viré, for her invaluable guidance and support throughout the project. Her insights and advice were instrumental in shaping the direction and outcome of this research.

Lastly, I would like to express my deepest gratitude to my family and friends who have supported me throughout my studies at TU Delft. Their encouragement and support were crucial in helping me achieve this milestone.

Thank you all.

Georgios Kotsiras
Delft, September 2024

Abstract

In recent years, the use of renewable energy sources has increased significantly. As a result, offshore wind energy has expanded due to its advantages compared to onshore, such as steadier winds, reduced visual impact and lower noise emissions. However, 80% of the global offshore wind resource potential is located in areas with water depths greater than 60 meters, making the installation of fixed-bottom wind turbines unfeasible and leading to an increase in floating wind turbines. Floating offshore wind turbines, due to their increased freedom of movement, experience more complex aerodynamic and hydrodynamic phenomena, resulting in different power generation compared to fixed-bottom wind turbines. The effect of six degrees of freedom on power production has not been extensively studied in full-scale operating wind turbines. Additionally, a better prediction of energy production could also reduce the investment risk of floating wind turbines, leading to a reduced levelised cost of energy and better integration of floating wind turbines into a fully renewable energy system.

The aim of this report was to investigate the power generation and response of the TetraSpar demonstrator project, the world's first fully industrialised floating offshore foundation. To achieve this, a model of the TetraSpar demonstrator was created in OpenFAST. Due to confidentiality, some data, particularly regarding the wind turbine, were unavailable and were instead based on scaling the NREL 5 MW wind turbine. In addition, the ROSCO controller was incorporated into the model and the floating platform was modelled as a six degrees of freedom rigid body.

For the validation of the OpenFAST model, a comparison was performed with the on-site TetraSpar demonstrator. Data for the on-site demonstrator regarding motions, metocean conditions and power generation were provided by RWE. Further filtering and averaging the data in 10-minute periods for an entire year was performed. First, three one-hour simulations were performed for three different operating conditions: cut-in, below rated and above rated. Results from time series and power spectral density analyses showed a good agreement in platform motions. For the generated power, the mean average produced power was closest to the on-site data in the above rated region.

Next, for the power curve and AEP estimation, the probability of occurrence for each wind speed in the operating region was determined based on the on-site measured data. Furthermore, for every wind speed, the most representative significant wave height, wave period, turbulence intensity and other parameters needed as inputs in OpenFAST were found. The results showed that the AEP predicted by OpenFAST was 2.8% lower than the AEP measured at the on-site TetraSpar demonstrator. Moreover, different peak shaving levels of the controller contributed to the AEP percentage difference, ranging from about 4.4% to 2.1% compared to the on-site measurements. As far as platform motions are concerned, the model showed good agreement, capturing the trend of mean values and standard deviations of the two most dominant motions in power production, surge and pitch. In addition, the effect of wave height and wave period showed that the mean generated power is slightly affected. Similar results were also found for different current velocities. However, waves were found to influence the oscillation amplitudes of surge and pitch motions, while currents mainly affected the shift in mean values. Lastly, wind-wave misalignment also proved to have a negative effect on power performance.

In conclusion, the current OpenFAST model can be used to estimate the energy production and platform motion of the TetraSpar demonstrator. However, further improvements and reduction of the assumptions made, mainly due to the unavailability of data because of confidentiality, could enhance its accuracy.

Contents

List of Figures

List of Tables

List of Abbreviations

Abbreviation	Definition
AEP	Annual Energy Production
BEM	Blade Element Momentum
CAGR	Compound Annual Growth Rate
CFD	Computational Fluid Dynamics
CoG	Centre of Gravity
DBEM	Dynamic Blade Element Momentum
DOF	Degrees of freedom
FFT	Fast Fourier Transform
FOWT	Floating Offshore Wind Turbine
JONSWAP	Joint North Sea Wave Project
LCOE	Levelised Cost of Energy
MWL	Mean Water Level
NREL	National Renewable Energy Laboratory
OLAF	cOnvecting LAgrangian Filaments
PSD	Power Spectral Density
RNA	Rotor Nacelle Assembly
TI	Turbulence Intensity
TLP	Tension Leg Platform
TSR	Tip Speed Ratio

1

Introduction

In chapter 1 the current status of offshore wind energy and the various types of offshore wind turbines are presented. Following this, the research motivation, objectives and the methods used in the thesis report are described. Finally, the layout of the report is presented.

1.1. Current offshore wind energy status

In recent years, the rising energy demand and the signing of the Paris Agreement's target to reduce the greenhouse gas emissions by 43% by 2050 (United Nations, 2015), have driven a substantial surge in renewable energy sources and their integration into the current energy mix. As a result, wind energy, both onshore and offshore, has seen significant growth over the past few years. According to GWEC (2023a), the total installed wind capacity in 2022 was 906 GW. From this, the total offshore wind capacity reached 64.3 GW, making 2022 the second year with the largest number of wind turbine installations since the beginning of offshore wind. It is expected that 380 GW of offshore wind energy will have been installed by 2032, leading to a total installed capacity of 447 GW (GWEC, 2023b).

The 80% of global offshore wind resource potential is located in areas with a water depth more than 60 meters. However, fixed-bottom wind turbines are not feasible in these water depths (O'Kelly & Arshad, 2016). This will lead to an increase in floating offshore wind projects in the future as can be seen also by Figure 1.1, where CAGR is the compound annual growth rate.

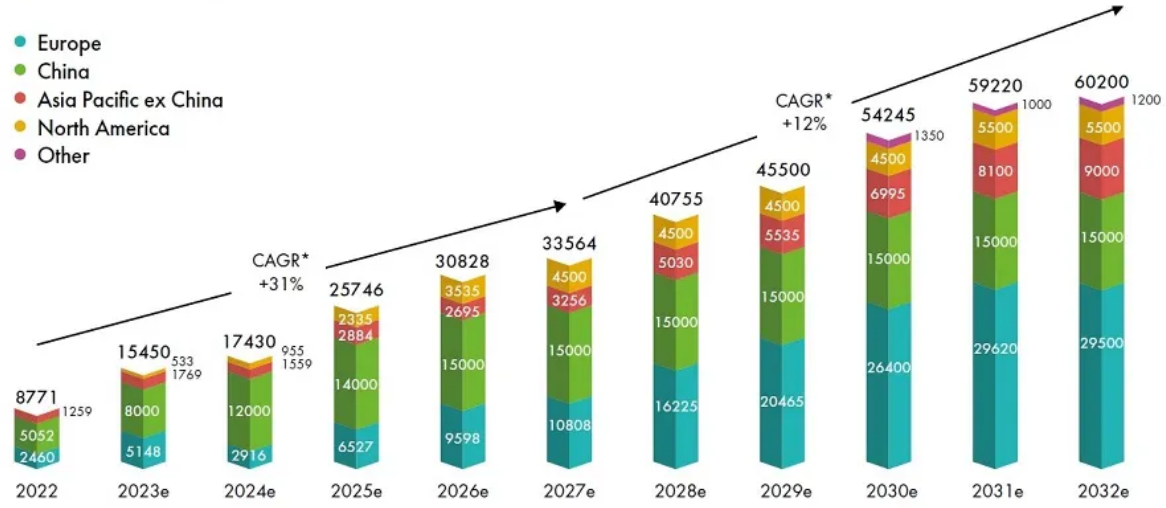

Figure 1.1: New global offshore wind installations in MW (GWEC, 2023a).

The cumulative capacity of floating offshore wind reached 187.8 MW in 2022, constituting 0.3% of the total installed offshore wind capacity. In 2022, 66.4 MW were added to the global floating offshore wind capacity, primarily concentrated in Norway with 60.2 MW, while China contributed an additional 6.2 MW. Projections from the GWEC (2023b) anticipate a significant surge, with an expected increase to 18.9 GW by 2030.

1.2. Offshore wind turbines

Offshore wind turbines have more advantages when compared to onshore wind turbines, such as steadier winds, less visual impact and flexible acoustic noise requirements (Barooni et al., 2023). Specifically, the sea surface is considerably smoother than the ground, resulting in offshore wind turbine rotors experiencing a more consistent wind speed compared to their onshore counterparts. Additionally, offshore wind tends to be stronger, allowing offshore turbines with the same rotor diameter to harness more wind energy than onshore turbines. Unlike onshore wind turbines, offshore installations are comparatively free from constraints such as visual impact and noise emissions, as they are positioned in the open sea, away from populated areas (Shen et al., 2018). As a result, placing wind turbines at a considerable distance from the shore can mitigate issues commonly associated with onshore wind turbines (Schallenberg-Rodríguez & Montesdeoca, 2018).

1.2.1. Fixed offshore wind turbines

As far as the fixed offshore wind turbines are concerned, there are three different types: monopile, tripod and jacket, as can be seen in Figure 1.2.

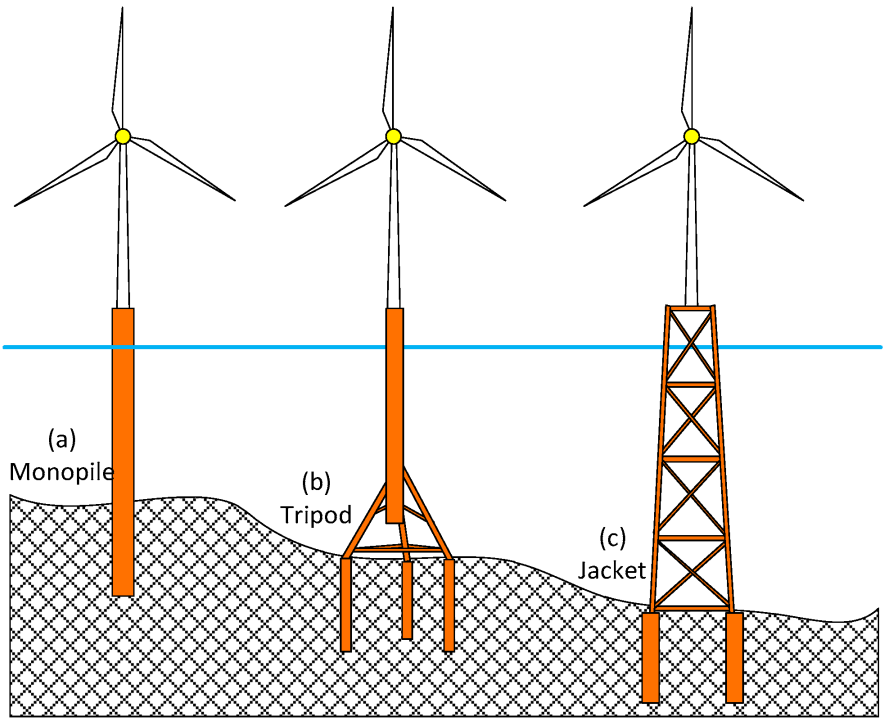

Figure 1.2: Different types of fixed offshore wind turbines: (a) Monopile, (b) Tripod, (c) Jacket (Plodpradit et al., 2019).

The monopile serves as the most commonly employed foundation for wind turbines, particularly in shallow water depths (<40 m). Its uncomplicated design and the absence of a need for seabed preparation confer the advantage of quick installation, often completed within 24 hours (Fischer et al., 2011). Conversely, tripod substructures are employed for larger wind turbines situated in deeper waters. These foundations feature three-legged tripod bases connected to a central steel tubular section with a large diameter, providing additional stability to the wind turbine. However, the construction time is extended and can take up to 2-3 days (Byrne & Houlsby, 2003).

In the development of offshore oil and gas platforms operating at depths of up to 60 meters, a common preference is given to the use of jacket or braced frame substructures (Koh & Ng, 2016). The jacket structure, characterised by a lattice truss with slender components connected by three or four tubular legs, is strategically secured into the seabed. Its notable advantages lie in its suitability for challenging offshore conditions, offering superior resistance to prevailing ocean waves and currents compared to monopile or tripod structures. However, there are drawbacks, including higher installation and construction expenses, categorising it as a substructure suitable for transitional waters. Additionally, extended maintenance periods are necessary to counteract erosion (Seidel, 2007). To sum up, there are different types of fixed offshore wind turbines, each suitable for varying water depths and weather conditions. However, as water depth increases and conditions become harsher, the costs associated with fixed-bottom wind turbines also increase.

1.2.2. Floating offshore wind turbines

Since the first prototype of a FOWT in 2007, there has been a rapid expansion up to the present. This is evident from Figure 1.3, which presents FOWT prototypes, demonstrators and farms. It is clear that the range of floating offshore wind turbine platforms is very broad, without a dominant specific type of foundation. When the technology matures sufficiently and there is convergence toward specific types of FOWTs, costs will also be reduced (Edwards et al., 2023). Due to the investments in the field of FOWTs, the levelised cost of energy (LCOE) for floating wind turbines is anticipated to decrease to 40–60 €/MWh by 2030 (Micallef & Rezaeiha, 2021).

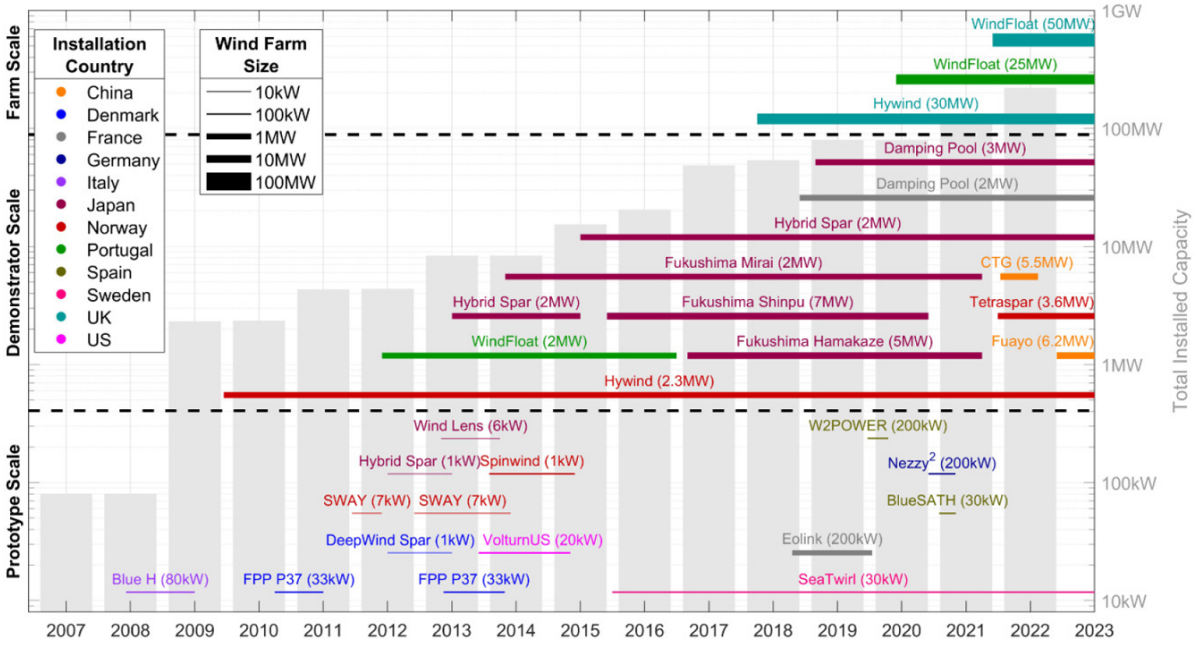

Figure 1.3: Timeline of floating offshore wind turbine deployments, including prototypes, demonstrators and farms (Edwards et al., 2023).

In recent years, different types of FOWTs with different support platforms, anchoring and mooring configurations have been proposed and investigated. According to Collu and Borg (2016) three primary methods are employed to enhance pitch stabilisation in offshore wind platforms. These include increasing the separation between the vertical center of buoyancy and the vertical center of gravity (gravity-stabilised), augmenting the pitch second moment of the waterplane area (waterplane-stabilised) and utilising taut moorings (mooring-stabilised). Platforms are typically categorised into four main types based on their stability approach: spar (gravity-stabilised), barge, semi-submersible and tension leg platform (TLP), as illustrated in Figure 1.4.

Spars utilise gravity stabilisation, featuring a single vertical cylinder with ballast at the bottom and a directly connected wind turbine tower. In contrast, TLPs rely on mooring stabilisation, with a submerged body connected to mooring lines and a central column linking the submerged body to the wind

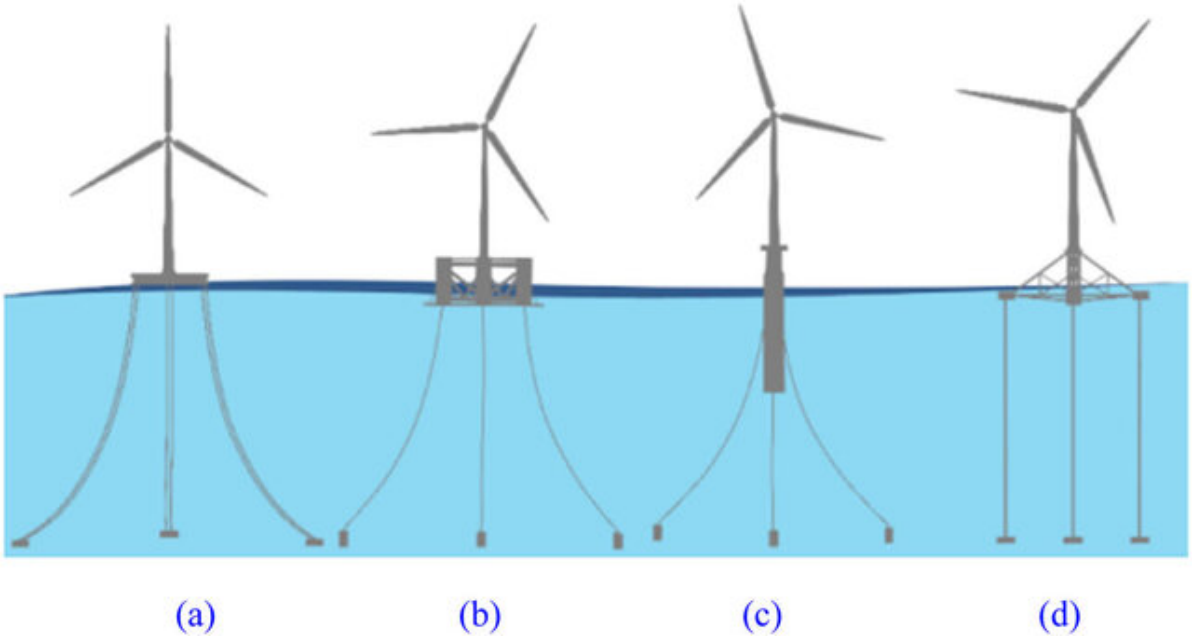

Figure 1.4: Different FOWT design concepts: (a) barge, (b) semi-submersible, (c) spar and (d) TLP (Adiputra et al., 2023).

turbine tower above the surface. Barges employ waterplane stabilisation, characterised by a shallow floating, wide platform. Semi-subs, on the other hand, combine waterplane and gravity stabilisation, often composed of three to five interconnected vertical cylinders, with the turbine centrally located or positioned above one of the columns.

1.3. Research motivation

Floating wind farms are being developed throughout the world and the number of megawatts under development is growing rapidly (GWEC, 2023b). To justify the capital investment required to build these wind farms, reliable predictions of energy volumes generated are crucial. However, compared to fixed-bottom wind turbines, in FOWTs there are more complex aerodynamic phenomena due to motions of the platform causing variations in loads (Micallef & Rezaeiha, 2021). The inherent flexibility of the floating platform brings about six degrees of freedom (DOF) in motion, encompassing three displacements (surge, heave, sway) and three rotations (pitch, roll, yaw). These extra platform movements are subsequently transmitted to the wind turbine rotors, potentially undergoing amplification. This introduces a heightened level of unsteadiness and complexity to the aerodynamics of the wind turbine when compared to fixed-bottom counterparts (Shen et al., 2018). For this reason, the understanding of how power production differs from a fixed-bottom turbine is a great challenge.

The industry has identified a variety of effects which could change power production of FOWTs such as the platform pitch motion (Wen et al., 2018) and the controller tuning (Abbas et al., 2021). In order to model these effects, different tools have been developed, ranging from modifications of existing wake models to simple Excel sheets. Various groups have done validations of these tools with both higher fidelity models and scale testing in wave tanks. However, validation on full scale operating turbines has not been performed to any large extent.

In this context, the methodology and results presented in this project aim to expand knowledge in the field of FOWTs and reduce their costs. By developing a model for the TetraSpar floating demonstrator, which enhances the understanding of its dynamics and can predict the annual energy yield at specific locations and operating conditions, this project is crucial for reducing investment risks. This advancement could contribute to the maturation of FOWT technology, potentially lowering the costs of floating wind turbines to be competitive with other wind technologies (Wiser et al., 2021). To summarise, improved understanding and accurate power production estimation can lead to a reduction in the cost of energy.

In addition, for a fully renewable energy system with a high share of floating wind turbines, accurate prediction of energy production is essential. Given the intermittent nature of renewable energy sources such as wind and solar, integrating them into the grid poses challenges, including the need to store excess energy for periods of low production. Therefore, precise predictions of generated power are critical for effective system integration and grid management.

In summary, the motivation of this project is to expand the understanding of power production and response of FOWTs and to validate these aspects on a full-scale operating wind turbine, the TetraSpar demonstrator. Predicting the energy production of FOWTs could contribute to reducing the cost of energy and facilitate easier integration into a fully renewable energy system.

1.4. Research objectives

Based on the aforementioned motivation, this report aims to investigate the power performance of the TetraSpar floating demonstrator project. To gain a clearer understanding of the problem, it is crucial to address the following research questions:

- How can the TetraSpar demonstrator be effectively modelled and what assumptions should be employed for the unknown parameters?
- What is the impact of the six degrees of freedom on power generation and which of them has the most significant influence?
- How does the controller tuning affect platform stability and generated power of TetraSpar demonstrator?
- How do different environmental conditions, such as wind speed and sea state, affect the motion of the wind turbine and what is their collective influence on the generated power?

1.5. Research approach

In order to address the research questions, a well-structured methodology was employed. The first step involved conducting a literature review on the influence of motion on the power output of floating wind turbines. The results of these studies not only provided a better understanding but also highlighted areas that require further investigation.

Subsequently, a model of the TetraSpar demonstrator was developed in OpenFAST. This process entailed determining wind turbine characteristics, hydrodynamic coefficients and various other inputs that were fed into the OpenFAST model.

Following this, suitable test cases were identified at various wind speeds and sea states using TetraSpar on-site measured data, ensuring that all relevant instrumentation was operational and the turbine was not curtailed. The data obtained from these tests were processed to determine power output.

The final step involved comparing the test cases to the predictions of the same conditions from the OpenFAST model, conducting a critical analysis and interpretation of the results.

1.6. Report layout

The thesis report follows the structure outlined below. A detailed description of the TetraSpar demonstrator is presented in chapter 2, while chapter 3 conducts a thorough literature review to identify the influence of platform motion and different weather conditions on the response and power production of FOWTs. Following this, chapter 4 presents the basic offshore wind background theory and the modules used by OpenFAST for the modelling. Next, chapter 5 analyses the methodology behind the development of the TetraSpar in OpenFAST. In chapter 6, the response of the model and the power output under different sea states and wind conditions, along with a comparison with on-site measured data, is presented. Then, chapter 7 investigates the impact of waves and currents on the TetraSpar motion and power production. Lastly, chapter 8 demonstrates conclusions and recommendations for future investigation.

2

TetraSpar demonstrator overview

In this chapter, a detailed description of the TetraSpar demonstrator is provided. In section 2.1, the design concept of the demonstrator is described. Next, in section 2.2, an overview of the global system is presented, while in section 2.3, analytical description and properties of the foundation and the wind turbine parts are provided. Lastly, section 2.4 describes the different measurement units used to define the motion and power output of the TetraSpar.

2.1. TetraSpar design philosophy

The TetraSpar demonstration project is the world's first full-scale demonstration of an industrialised offshore foundation (Stiesdal, 2021). The main principle guiding the TetraSpar concept (Figure 2.1) revolves around utilising components highly suitable for large-scale industrial production. In both onshore and offshore wind energy sectors, reducing the cost of tower structures has been significant in reducing the LCOE. This reduction in cost has been achieved through large volume and standardised designs, facilitating investments in highly industrialised production facilities.

In order to achieve similar cost in the floating offshore wind industry, it's essential for any concept to minimise labor-intensive tasks or onshore production requirements (Borg et al., 2020). Instead, all welding and coating processes should occur in controlled factory settings with automation to ensure precision and safety. The TetraSpar concept meets this requirement by constructing modules that are ready for assembly upon arrival at the port, utilising existing workforce expertise in wind turbine tower assembly. This means that assembly complexity is kept at or below that of wind turbine towers, primarily relying on bolt and pin connections. Furthermore, the modularity of the TetraSpar concept allows for the utilisation of currently used logistics practices within the wind energy sector. Last but not least, one important factor is that none of the foundation elements exceed the dimensions of the wind turbine itself, ensuring compatibility with existing delivery methods.

The TetraSpar platform combines spar-like stability suited for 100-1000+ meter water depth, with a very low center of gravity without requiring deep water ports. This is achieved by a hull at the water's surface that supports a 3.6 MW wind turbine and a keel suspended below the main body. The hull consists of ten cylinders while the keel of three. The lower keel has a notably dense structure, contributing to the overall platform's lowered center of gravity. These cylinders are interconnected to create a tetrahedral shape and are anchored to the seabed using three catenary lines attached to the ends of the radial elements. When assembled in port using quayside cranes, the keel can be partially deployed, enabling access to a wider range of potential ports. In addition, all parts of the foundation were manufactured offsite with industrialised processes reducing manufacturing hours by 85-90%. The TetraSpar consists of readily manufacturable tubular steel members that with no welding or other special processes used during assembly.

The port of Grenaa in Denmark was chosen as the construction site for the TetraSpar foundation. The TetraSpar foundation components were manufactured at the facilities of the wind turbine tower manufacturer and were transported to the port over the summer 2020 and assembly took place in

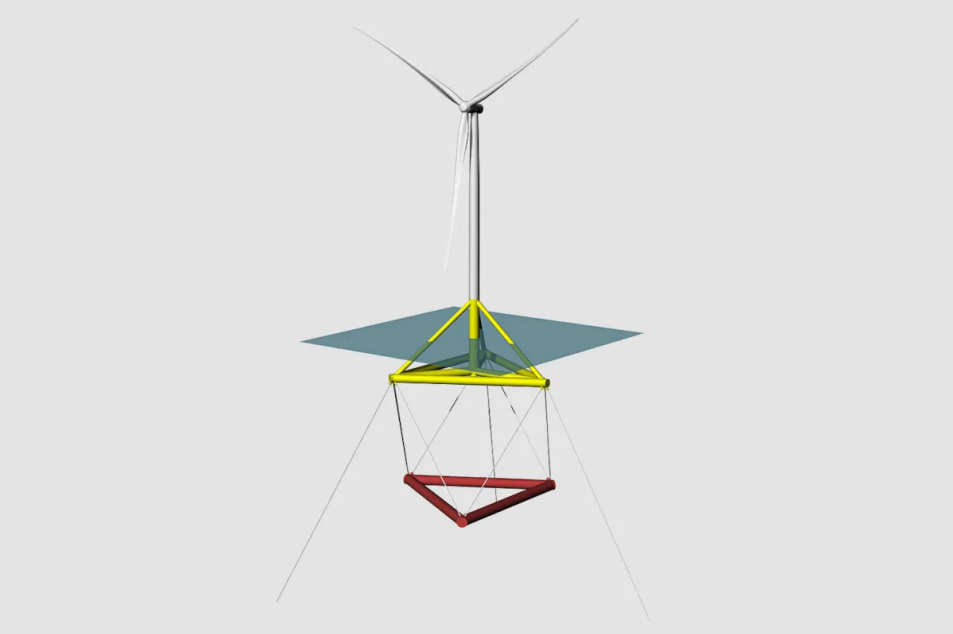

Figure 2.1: The TetraSpar demonstrator concept (Borg et al., 2020).

October and November 2020. The TetraSpar floater was moored 10 kilometres offshore (220 m depth) at the Marine Energy Test Centre in the North Sea, off the island of Karmøy on the western coast of Norway—approximately 1500 m north-west of the Equinor Hywind Demo. Commissioning was completed November 29, 2021, and the TetraSpar demonstrator has been in full operation since then.

2.2. Global system overview

As has been described, the floating platform consists of the floater and the keel which is suspended below the floater with six suspension lines. The platform is moored to the seabed with a catenary mooring system. An overview of the system with the centre of gravity for the different components is presented in Figure 2.2, while in Table 2.1 the overall properties of global system are presented.

This setup essentially makes the TetraSpar behave like a typical spar, providing strong buoyancy and stability thanks to the ballast in its keel. By adjusting the weight and depth of the keel, the overall performance of the system can match specific design requirements. On the following sections, a detailed description of all the components is presented.

Table 2.1: Overall properties of the global system (Borg et al., 2020).

Item	Unit	Value
Overall mass including ballast	(t)	5471
Overall vertical center of gravity below MWL	(m)	40.0
Draft	(m)	66.0
Height of foundation-tower interface above MWL	(m)	16.0

2.3. Components description

In this section a detailed description of the floater, keel, suspension system, mooring lines and wind turbine is presented. The mechanical and structural properties are used as inputs in the OpenFAST model.

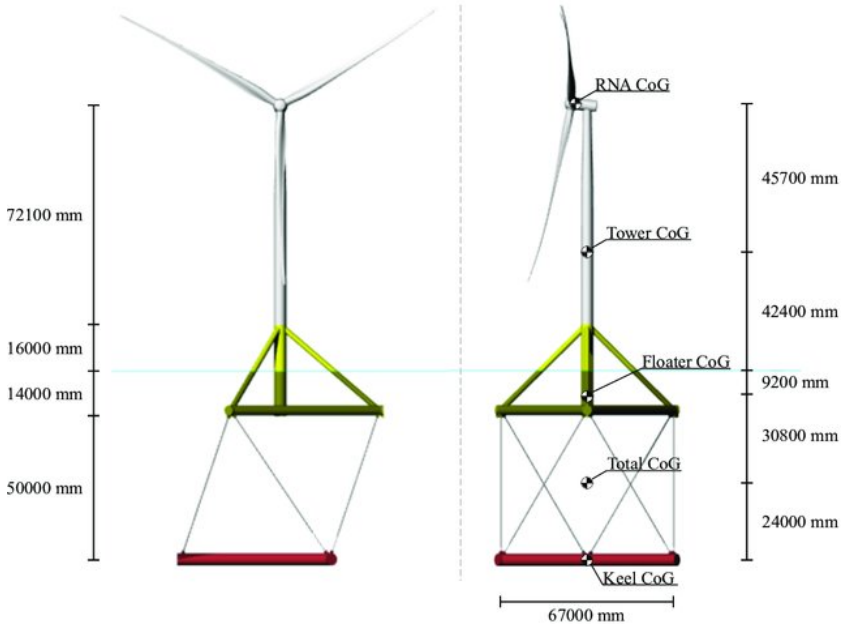

Figure 2.2: TetraSpar structure (left) and centre of gravity (right) (Borg et al., 2020).

2.3.1. Floater

As far as the floater is concerned (Figure 2.3), it consists of of ten steel tubes. There is one vertical column where three horizontal radial braces are connected close to its base, oriented 120 degrees from one another. At the outer end of each of these radial braces, a diagonal brace is connected to the central column. Further, adjacent radial braces outer ends are connected by lateral braces. These elements are terminated in cast nodes and conically tapered where applicable. All nodes are connected with shear loaded pin connections in order to mitigate the risk of possible errors in works related to bolt tension. The overall properties of the floater are presented in Table A.1, while the definition and the position of each component are listed in Table A.2. The conically tapered ends are converted into constant cylinders providing similar buoyancy of the entire element. The floater is equipped with boat landing, platforms, wind turbine components, etc., all included in the mass defined in Table A.1.

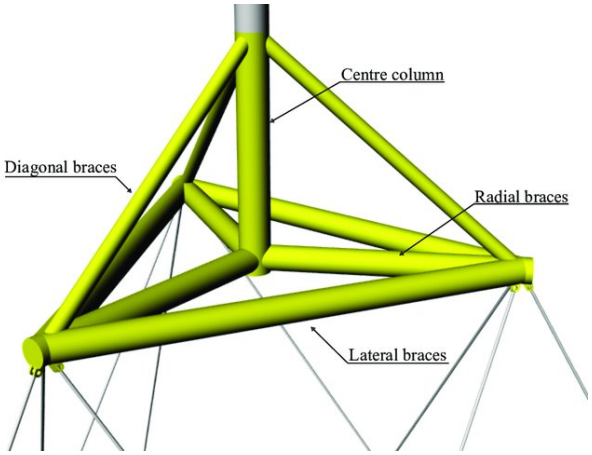

Figure 2.3: Floater components (Borg et al., 2020).

2.3.2. Keel

The keel is composed of three identical cylinders arranged in a triangular configuration, as depicted in Figure 2.4. Like the components of the floater, the cylinders in the keel are tapered conically, but for

simplicity, they are represented as constant cylinders. The overall characteristics of the keel system are detailed in Table A.3, along with descriptions of each individual cylinder.

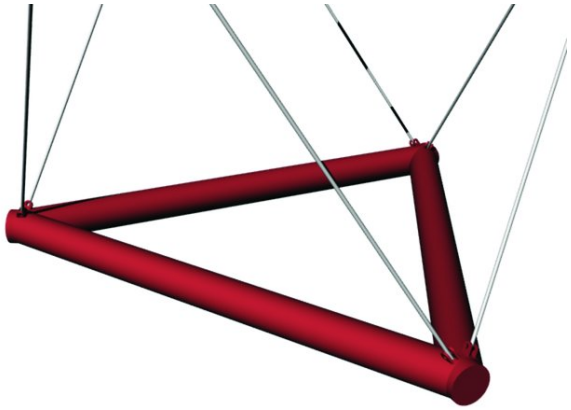

Figure 2.4: Keel of the TetraSpar (Borg et al., 2020).

In order to suspend the keel from the floater, six lines are used. Each line is comprised of a cluster of synthetic ropes. The mechanical properties of suspension lines and the position of them are presented in Table A.4.

2.3.3. Mooring system

The TetraSpar demonstrator employs a conventional 3-line spread mooring system to maintain its position. As can be observed from Figure 2.5, which illustrates the catenary of the mooring line in the static state, each mooring line consists of four different types of lines which are connected together in order to create a six segment line.

Detailed information about the mooring system and the mechanical properties of the mooring lines can be found in Table A.5 and Table A.6, respectively. Due to the prevailing environmental load directions, the mooring lines are distributed unevenly.

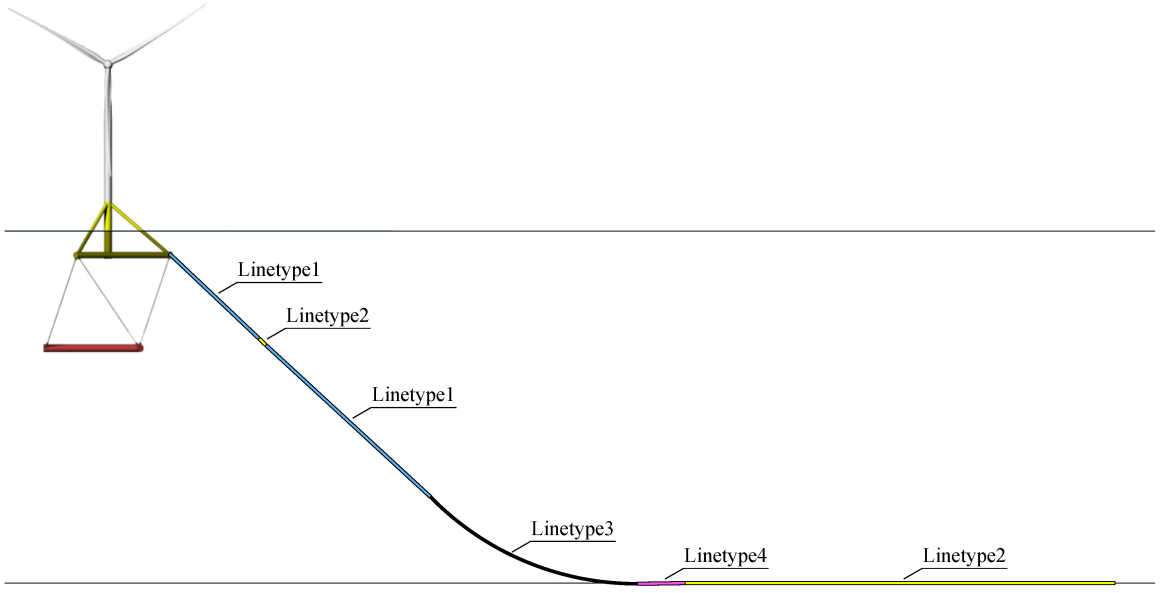

Figure 2.5: Segments of mooring line (Borg et al., 2020).

It is important to note that the orientation of the total mooring system and floater in the tables does not align with their actual onsite orientation. The actual orientation cannot be published due to confidentiality reasons. However, in the development of the model in OpenFAST the actual on-site orientation was used for a more accurate comparison with measured data.

2.3.4. Wind turbine

The TetraSpar demonstrator is equipped with a wind turbine with nominal rated power of 3.6 MW and rotor radius 130 m. More information about the analytical description of the RNA is not publicly available, except for those presented in Table 2.2.

Table 2.2: Wind turbine properties (Borg et al., 2020).

Item	Unit	Value
Tower base above MWL	(m)	16.0
Rotor and nacelle (RNA) mass	(t)	200.0
RNA CoG wrt. tower base	(m)	(3.75; 0.0; 72.1)
Total tower mass	(t)	235
Vertical tower CoG above tower base	(m)	26.4
Tower length	(m)	71.6
Tower roll moment of inertia wrt. CoG	($kg \cdot m^2$)	89.38×10^6
Tower pitch moment of inertia wrt. CoG	($kg \cdot m^2$)	89.38×10^6
Tower yaw moment of inertia wrt. CoG	($kg \cdot m^2$)	489.85×10^3
Tower base diameter	(m)	4.3
Tower top diameter	(m)	3.6

2.4. On-site measurement sensors

The TetraSpar floating demonstrator has been equipped with various measurement sensors to comprehensively observe its behavior. These instruments include devices for estimating wind conditions and sea states, such as as a LiDAR which is located on the nacelle, a wave radar located on the base of the tower (Singh et al., 2024) and wave buoys. Different sensors are utilised to measure displacements, accelerations and inclinations in six degrees of freedom. Additionally, various outputs from the wind turbine, along with other relevant parameters such as generated power, are continuously monitored. The data, are transmitted from all sensors to a central acquisition system, which stores the data at a frequency of 25 Hz (Singh et al., 2024).

The primary focus of this thesis is to investigate power production and the influence of different platform motions on it. Therefore, the data utilised will mainly include weather conditions, platform motions and wind turbine-related parameters, particularly those related to power production. All the other data that are not relevant to the project are not taken into consideration.

3

Literature review

The idea of floating offshore wind turbines was first introduced by Professor William E. Heronemus at the University of Massachusetts in 1972 (Musial et al., 2004). However it gained attention in the research community in the 1990s, and the first prototype was built in 2007 (Edwards et al., 2023). This chapter provides a detailed overview of previous studies on dynamic response and power production of FOWTs under different environmental conditions.

To begin with, in the study of Karimirad et al. (2012) the response of a spar-type floating offshore wind turbine was investigated under turbulent and steady wind speeds. It was revealed that turbulence does not significantly influence the mean power, but power fluctuations are increased. The most notable difference in mean power between turbulence and steady state is observed primarily at velocities below the rated wind speed. The average electrical power produced at the rated wind speed in the turbulent wind scenario was 4.1 MW, in contrast to the 5 MW output observed for the initial onshore wind turbine.

Farrugia et al. (2016) performed a study on the aerodynamics of a floating wind turbine rotor. For this reason, a comparison between power and wake characteristics of a FOWT with a fixed-bottom wind turbine was examined using advanced vortex methods. The NREL 5 MW reference wind turbine was used, mounted on a Tension Leg Platform (TLP). Due to the fact that surge motion is the most dominant on tension leg platforms, only this degree of freedom was investigated. The results revealed the occurrence of fluctuations in torque, with an increasing amplitude for increasing tip speed ratio. In addition, there is a linear connection between aerodynamic loading response amplitude and velocity amplitude in the direction of surge. As far as the power coefficient is concerned, it was found that compared to steady conditions, the power coefficient under floating conditions increases with surge frequency at high tip speed ratios and decreases at low tip speeds.

The performance of a 10 MW floating offshore wind turbine influenced by yaw and pitch motions was presented in the study of Leble and Barakos (2016). As expected, the results showed divergence in thrust and power for both motions compared to fixed wind turbines. However, for pitch motion, the differences in thrust and power were up to 32.8% while for yaw motion up to 2.5%, compared to fixed turbines (Figure 3.1).

Tumewu et al. (2017) investigated the influence of pitch motion on the power performance of three different floating offshore wind turbines (TLP, barge and semi-submersible) under three degrees of freedom (surge, heave, pitch). It was examined for wind speeds above rated and above-average wave loads. The simulations showed a clear connection of platform type to the steadiness of power output, with the semi-submersible performing the best and the barge platform being the worst as can be observed in Figure 3.2.

The primary objective of Wen et al. (2018) was to examine the power performance of the NREL 5 MW wind turbine based on an offshore platform, with a specific focus on pitching motion. A comparison was conducted solely for pitching motion, revealing an increase in power when the platform undergoes pitching motion compared to the fixed foundation case. Additionally, an increase in platform pitching

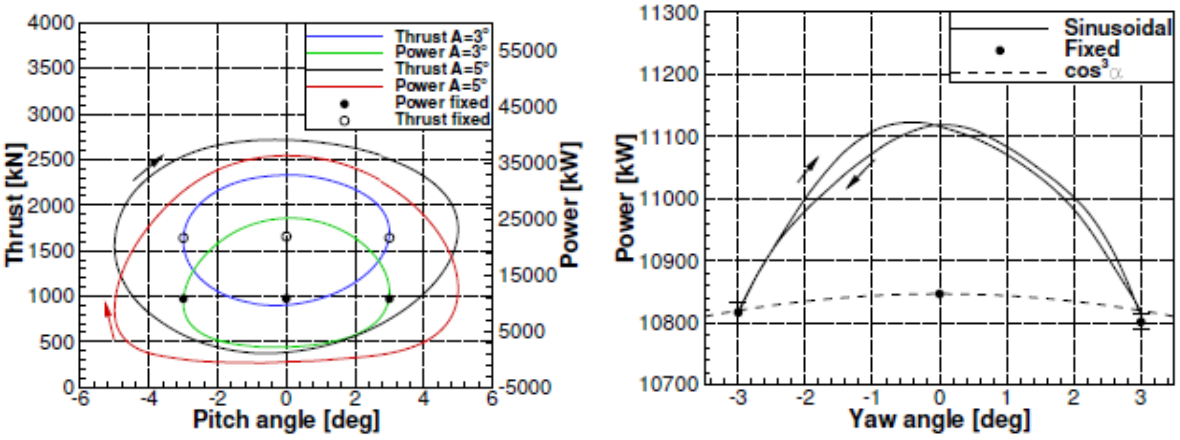

Figure 3.1: Thrust and power as function of pitching amplitude (left) and power as function of yaw angle (right) (Leble & Barakos, 2016).

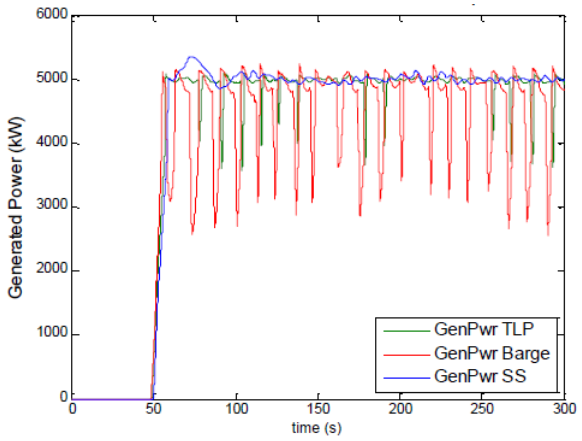

Figure 3.2: Power output for the different platforms under stochastic wave case (Tumewu et al., 2017).

amplitude and frequency was found to elevate mean power; however, this resulted in a reduction in power coefficient and power production fluctuation, as illustrated in Figure 3.3. Moreover, the fluctuation in power, which poses risks to power quality and FOWT component safety could be mitigated by configuring the FOWT to operate at lower tip speed ratios, related to lower power fluctuations. Additionally, optimising the FOWT platform is crucial to alleviate potential repercussions of excessive pitching motion.

Apart from the influence of pitch motion, Wen et al. (2017) also examined the influence of platform surge motion on power and thrust of a spar-type FOWT using the Free Vortex Method (FVM). Surge motion has a more significant effect on the angle of attack along the rotor blades than uniform wind velocity. Consequently, power and thrust depend on the angle of attack. An increase in the angle of attack is beneficial when there is no stall, but it is not advantageous for power output in stall conditions. A comparison with different frequencies and amplitudes of surge motions, as well as tip speed ratios, revealed that an increase in frequency or amplitude results in decreased power for low tip speed ratios and higher power output for larger tip speed ratios. Meanwhile, the mean thrust decreases for all tip speed ratios and the variations of both power and thrust increase, similar to Figure 3.3.

In the study of Shen et al. (2018), an unsteady lifting surface method with a free wake model is used to analyse the performance of the full-scale NREL 5 MW wind turbine under the surge motion of a floating offshore wind turbine. According to this study, pitch and surge are the most dominant degrees of freedom that influence the aerodynamic performance of a floating offshore wind turbine. The frequency of the aerodynamic power output and thrust response aligns with the frequency of surge motion. The results showed an increase of about 3% in power output of the FOWT compared to a fixed wind turbine

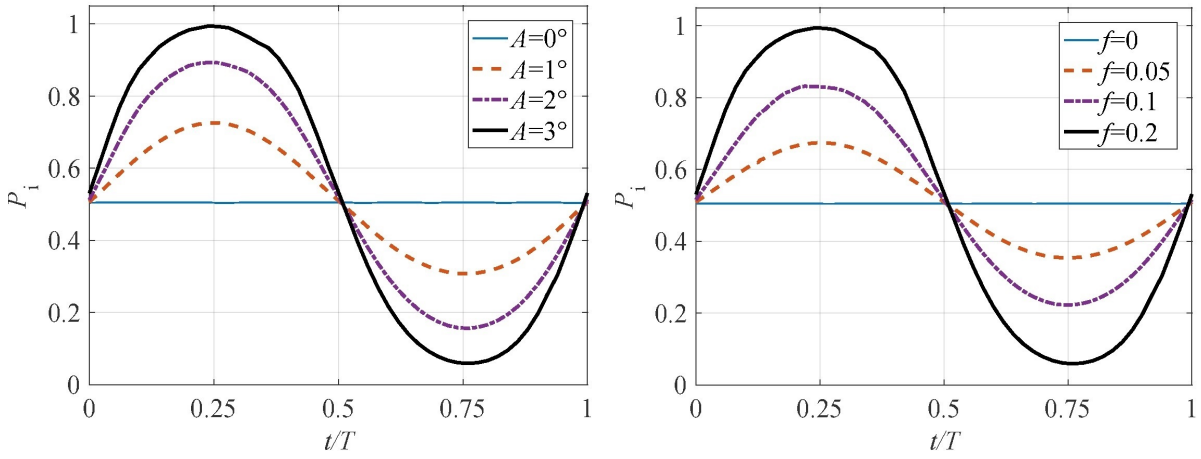

Figure 3.3: Time histories of the instantaneous power output P_i at different pitching amplitudes for $TSR = 7$ and $f = 0.2$ Hz (left) and for different pitching frequencies for $TSR = 7$ and $A = 3°$ (right) (Wen et al., 2018).

when working at rated or below rated conditions, if the blade pitch is kept constant and the blade is working under attached flow conditions (Figure 3.4). On the other hand, the thrust is decreased compared to a fixed turbine, but the large time-varying and frequency of rotor thrust have a negative influence on fatigue.

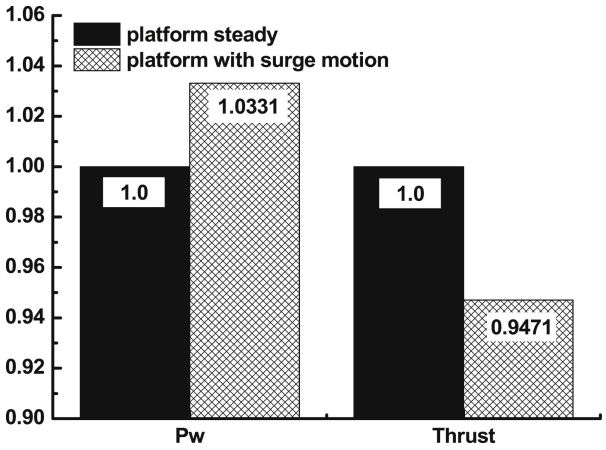

Figure 3.4: Comparison of the average power output and thrust between a steady platform and a platform with surge motion (Shen et al., 2018).

The influence of different wind and wave conditions on the energy yield and downtime of a spar-buoy floating wind turbine was investigated by Lerch et al. (2019). For this reason, the OC3-Hywind concept was examined using a Matlab model and compared with OpenFAST. For simplification, only surge, heave and pitch motions were taken into consideration. The two load cases used were for regular waves with steady wind speed and irregular waves with turbulent wind. The results showed a small power loss, less than 1% and 1.1% for the FOWT compared to a fixed-bottom wind turbine. This is verified by Figure 3.5, where the power curve of FOWT is almost identical to the power curve of fixed-bottom.

The main study of Lee and Lee (2019) was to investigate how the platform motions of a FOWT influence the wake evolution and aerodynamic performance. For this reason, the NREL 5 MW wind turbine was used and numerical simulations were performed using a nonlinear vortex lattice method (NVLM) coupled with a vortex particle method (VPM). As far as the power performance is concerned, calculations showed that only the pitch and surge motions have a significant influence on the power output (when one degree of freedom is used) because the wind velocities in these directions mainly influence the angle of attack, as can be observed in Figure 3.6. The aforementioned motions caused

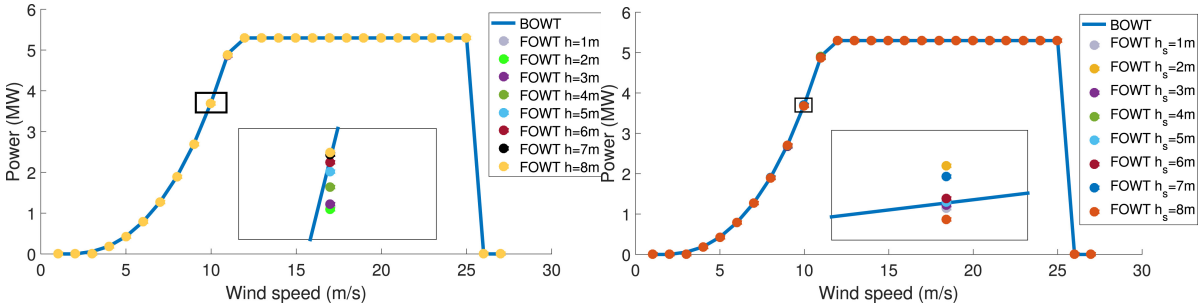

Figure 3.5: Power curve comparison between fixed-bottom (blue line) and FOWT (colored dots for waves with wave height (h)). Left: regular waves–steady wind. Right: Irregular waves–turbulent wind (Lerch et al., 2019).

oscillations in aerodynamic performance, with a frequency similar to the frequency of platform motions. In addition, numerical simulations of the wind turbine on three types of floating structures (spar-buoy, TLP, barge) with multiple degrees of freedom available showed that the barge structure has the most unsteady wind turbine performance.

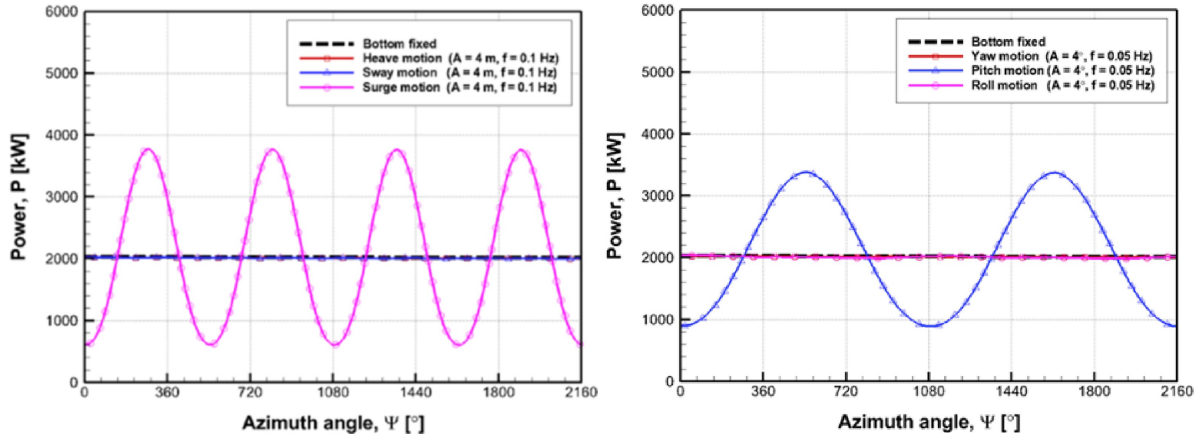

Figure 3.6: Variation in the power of a wind turbine in translational $A = 4\,\text{m}$ and $f = 0.1\,\text{Hz}$ (left) and rotational $A = 4°$ and $f = 0.05\,\text{Hz}$ (right) (Lee & Lee, 2019).

The study of Lyu et al. (2019) examined the dynamic response under different wind and wave conditions of the NREL 5 MW reference wind turbine supported by the OC3-Hywind spar-type platform, utilising FAST with WAMIT. The results indicated a connection between pitch and surge motions with wind and waves, particularly when the wind aligns with the surge direction. Additionally, the time domain investigation showed that pitch reaches its maximum when wind and waves share the same direction, while the other five degrees of freedom peak when they are perpendicular. The frequency domain analysis revealed the dependence of surge, pitch and heave motion on both wind and waves, whereas sway, roll and yaw motion are primarily influenced by waves.

Huang and Wan (2020) investigated the interference effects between a wind turbine and a spar-type floating platform under combined wind-wave excitation using CFD. The NREL 5 MW wind turbine and the OC3-Hywind spar platform were utilised for the study, examining the response of the FOWT in different platform motions (surge, heave, pitch and yaw). The results revealed that the surge velocity of the platform influences the local angle of attack, with the rotor power observed to be much more sensitive than the thrust, as can be observed in Figure 3.7. Additionally, the mean power output is reduced due to the large platform pitch angle when considering the shaft-tilt and prone-cone angle.

In addition, Johlas et al. (2021) investigated the effects of floating platforms on power generation. OpenFAST simulations were conducted for the NREL 5 MW reference turbine across three platform types: OC3-UMaine spar, OC4-DeepCWind semi-submersible and a fixed-bottom variant, considering weather conditions below rated wind speeds and extreme wave height. The results showed that power generation is decreased by rotor pitch angle and increased by upwind-downwind rotor motion caused

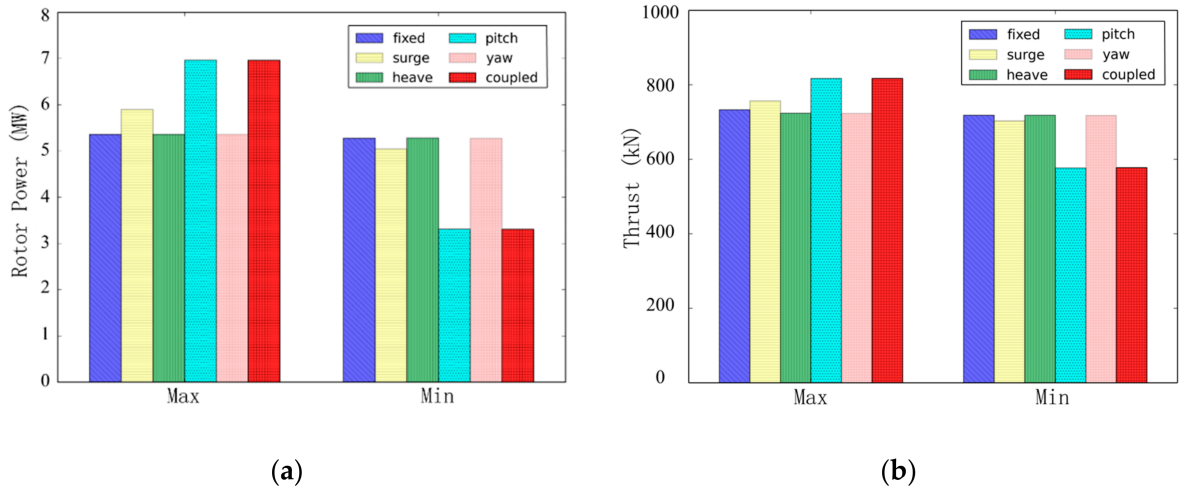

Figure 3.7: Comparison of the maximum and minimum values of rotor power (a) and thrust (b) between a fixed-bottom wind turbine and a FOWT under different platform motions (Huang & Wan, 2020).

by platform pitch and surge-pitch motions, respectively. The other platform motions (sway, heave, roll, yaw) do not significantly influence the power performance of the FOWT. The spar platform's lower center of mass results in more significant rotor motions dominated by pitch in the upwind-downwind direction. This dominance surpasses the impact of its rotor pitch angle, leading to a power gain ranging from 3.1% to 4.5% compared to a fixed-bottom wind turbine.

The study of Liu and Yu (2022) focused on examining the dynamic response of a spar-type floating offshore wind turbine under varying wave group conditions. It was observed that the presence of wave groups notably amplified the heave motion, with slight increases in surge and pitch motions compared to the scenario with irregular waves.

Wang et al. (2023) estimated the power output and loads on a 10 MW offshore wind turbine installed in monopile, spar and semi-submersible foundations. The comparison was conducted for different wind speeds, specifically below rated, rated and above rated wind speeds. The findings for power performance are summarised in Figure 3.8. The mean power performance of the three offshore wind turbines does not exhibit significant differences under the three different conditions. However, the standard deviation of the spar wind turbine is much larger in rated and above rated conditions. This is attributed to the larger platform pitch motion.

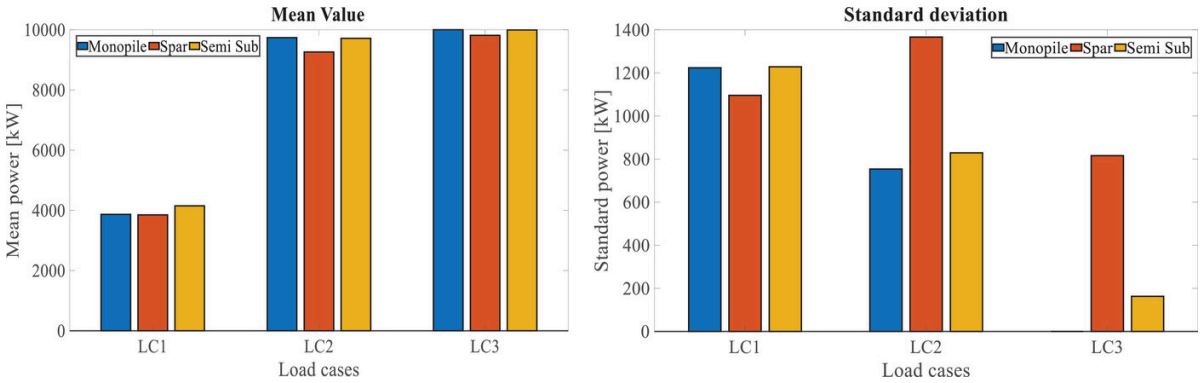

Figure 3.8: Power production of the monopile, spar and semi-submersible wind turbines. Left: Mean values. Right: Standard deviations (Wang et al., 2023).

Last but not least, Ramponi et al. (2023) investigated the mean power produced by a wind turbine under the influence of the following coupled motions: pitch-surge, pitch-yaw and surge-yaw. This examination was conducted both with and without a controller. It was observed that when the controller

is active, the produced power is reduced due to the effects of platform motions. Additionally, in pitch-yaw and surge-yaw configurations, pitch and surge motions were predominant over yaw, attributed to their alignment with the incident wind.

To summarise, studies on the effect of platform motions and weather conditions on the power output of FOWTs were presented in this chapter. To understand the dynamics of FOWTs, different methods have been employed, such as vortex methods, CFD and software like OpenFAST. It was found that surge and pitch are the motions with the highest impact on power generation. Additionally, turbulence influences power fluctuations, but the mean power remains unaffected. Furthermore, the platform type also affects the stability of FOWTs. Lastly, as far as the influence of waves is concerned, results showed that regular and irregular waves cause small power losses compared to fixed-bottom wind turbines, with platform surge and pitch motions closely linked to wave conditions, especially when wind and waves are aligned.

4

Theoretical background and OpenFAST theory

In chapter 4, the theoretical background for FOWTs relevant to this project is presented, followed by an explanation of the OpenFAST modules used for modelling the TetraSpar demonstrator.

4.1. Theoretical background

Compared to fixed-bottom wind turbines, there are more complex aerodynamic phenomena due to motions of the platform, causing variations in loads. The potential cycling between the wind turbine and propeller states during pitching motion, and the intermediate flow conditions, poses operational and modelling challenges for FOWTs (Leble & Barakos, 2016). Consequently, due to the increased degrees of freedom, FOWTs exhibit strong coupling between aerodynamics, hydrodynamics, aeroelasticity, control, material science, structural engineering and soil mechanics.

4.1.1. Platform motions

In general, when considering spar-type floating offshore wind turbines, they are typically assumed to experience rigid body motions. A coordinate system is established with its origin located at the center of gravity of the whole structure, where challenges related to hydrodynamics arise. These rigid motions involve six degrees of freedom, encompassing three translational and three rotational DOFs. The translational DOFs involve movement along the x, y and z axes, while the rotational DOFs entail rotation around these axes. Specifically, the translational DOFs include motion in surge, sway and heave, while the rotational DOFs encompass roll, pitch and yaw, as presented in Figure 4.1.

For the motion response of a spar FOWT modelled as rigid body, the Equation 4.1 is used, which is based on Newton's second law of motion (Matha et al., 2016):

$$\begin{bmatrix} M(s) \\ M(a) \\ M_{\text{WT}} \end{bmatrix} \ddot{x} + \begin{bmatrix} C(s) \\ C_{\text{WT}} \end{bmatrix} \dot{x} + \begin{bmatrix} K(s) \\ K_{\text{WT}} \\ K_{\text{mooring}} \end{bmatrix} x = F(x) \tag{4.1}$$

where $M(s)$ is the platform structure mass matrix, $M(a)$ is the additional mass matrix, M_{WT} is the wind turbine mass matrix, $C(s)$ is the platform structure damping matrix, C_{WT} is the wind turbine damping matrix, $K(s)$ is the platform structure stiffness matrix, K_{WT} is the wind turbine stiffness matrix, K_{mooring} is the mooring system stiffness matrix and $F(x)$ the external forces acting on the FOWT, as given by Equation 4.2. The motion vector x represents the displacements in each degree of freedom, while the derivatives $\dot{x}$ and $\ddot{x}$, the velocities and accelerations, respectively.

$$F(x) = F_{\text{hydrostatics}} + F_{\text{hydrodynamics}} + F_{\text{moorings}} + F_{\text{aerodynamics}} \tag{4.2}$$

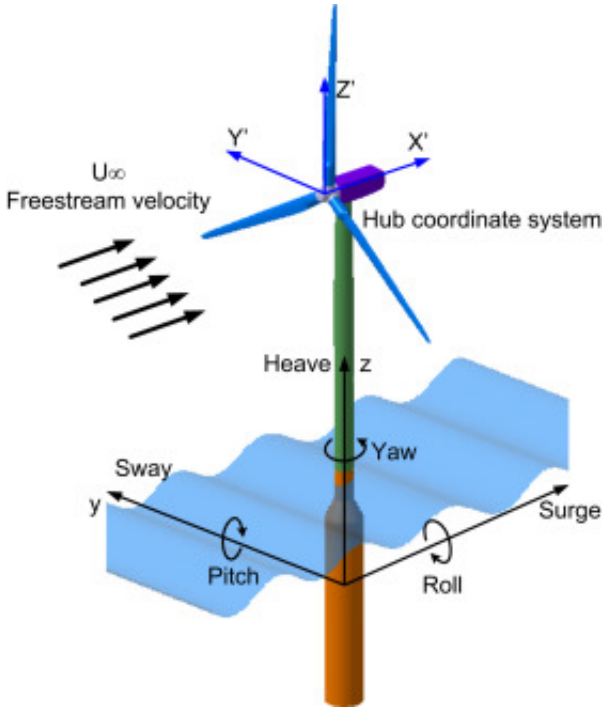

Figure 4.1: The degrees of freedom for a floating spar-type offshore wind turbine (Tran & Kim, 2015).

The external loads act on a FOWT include the aerodynamic loads, hydrostatic forces, hydrodynamic loads and mooring system forces. The hydrostatics and mooring loads consist the restoring forces for the system. On the current study, waves and currents are mainly the most dominant hydrodynamic loads. However there is a variety of loads such as tides, seismic activity or ice (Cradden et al., 2016).

The aerodynamic loads on a FOWT depend mainly on the wind conditions and the rotor characteristics. However, due to floating motion the relative wind velocity is the velocity seen by the moving rotor at hub height and is given by Equation 4.3:

$$\vec{V}_{\text{rel}} = \vec{V} - \vec{V}_{\text{hub}} \tag{4.3}$$

where $\vec{V}_{\text{rel}}$ is the relative wind velocity vector, $\vec{V}$ the incoming undisturbed wind velocity vector and $\vec{V}_{\text{hub}}$ represents the hub velocity vector due to motions of the structure.

As a consequence the wind force is given by Equation 4.4:

$$\vec{F}_{\text{aerodynamics}} = \frac{1}{2} \cdot \rho_{\text{air}} \cdot \pi \cdot R^2 \cdot C_t(\lambda, \beta) \cdot \vec{V}_{\text{rel}}^2 \tag{4.4}$$

where ρ_{air} is the air density, R is the rotor radius and C_t is the wind turbine's thrust coefficient which is influenced by he tip speed ratio λ and blade pitch angle β.

The other forces are acknowledged but not examined in detail, since the main scope of this project is the power generation investigation and not load analyses.

4.1.2. Power production in FOWTs

The power production of a FOWT deviates in two ways when compared to a fixed-bottom. The first consideration is the influence of the movements of the floating offshore wind turbine, which result in an additional average tilt angle in the platform. Consequently, the rotor is slightly angled relative to the incoming wind velocity V_{wind}. To address this effect in the power calculation, the inflow wind velocity is modified by reducing it by the cosine of the pitch angle θ of the structure, as indicated by Equation 4.5

(Matha et al., 2016). This adjustment compensates for the rotor's inclination caused by the platform's tilt.

$$V_{\text{tilt}} = V_{\text{wind}} \cdot \cos(\theta) \tag{4.5}$$

In addition, as has been described by Equation 4.4, the aerodynamic force $\vec{F}_{\text{aerodynamics}}$ considers the relative wind speed based on the translational and rotational motion of rotor. The above lead to the following equations for the power production (Lerch et al., 2019):

$$P_{\text{FOWT}} = \frac{1}{2} \cdot \rho_{\text{air}} \cdot \pi \cdot R^2 \cdot C_P(\lambda, \beta) \cdot V_{\text{tilt}}^3 \tag{4.6}$$

where C_P represents the power coefficient of the wind turbine, influenced by both the tip speed ratio λ and the blade pitch angle β.

The tilted wind speed is calculated as:

$$V_{\text{tilt}} = V_{\text{rel}} \cdot \cos(\theta) \tag{4.7}$$

4.2. OpenFAST theory

For the modelling of wind turbines there have been developed different software. The software that was used in the current thesis project for modelling the TetraSpar demonstrator is the OpenFAST (NREL, 2024).

OpenFAST (previously named FAST) is a multi-physics, multi-fidelity tool for simulating the coupled dynamic response of wind turbines. It acts as a framework that integrates various computational modules covering aerodynamics, hydrodynamics, control and electrical systems dynamics, and structural dynamics. This integration allows for the simulation of complex interactions between aerodynamics, hydrodynamics, control mechanisms and structural dynamics in real-time. OpenFAST supports the analysis of diverse wind turbine configurations, such as different rotor designs (two or three blades), regulation methods (pitch or stall), hub types (rigid or teetering), rotor orientations (upwind or downwind) and tower structures (lattice or tubular). Additionally, it can model wind turbines installed on land or offshore, including fixed-bottom or floating platforms.

OpenFAST consists of different modules as described before. These modules could be used as standalone modules or coupled with OpenFAST to model wind turbines and its support structures. As shown in Figure 4.2 the external conditions such as wind and waves are used in order to compute the applied loads. Next, the applied loads are coupled using the modules in order to give as output various parameters for the performance and response of the wind turbine and other parts of the structure such as the mooring lines.

For the current study, only the following modules were used:

AeroDyn module
This a time-domain wind turbine aerodynamics module that is coupled with OpenFAST to enable aero-elastic simulation of horizontal-axis turbines. AeroDyn calculates aerodynamic loads on blades and tower using actuator line principles, approximating three-dimensional flow with local two-dimensional flow at cross sections. Distributed pressure and shear stresses are represented by lift forces, drag forces and pitching moments lumped at nodes along the length of each structure. While the model's validity is limited to slender structures due to its actuator line approximations, corrections such as tip-loss, hub-loss or skewed-wake corrections are incorporated into input data to compensate for the neglect of three-dimensional behaviour.

AeroDyn assumes the turbine geometry consists of a one-, two- or three-bladed rotor at the top of a tower. In addition, environment conditions, airfoil information, blade and tower properties are also included in the input file. One important part of AeroDyn module is the method used for calculating the effect of wake on rotor aerodynamics. There are currently three methodologies available: Blade Element Momentum (BEM) theory, Dynamic Blade Element Momentum (DBEM) theory and the cOnvecting LAgrangian Filaments (OLAF). In the current study, the BEM theory was utilised.

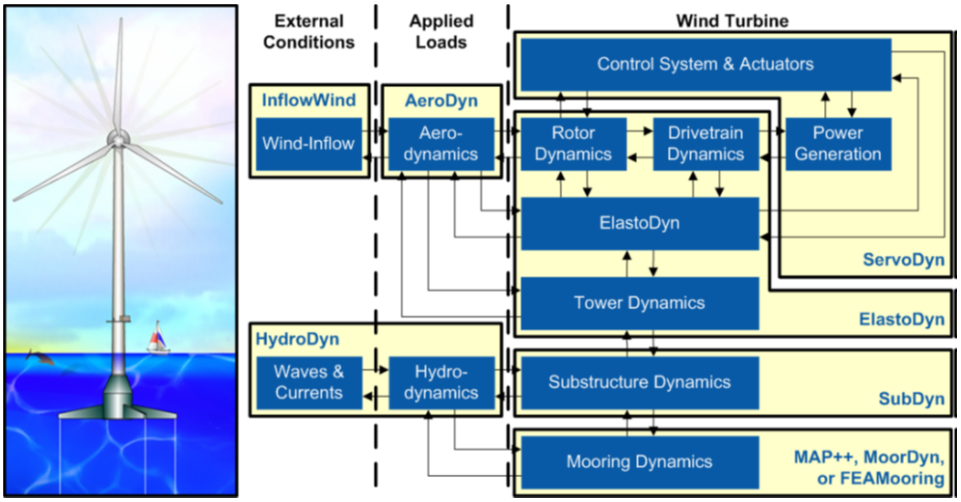

Figure 4.2: OpenFAST schematic (Jonkman et al., 2020).

Despite its simplicity, the BEM theory has some limitations due to its assumptions. In order to overcome these limitations, OpenFAST has incorporated some correction models (Moriarty & Hansen, 2005). Firstly, the tip loss model is used to account for the limitation that there is not influence of vortices shed from the blade tips into the wake on the induced velocity field, which create helical structures in the wake and play a significant role in induced velocity distribution at the rotor. Based on the same logic, there is also the hub loss model to compensate for vortices shed at hub location. Another drawback of blade element momentum theory is its initial design for axisymmetric flow. However, wind turbines frequently operate at yaw angles concerning the incoming wind, resulting in a skewed wake behind the rotor. To address this issue, the BEM model is adjusted using the Pitt and Peters correction method.

ElastoDyn module
ElastoDyn serves as a tool for predicting the forces and moments exerted on both blades and towers of wind turbines. By inputting parameters such as mass, stiffness and inertia of the blades and tower, along with essential dimensions and wind turbine characteristics, ElastoDyn can accurately estimate forces, moments and deflections. Moreover, for floating offshore wind turbines, ElastoDyn goes beyond static analysis and is capable of predicting both translational and rotational motions. This comprehensive capability makes it an invaluable tool for assessing the performance and behaviour of wind turbines in offshore environments.

HydroDyn module
The HydroDyn module is utilised to simulate ocean conditions and the hydrodynamic loads on the floating platform. Concerning ocean conditions, it's possible to simulate waves and currents based on parameters such as significant wave height and period. Additionally, external wave data can be inserted, which were employed in the current report, where on-site measured wave elevation time series and direction served as input for the HydroDyn module.

Apart from simulating sea states, the module also models the floating platform by inserting the properties of platform elements. The hydrodynamic loads are estimated using three different theories: potential flow theory, strip theory or a hybrid theory which combines both. For the current study, strip theory was employed, wherein loads are calculated using Morison's equation in its relative form. This equation encompasses distributed fluid inertia, added mass and viscous drag components. Alongside these, there are additional distributed load elements, such as axial loads resulting from tapered members and static buoyancy loads (NREL, 2024).

InflowWind module
InflowWind is responsible for simulating the desired wind conditions at different points. Various wind types can be simulated, such as steady wind, uniform wind, binary TurbSim full-field (FF), binary Bladed-style FF and HAWC formatted binary FF wind files (Platt et al., 2016). Based on the type, specific input parameters should be defined, such the horizontal wind speed and hub height.

MoorDyn module
MoorDyn is the module designed for simulating the mooring lines of floating structures. It employs a lumped-mass technique to divide the cable dynamics along the length of the mooring line into discrete segments. This module offers flexibility in modelling various aspects such as interconnections between lines, the inclusion of clump weights and floats, and the consideration of different line properties. It takes into account internal axial stiffness and damping forces, as well as the effects of weight, buoyancy, hydrodynamic forces based on Morison's equation and vertical spring-damper forces arising from contact with the seabed (Hall, 2015).

ServoDyn module
The ServoDyn module is responsible for wind turbine control. It offers options for simulating the controller, allowing users to manually implement diverse control strategies like pitch control, torque control, nacelle-yaw control and high-speed shaft brakes.

To summarise, OpenFAST consists of different modules, but for the current study, only the AeroDyn, ElastoDyn, HydroDyn, InflowWind, MoorDyn and ServoDyn modules were used. These modules were coupled together to accurately model the power generation and motion of the TetraSpar demonstrator under different conditions.

5

Model development

In this chapter, the development of the TetraSpar model in OpenFAST is described. Firstly, section 5.1 highlights the differences between the OpenFAST coordinate system and the coordinate system of the on-site location. In section 5.2, the differences in the propagation direction of weather conditions are presented. Following this, section 5.3 describes the modelling of the wind turbine and section 5.4 details the modelling of the floating platform. Next, section 5.5 explains the mooring system modelling, while in section 5.6 an overview of the TetraSpar model as created in OpenFAST is provided.

5.1. Coordinate system

In order to compare the motion of the OpenFAST model with the on-site data, the orientation and coordinate system of OpenFAST should be perfectly aligned with the on-site location. As far as the OpenFAST is concerned, the platform motions are described within a reference inertial frame coordinate system. This coordinate system is established with its origin situated at the intersection of the undisplaced tower center line and the mean sea level. In this context:

- The positive x-axis extends in the nominal direction, aligned with zero degrees wind and wave.
- The positive y-axis stretches to the left when observed from above.
- The positive z-axis is oriented vertically upward, contrary to the direction of gravity.

Relative to this coordinate system, the platform's degrees of freedom are defined. The translational motions of surge, sway and heave are defined along the positive x, y and z axes, respectively, while the rotational motions of roll, pitch and yaw are described along the same axes, with positive values determined according to the right-hand rule convention. The exact origin of these DOFs depends on the parameter known as `PtfmRefzt`, which is defined as the vertical distance from mean water level. When `PtfmRefzt` is set to zero, the origin of the platform's DOFs aligns with that of the inertial frame coordinate system.

Regarding the coordinate system of the on-site location, it deviates from that of OpenFAST in terms of orientation:

- Surge: Positive along the negative x-axis of OpenFAST.
- Sway: Positive to the left when observed from above, similar to OpenFAST.
- Heave: Positive in the downward direction (similar to gravity), contrasting with OpenFAST.

Rotational motions, including roll, pitch and yaw are measured about axes fixed to the floater, following the right-hand rule.

Based on the above, it is cleat that the coordinate system of OpenFAST and on-site location deviates. For this reason, in order to align the coordinate system of the motions from OpenFAST with the on-site location, the following adjustments need to be done:

- Surge:

$$\text{Surge}_{\text{OpenFAST}} = -\text{Surge}_{\text{on-site}}$$

- Sway:

$$\text{Sway}_{\text{OpenFAST}} = \text{Sway}_{\text{on-site}}$$

- Heave:

$$\text{Heave}_{\text{OpenFAST}} = -\text{Heave}_{\text{on-site}}$$

The change in the orientation of the surge and heave axes also affects the rotational motions, roll and yaw. Consequently, when comparing simulated roll values with on-site measured data, the simulated values should be negated to align with the correct direction in the OpenFAST coordinate system. The same consideration applies to yaw motion. These adjustments are summarised below:

- Roll:

$$\text{Roll}_{\text{OpenFAST}} = -\text{Roll}_{\text{on-site}}$$

- Pitch:

$$\text{Pitch}_{\text{OpenFAST}} = \text{Pitch}_{\text{on-site}}$$

- Yaw:

$$\text{Yaw}_{\text{OpenFAST}} = -\text{Yaw}_{\text{on-site}}$$

Applying these adjustments ensures that the OpenFAST results are properly aligned with the on-site measured data for comparison.

5.2. Weather conditions

In order to compare the motion and power output of the wind turbine under different cases, similar weather conditions as the on-site measured data should be used in OpenFAST. In OpenFAST, the wind propagation is defined as in Figure 5.1a, while the propagation direction of waves and currents is given by Figure 5.2a. However, the direction of wind, waves and currents on the site location is different when compared to OpenFAST. Wind coming from direction 0° is North, while 90° is East (Figure 5.1b). The similar condition states for waves, as can be seen in Figure 5.2b, and currents.

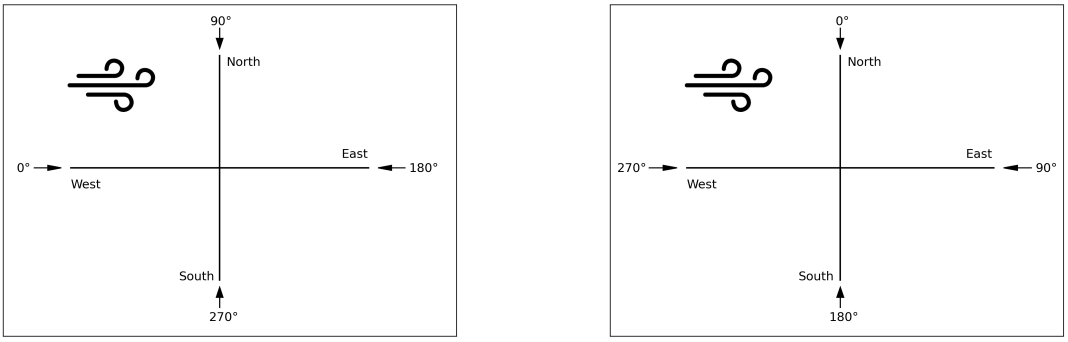

(a) OpenFAST **(b)** On-site

Figure 5.1: Comparison of wind propagation direction in OpenFAST (a) and on-site location (b).

For this reason, the measured wind and waves are transformed based on the following conventions:

$$\theta_{\text{wind,OpenFAST}} = \begin{cases} \theta_{\text{wind,on-site}} + 90, & \text{if } \theta_{\text{wind,on-site}} < 270 \\ \theta_{\text{wind,on-site}} - 270, & \text{if } 270 \leq \theta_{\text{wind, on-site}} \leq 360 \end{cases}$$

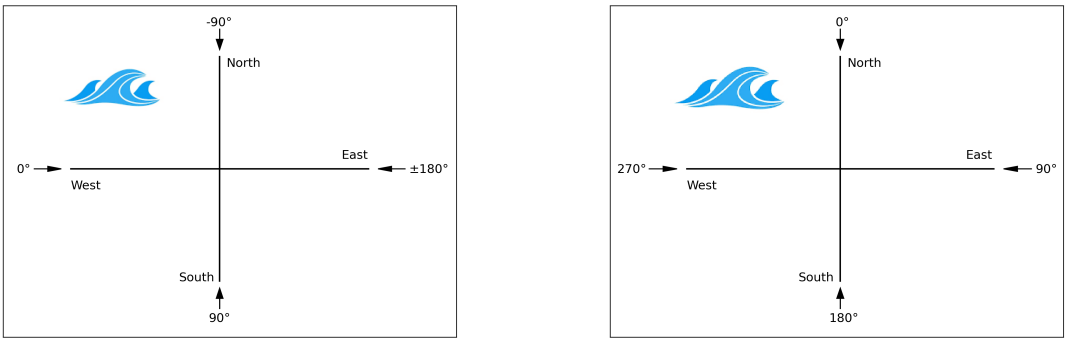

(a) OpenFAST **(b)** On-site

Figure 5.2: Comparison of wave propagation direction in OpenFAST (a) and on-site location (b).

$$\theta_{\text{wave,OpenFAST}} = \begin{cases} -90 - \theta_{\text{wave, on-site}}, & \text{if } \theta_{\text{wave, on-site}} < 90 \\ 270 - \theta_{\text{wave, on-site}}, & \text{if } 90 \leq \theta_{\text{wave, on-site}} \leq 360 \end{cases}$$

As has been described in section 2.4, the LiDAR is utilised to estimate the average wind speed at hub height over 10-minute intervals. The data provided by RWE include not only the mean wind speed but also the mean wind direction and the standard deviation for each 10-minute period. Based on the mean wind speed and the standard deviation, the turbulence intensity (TI) was estimated. However, for simulation purposes in OpenFAST, turbulent time series wind speeds are required, rather than the average 10-minute wind speed. Therefore, TurbSim was employed to generate turbulent wind fields based on the 10-minute average wind speed at hub height and turbulence intensity.

TurbSim is a stochastic, full-field, turbulent wind simulator. It uses a statistical model to simulate time series of three-component wind speed vectors at points in a two-dimensional vertical rectangular grid that is fixed in space. The output from TurbSim is then fed into AeroDyn which employs Taylor's frozen turbulence hypothesis to obtain local wind speeds by interpolating the TurbSim generated fields in both time and space.

5.3. Wind turbine modelling

As has been described in subsection 2.3.4, the wind turbine used for power generation is a 3.6 MW wind turbine with 130 m rotor radius. However, due to confidentiality, much of the data regarding the wind turbine are not publicly available, except for the information presented in Table 2.2. For the unknown parameters, estimations were based on internal data and the NREL 5 MW reference wind turbine (Jonkman et al., 2009), using scaling laws and other techniques that are presented below.

5.3.1. Tower

Tower data is needed in OpenFAST for both the AeroDyn and ElastoDyn modules. In the AeroDyn module, eleven tower nodes were used for the entire length of 71.6 m. At each node, the tower diameter was estimated, starting from 4.3 m at 16 m above mean water level and ending at 3.6 m at the top. The estimation of diameter at each node was based on internal data. Additionally, ElastoDyn module was used to model the structural properties of the tower. For eleven different section points starting from 16 m above sea level and increasing by 10% for every point, the mass density, flapwise and edgewise stiffness were inserted in OpenFAST based on proprietary sources. The structural damping considered in ElastoDyn is 0.5% critical damping for the first tower bending mode and 1% critical damping for the second tower bending mode (Thomsen et al., 2021).

To estimate the tower's first and second fore-aft and side-to-side mode shapes, the open-source software BModes was used (Bir, 2005). BModes is capable of estimating the frequencies of tower

side-to-side and fore-aft modes. The main data used for BModes simulation are the mass density, inertia and stiffness at different nodes. The tower's first and second frequencies were based on the magnitude of displacements. After estimating the dominant frequencies, OpenFAST required as inputs the mode shape coefficients for these frequencies in the form of a six-degree polynomial formula as can be seen in Equation 5.1, where x is the normalised height location along the tower, y is the displacement and α represents the polynomial coefficients. For the calculation of the polynomial coefficient given deflection data along the tower, an Excel file provided by the BModes software was employed.

$$y = \alpha_6 \cdot x^6 + \alpha_5 \cdot x^5 + \alpha_4 \cdot x^4 + \alpha_3 \cdot x^3 + \alpha_2 \cdot x^2 \tag{5.1}$$

5.3.2. Blades

The modelling of the blades in OpenFAST was performed using 51 blade nodes per blade. The distributed blade properties at each node, such as mass density, stiffness and twist, were based on internal data. For estimating the flapwise and edgewise mode shapes, the same procedure used for the tower was followed, utilising the software BModes. Each node represents a specific point along the blade, allowing for precise simulation of the blade's behaviour. Using BModes ensures accurate representations of both flapwise and edgewise deformations, enhancing the overall accuracy of the OpenFAST simulation.

5.3.3. Airfoil selection

The selection of appropriate airfoils for the wind turbine is crucial. However, the airfoils used in the 65 m blades are confidential. Therefore, the same airfoils as those used in the NREL 5 MW wind turbine were adopted. The chosen airfoils were accompanied by an updated blade distribution, considering the difference in blade length between the NREL turbine and the turbine of the TetraSpar demonstrator. The updated airfoil distribution is visible in Figure 5.3, while the airfoil shapes are presented in Figure 5.4.

Blade span (m)	Airfoil
4.2	Cylinder
7.0	Cylinder
10.5	DU 40
18.9	DU 35
23.1	DU 30
31.5	DU 25
39.9	DU 21
65.0	NACA 64

Figure 5.3: Airfoil distribution along the blade span.

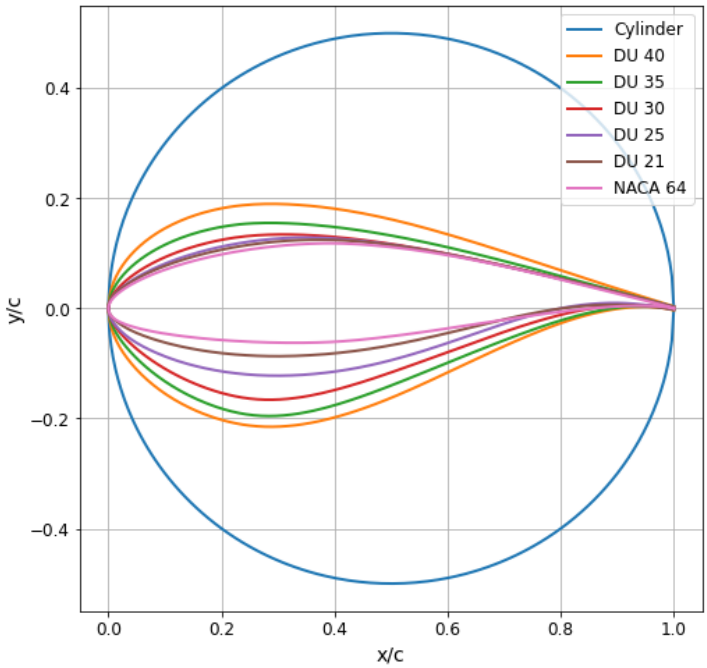

Figure 5.4: Shape of airfoils used along the blade span.

5.3.4. Controller modelling

Controller is one of the most important parameters of this project, since the main scope is the estimation of power output. Apart from regulating the power output of the wind turbine, controller is responsible for minimising the fatigue on the wind turbine. In below rated region the torque controller is used so as the turbine to operates at the maximum tip speed ratio. On the other hand, in above rated wind speed the

pitch controller maintains the power output of the wind turbine at the rated value by pitching the blades. Apart from the above, the controllers that are used in FOWTs are responsible for improving the stability of the floating platform by using a floating feedback. This floating feedback was also incorporated into this project. However, due to confidentiality there are not information provided by the wind turbine manufacturer for the characteristics of the controller, as it is proprietary information. For this reason, the ROSCO open source controller was applied (NREL, 2021).

In order to tune the controller, the ROSCO generic theory was adopted (Abbas et al., 2021). The ROSCO toolbox offers a procedure in order to implement the desired controller. The main tuning of the controller is performed by a python code that calls an input file containing all the turbine and controller parameters and creates the DISCON input file that is used by the ServoDyn module in OpenFAST. The aerodynamic and performance coefficient tables (C_p, C_t and C_q) were left the same as the NREL 5 MW wind turbine due to the unavailability of further information for the 3.6 MW wind turbine. As far as the turbine parameters are concerned, these include, for instance, the rated power, the operating region and the rated wind speed. On the other hand, the controller parameters are responsible for the control modes that are used. More specifically, a TSR tracking PI control was implemented in the generator torque control mode in above rated conditions, and for the blade pitch control, an active PI blade pitch control was utilised. Additionally, a wind speed estimator mode was used based on a continuous-discrete extended Kalman filter and a floating feedback mode to account for the platform motion. Furthermore, a set point smoother regime was employed in order to avoid the conflict between the generator torque and blade pitch controllers in near rated operation. In practice, the set point smoother adjusts the generator speed reference signal of the saturated controller while the unsaturated controller is active. This prevents conflicting behaviours between the controllers by ensuring that one controller remains active while the other is inactive (Abbas et al., 2021). Lastly, yaw control was not applied. This consideration was made because in the InflowWind module, the average 10-minute wind direction was used. As a result, it did not make sense to track the wind direction. The constant wind turbine yaw direction that was used was the average 10-minute wind direction from the on-site measured data. By this, the wind yaw misalignment was accounted for in the model.

According to Larsen and Hanson (2007), the tuned bandwidth of a rotor speed-regulating collective blade pitch controller should not exceed the platform's first fore-aft eigenfrequency. This method was applied when tuning the ROSCO controller, by ensuring that the pitch controller natural frequency was less than frequency estimated in section 6.1. For the estimation of the pitch controller desired damping ratio, the appropriate value was determined by performing simple simulations with step wind. The effect of the damping ratio on the generated power is presented in Figure 5.5. For the torque controller's desired natural frequency and damping ratio, the tuning procedure was performed using a trial-and-error method.

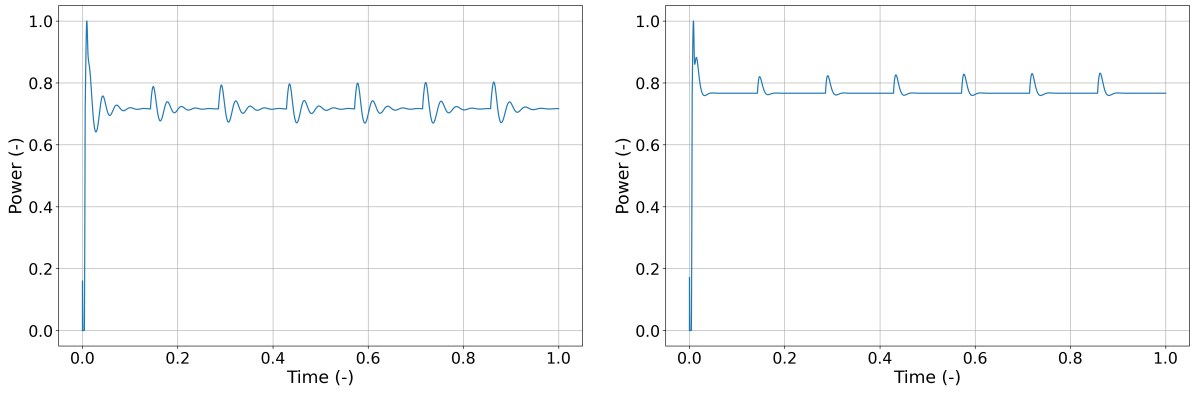

(a) Low damping ratio

(b) High damping ratio

Figure 5.5: Effect of pitch controller damping ratio for untuned controller with low damping ratio (a) and tuned controller with higher damping ratio (b) in the normalised generated power in the above rated region. Simulations were performed with a step wind input.

5.4. Platform modelling

In order to model the floating platform, the ElastoDyn and HydroDyn modules were utilised. In ElastoDyn, the platform mass, inertia and center of gravity were defined. The entire platform (floater, suspension lines, keel) was treated as a rigid body with six degrees of freedom. Additionally, in ElastoDyn, the platform reference point, `PtfmRefzt`, located 40 m below the MWL, was defined. This point serves as the reference for all platform translational and rotational motion, which were estimated and compared with on-site measured data.

Initially, the floating platform was intended to be modelled using potential flow theory, requiring the use of the WAMIT software (WAMIT, Inc. & Massachusetts Institute of Technology, 2023). Modelling the entire platform in WAMIT is necessary to acquire the hydrostatic restoring matrix, frequency-dependent hydrodynamic added mass matrix and damping matrix, and frequency- and direction-dependent wave excitation force vector per unit wave amplitude. Due to time constraints and license approval delays, strip theory was adopted instead, which is a suitable approach for slender structures like the TetraSpar demonstrator.

Initially, the member connection points were specified in the HydroDyn module and the coordinates for floater members, keel members and suspension lines were inserted in the module based on Table A.2, Table A.3 and Table A.4. It should be mentioned that these coordinates were rotated in order to meet the exact on-site location of TetraSpar demonstrator. The rotation angle is not disclosed due to confidentiality. Additionally, their diameter and thickness were identified based on internal data. The inertia coefficient was defined as $C_M = 1 + C_A$, where $C_A = 1$ is the added mass coefficient. The drag coefficient was defined as $C_D = 0.6$ (Thomsen et al., 2021). Axial hydrodynamic coefficients were also included for member joints and for the entire members, but due to confidentiality, they cannot be published. The model did not consider second-order floating platform forces. Furthermore, neither second-order wave kinematics nor marine growth on the submerged members of the platform were accounted for.

To summarise, the floating platform model in OpenFAST utilises ElastoDyn to establish mass, inertia and center of gravity, treating the platform as a rigid body with six degrees of freedom. Due to time constraints and WAMIT licensing issues, strip theory was applied in HydroDyn to model platform members, with connection points, coordinates, diameters and thicknesses specified from internal data. Second-order platform forces, wave kinematics and marine growth were not accounted for.

5.5. Mooring system modelling

The catenary mooring system was modelled in the MoorDyn module. Each mooring line consists of four different line types whose diameter, mass density and stiffness were entered as inputs in OpenFAST based on the values in Table A.6. In addition, normal and axial drag, and added mass coefficients were also needed as inputs in OpenFAST. These values are treated as internal data and cannot be published.

Regarding the type of connection points used, three different types of connection points were implemented. The fairlead node, which is connected to the platform, is of 'vessel' type and its motion is defined in other modules, while the endpoint of the mooring line, anchored to the seabed, is a 'fixed' type attachment that cannot be moved. For the other points where the different segments are connected, 'free' type points were used, which, as their name implies, move according to the forces acting on them, including the tensions of attached lines, as well as their own self-weight and buoyancy (Hall, 2015). As a result, each mooring line consists of one 'fixed' point, one 'vessel' point and five additional 'free' points.

To estimate the coordinates of the connection points between different segments, which were needed in the MoorDyn module, the following approach was adopted. Starting with the coordinates of the fairlead and anchor nodes, along with the segment lengths of each mooring line listed in Table A.5, simple trigonometric equations were applied to determine the coordinates of the connection points.

5.6. Overview of the TetraSpar demonstrator model in OpenFAST

In previous sections, the methodology used for modelling the different components of the TetraSpar demonstrator was described. Based on this methodology, the schematic of the TetraSpar demonstrator model as created in OpenFAST is presented in Figure 5.6. As observed from the figure, there is a strong resemblance between the model and the actual TetraSpar on-site demonstrator, with the schematic accurately reflecting the key features and configuration of the demonstrator.

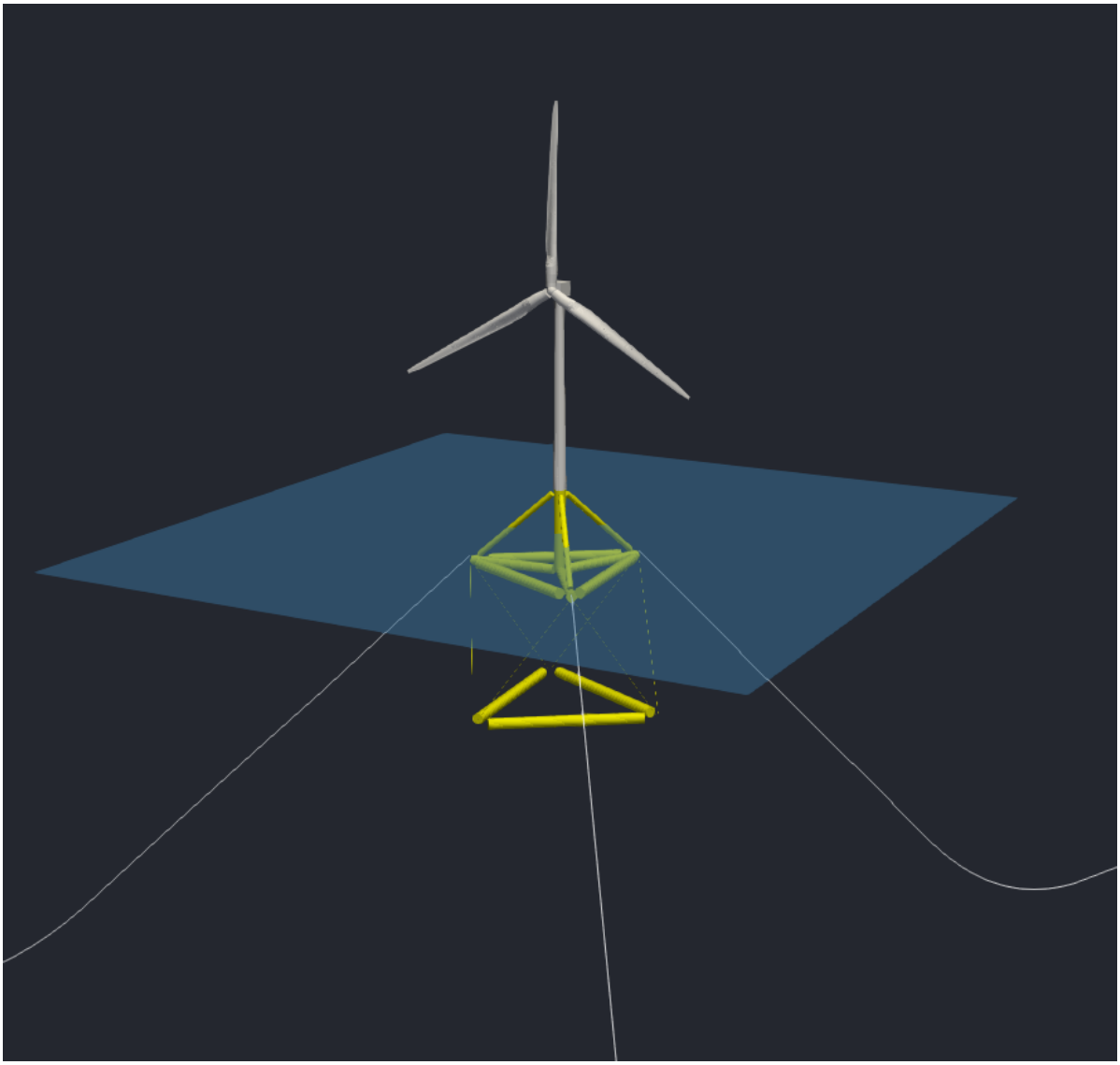

Figure 5.6: Schematic of TetraSpar demonstrator model in OpenFAST.

6

OpenFAST simulation results

In this chapter, various results are presented from the OpenFAST model and compared with the on-site measured data. The main area of interest is the motion of the floating platform and its impact on the generated power. Firstly, in section 6.1 free decay tests are performed to identify the natural frequencies of the system for the different platform motions. Secondly, in section 6.2 the platform motion and wind turbine power output are examined under three different hourly simulations. Next, in section 6.3 the power curve and the AEP are estimated for different controller tuning cases and compared to the on-site TetraSpar demonstrator and a fixed-bottom wind turbine. Following this, the platform motions are examined in section 6.4. Lastly, the limitations of OpenFAST model are analysed in section 6.5.

6.1. Free decay tests

Free decay tests are very important for the identification of the natural frequencies of floating offshore structures. If the response and natural frequencies of the OpenFAST TetraSpar model do not match those of the on-site location TetraSpar demonstrator, accurate results for power output cannot be estimated. For this reason, it is crucial to perform free decay tests.

The free decay simulations in OpenFAST were performed by applying the following modifications to the used modules:

- AeroDyn & InflowWind modules: Zero incoming wind speed and direction.
- HydroDyn module: No waves and currents.
- ServoDyn module: No blade pitch.

Furthermore, it was necessary to specify the initial displacement or rotation for each DOF, while all other initial conditions in the input were set to zero. In total, six free decay tests were simulated for each TetraSpar motion. In Figure 6.1a, Figure 6.2a, Figure 6.3a the free decay time series for surge, heave and pitch motions are presented. It should be noted that the time series data shown in these figures has been normalised on both axes. This normalisation is applied to facilitate comparison and to adhere to confidentiality requirements. In addition to the time domain analysis, the results in the frequency domain are also provided for the identification of natural frequencies. The Fast Fourier Transform (FFT) was performed on the motion data to analyse the frequency content and to identify the dominant frequencies corresponding to the system's natural frequencies. However, due to confidentiality reasons, the frequency domain plots do not disclose specific numerical values on the frequency and amplitude axis. This precaution is taken to prevent the direct disclosure of the natural frequencies, which could potentially reveal sensitive information about the system's dynamic characteristics. Free decay tests for the other motions are presented in section B.1.

As can be observed from Figure 6.1a, after the initial displacement the platform exhibits oscillations with diminishing amplitude. The final damping position occurs at the static equilibrium position, which is not at zero. This offset is due to the configuration of the mooring system, as the surge and sway

displacements are significantly affected by the mooring lines, which are unevenly distributed (Borg et al., 2020).

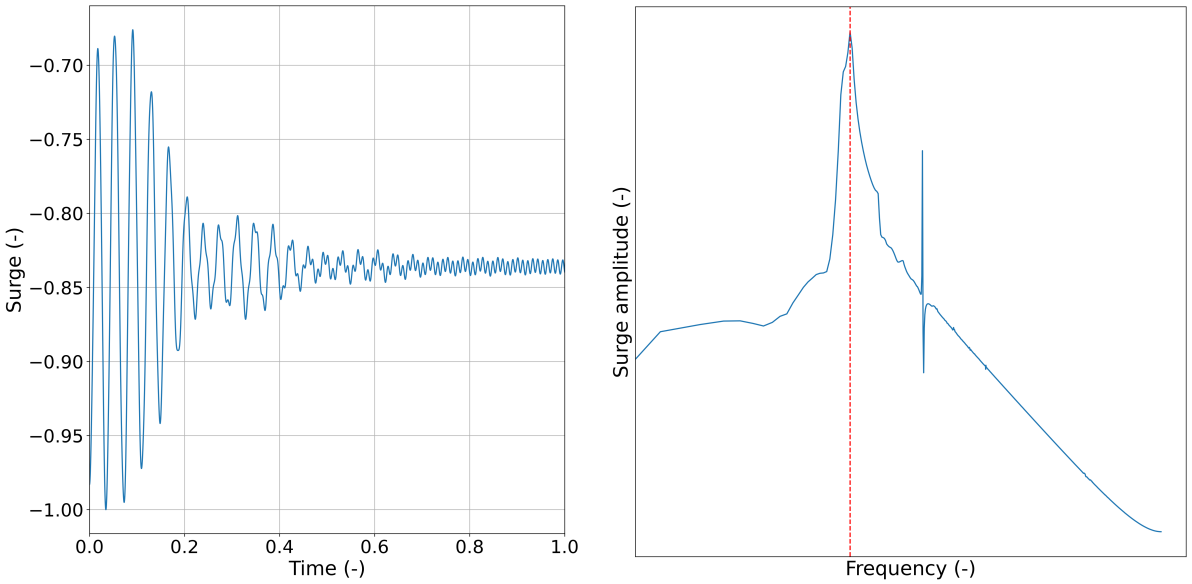

(a) Platform surge free decay time series

(b) Platform surge free decay in frequency domain

Figure 6.1: Normalised platform surge free decay time series (a) and frequency domain representation (b), where the red dashed line indicates the natural frequency of surge motion.

Compared to surge, heave motion (Figure 6.2a) exhibits a quicker damping, indicating a shorter natural period. The final damping at the zero point indicates that the platform achieves equilibrium at the mean sea level, validating that the entire weight of the structure equals the buoyant force.

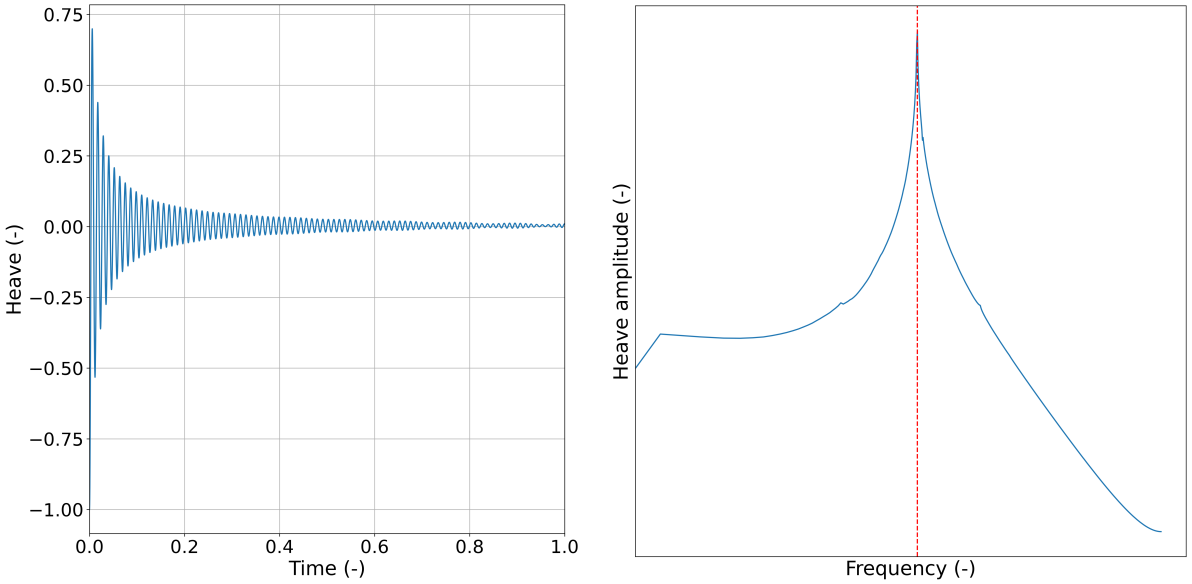

(a) Platform heave free decay time series

(b) Platform heave free decay in frequency domain

Figure 6.2: Normalised platform heave free decay time series (a) and frequency domain representation (b), where the red dashed line indicates the natural frequency of heave motion.

The pitch motion also dampens after the initial displacement but continues to oscillate with higher amplitude compared to surge and heave, as shown in Figure 6.3a. This is primarily attributed to the

wind turbine itself. More specifically, the rotor-nacelle assembly (RNA) is not perfectly aligned with the tower's axis, resulting in a restoring moment that induces continuous pitching of the platform.

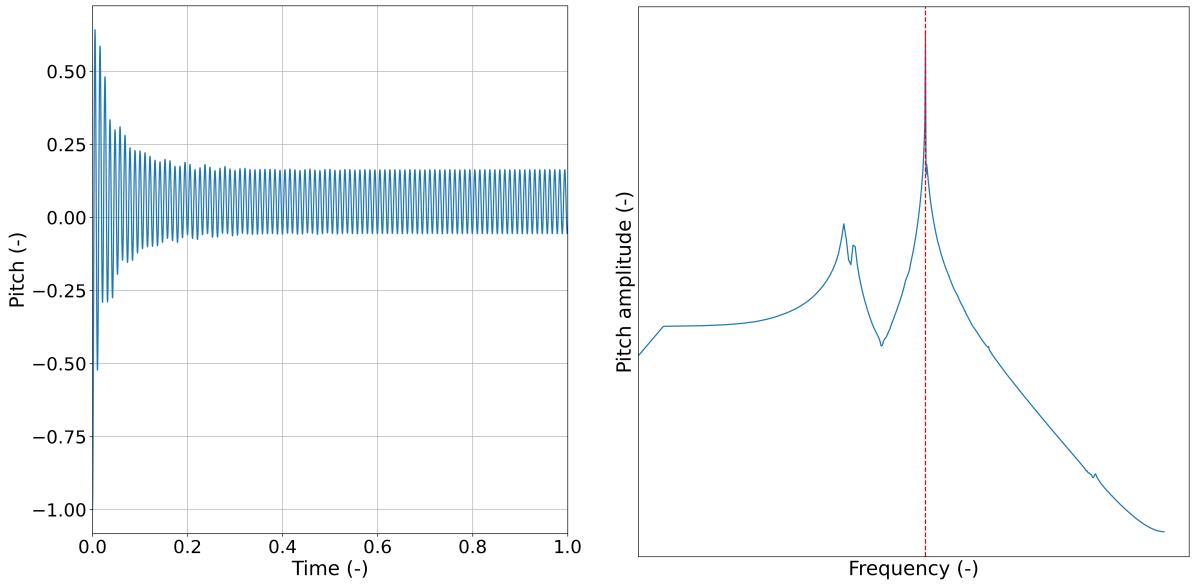

(a) Platform pitch free decay time series

(b) Platform pitch free decay in frequency domain

Figure 6.3: Normalised platform pitch free decay time series (a) and frequency domain representation (b), where the red dashed line indicates the natural frequency of pitch motion.

In FOWTs, surge and pitch motions are coupled. This is verified by Figure 6.1b and Figure 6.3b, where there is a secondary peak in the frequency domain. For instance, the secondary peak in the pitch frequency domain corresponds to the surge eigenfrequency. This coupling does not occur in the heave motion (Figure 6.2b), which is uncoupled. This coupling is also visible in the time domain, where the damping is more variable and less smooth in the coupled surge and pitch graphs compared to the heave motion.

In Table 6.1 the differences between the natural periods for the on-site TetraSpar demonstrator and those estimated by the free decay tests for the OpenFAST model are presented. Due to confidentiality, the absolute values cannot be revealed. Instead, the percentage differences between the OpenFAST estimates and on-site demonstrator are provided. It can be observed that the OpenFAST model estimates the sway and heave motions' natural periods very well, with differences of only -2.2% and 4.2%, respectively. The next motion with the smallest error is yaw, with a difference of 6.5%. A higher difference of approximately -12.5% is observed for roll. Lastly, surge and pitch motions have the highest differences, with OpenFAST underestimating the natural frequency by approximately 14.5%.

Table 6.1: Comparison of the percentage differences in natural periods between the on-site TetraSpar demonstrator and the OpenFAST model. Negative values indicate underestimation by the OpenFAST model.

Motion	Difference (%)
Surge	-14.5
Sway	-2.2
Heave	4.2
Roll	-12.5
Pitch	-14.3
Yaw	6.5

To summarise, free decay tests were conducted to estimate the natural frequencies of the OpenFAST model and compare them with those of the on-site TetraSpar demonstrator. The results indicate that all platform motions show damping after the initial oscillations in calm weather conditions. The

largest differences were observed in surge and pitch motions, while the other motions displayed smaller discrepancies.

6.2. Evaluation of one-hour simulations and on-site measurements

In this section, the wind turbine was tested under three different conditions: near cut-in, below rated and above rated wind speeds. Wind speeds beyond cut-out were not investigated since the main focus of the project is the power output assessment. Each test case was simulated for a duration of one hour. As previously mentioned, on-site measured data, recorded at a frequency of 25 Hz and were averaged over 10-minute periods for the entire year of 2023, which served as the reference year for the simulations. Consequently, each test condition required six averaged ten-minute periods.

Firstly, based on the wind speed and the turbulence intensity (TI) of each 10-minute period, TurbSim files were generated. Next, the other parameters needed for the OpenFAST simulation were extracted from the averaged data. For instance wind direction, wave direction and nacelle yaw angle. It should be noted that for simulating the waves, the measured surface elevation time series was used in OpenFAST, which supports the use of an externally generated wave elevation time series without needing significant wave height and wave period data. For the simulation of current, average current speed and direction at 3 m below mean surface level were adopted. Additionally, based on the measured air humidity, pressure and temperature, the air density was estimated and input into OpenFAST, while the six DOFs were fully enabled in OpenFAST in order to simulate the on-site condition.

The simulation of these one-hour test cases provides insights into the power output and motion of the floating platform. Due to time constraints and the lengthy duration required for one simulation, it was not feasible to run a simulation for every 10-minute period throughout an entire year. Moreover, there were periods when the measurement units were not working, resulting in missing or erroneous data. For these reasons, in section 6.3, averaged data were used for the estimation of AEP and response of the TetraSpar demonstrator. However, testing the three representative time periods for different operating conditions offers a real-time observation of the model behaviour.

6.2.1. Cut-in region

For the first simulation, the near cut-in region was examined. Due to confidentiality the exact cut-in wind speed is not available by the manufacturer of wind turbine. For this reason, the wind speed used for this is about 4.5 m/s, where from on-site measured data the wind turbine produces some power. For the simulation in cut-in region the used data are presented in Table 6.2.

Time	**Wind speed** (m/s)	**TI** (%)	**Wind direction** (°)	**Wave direction** (°)	**Nacelle yaw** (°)	**Current speed** (m/s)	**Current direction** (°)	**Air density** (kg/m³)
17:00:00	4.70	5.70	321.40	302.30	319.90	0.22	327.10	1.21
17:10:00	4.50	6.60	321.70	303.80	319.90	0.20	324.10	1.21
17:20:00	4.40	5.90	324.50	298.80	322.40	0.21	332.70	1.21
17:30:00	4.60	7.00	326.70	298.10	324.10	0.24	337.70	1.21
17:40:00	4.40	6.10	329.30	304.50	326.70	0.22	343.50	1.21
17:50:00	4.50	7.20	328.50	302.30	327.90	0.21	335.20	1.21

Table 6.2: Input parameters for OpenFAST simulations in cut-in region.

The initial approach for comparing platform motion between OpenFAST simulation and on-site measurement is illustrated in Figure 6.4, where the mean values and ranges of motions are presented. Due to confidentiality, the y-axis of all motions was normalised based on the minimum and maximum values of each motion. The same normalisation method is also applied for the other two cases examined: the below rated and above rated regions.

To begin with, it can be concluded for all motions that the standard deviation arising from the OpenFAST simulation is lower compared to the on-site measured data. This can be attributed not only to the metocean conditions of the simulation but also to the properties of the modelled TetraSpar in OpenFAST.

However, despite the disparities between the OpenFAST model and the real demonstrator, it is clear that the mean values of OpenFAST simulations fall between the margins of the on-site measurements, except for sway and yaw, indicating a reasonable agreement between the OpenFAST simulations and the actual measurements, despite some differences in variability.

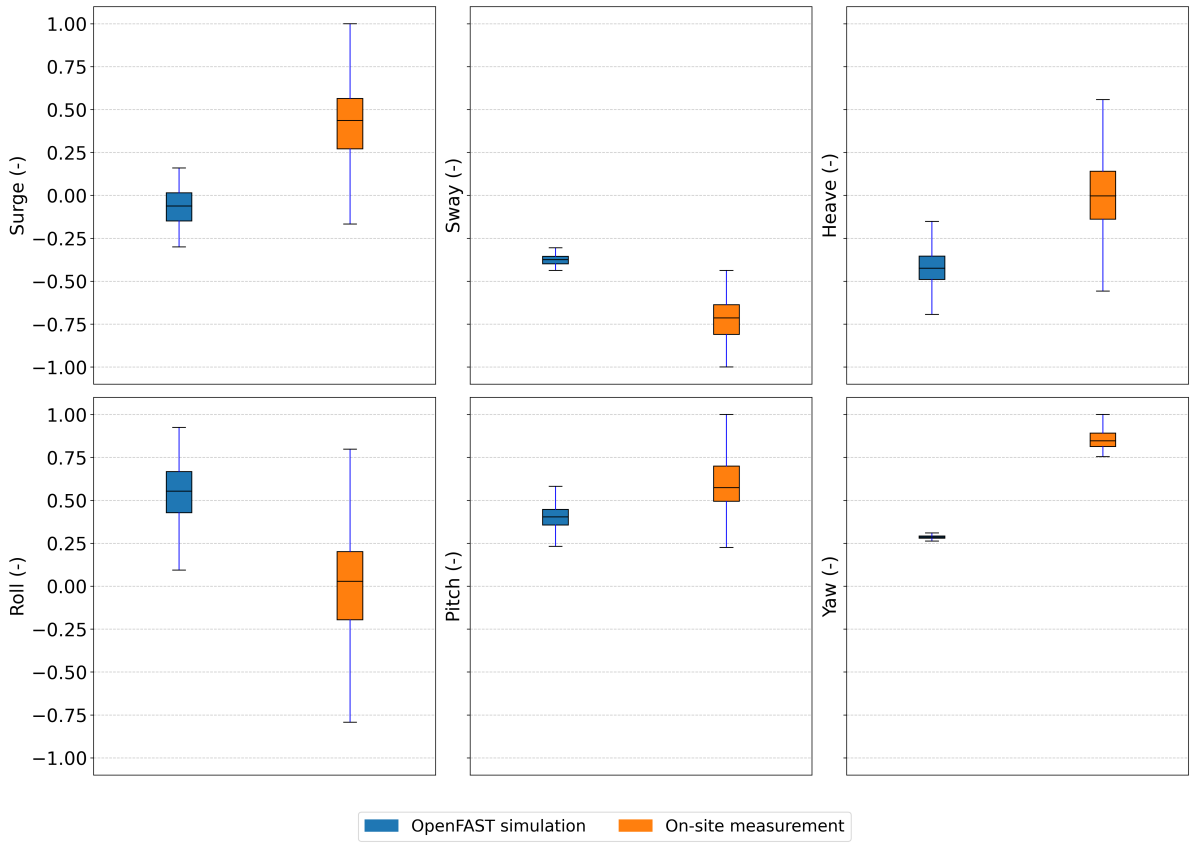

Figure 6.4: Normalised comparison between OpenFAST simulation and on-site measurement for all platform motions in cut-in region.

To provide more insight into the differences presented in Figure 6.4, the time series and spectral densities of motions are shown in the subsequent figures. It should be mentioned that in these figures, the y-axis in the time domain was normalised, while the graphs of power spectral densities are presented without values due to confidentiality. The reason for this is that the power spectral density is a normalisation function itself, making further normalisation redundant. Consequently, this approach allows for an illustrative view of power density without disclosing significant information related to the natural frequencies of the system and the response of the TetraSpar demonstrator.

To begin with, as can be seen from Figure 6.5a and Figure 6.6a, surge and sway motions in OpenFAST have lower oscillation amplitudes compared to on-site measurements. As far as the power spectral densities are concerned, it is visible from Figure 6.5b and Figure 6.6b that the energy content in the OpenFAST simulations is notably more consistent and exhibits less variability compared to the on-site measurement. At lower frequencies, the simulations tend to show less energy than observed in the measurements while at higher frequencies, the simulations appear to overestimate the energy content. Nevertheless, the general trend observed in the power spectral density of both surge and sway is consistent between the OpenFAST simulations and the on-site data, indicating that the simulation effectively captures the overall behaviour of these motions.

The discrepancies could be attributed to several factors related to the modelling and simulation processes used in OpenFAST. First, the hydrodynamic model used in OpenFAST does not include second-order wave effects, which can significantly impact the accuracy of the simulation. Additionally, in the simulations, only the current velocity and direction at three meters below mean sea level were

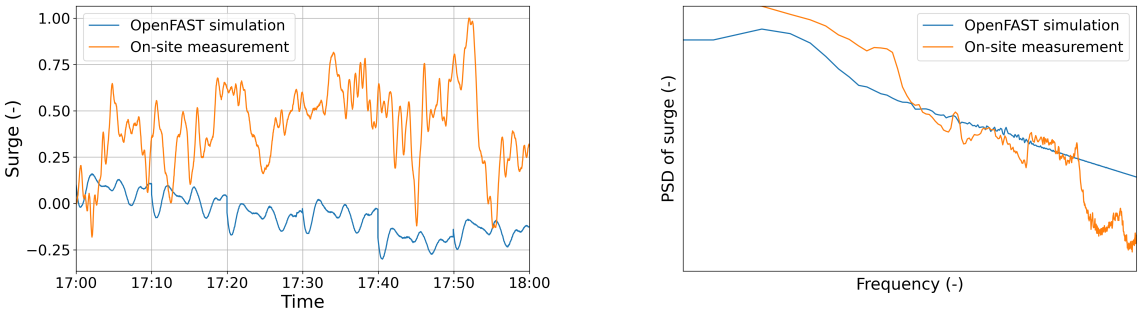

(a) Normalised surge time series

(b) Power spectral density of surge

Figure 6.5: Comparison of normalised platform surge time series (a) and power spectral density (b) between OpenFAST and on-site measurement in cut-in region.

considered. This simplification could lead to inaccuracies in representing the actual current profile experienced by the platform. Furthermore, the hydrodynamic coefficients were derived from internal data and using strip theory. However, accurately estimating the platform stiffness and damping matrix used in HydroDyn with the WAMIT utilisation proved impossible, as described in section 5.4, potentially leading to less accurate results. Moreover, the complexity of the mooring system also plays a crucial role in translational motions like surge and sway. Each mooring line consists of four different line types, and it is possible that the simulated model is stiffer than the actual system, resulting in more damping and a reduced response. Lastly, the wind time series used in the simulation are based on the average turbulence intensity (TI) and wind direction, which might not capture the full variability of the actual wind conditions experienced by the platform. Overall, these factors collectively contribute to the differences observed between the OpenFAST simulations and the on-site measurements, leading to lower oscillation amplitudes in the simulated results.

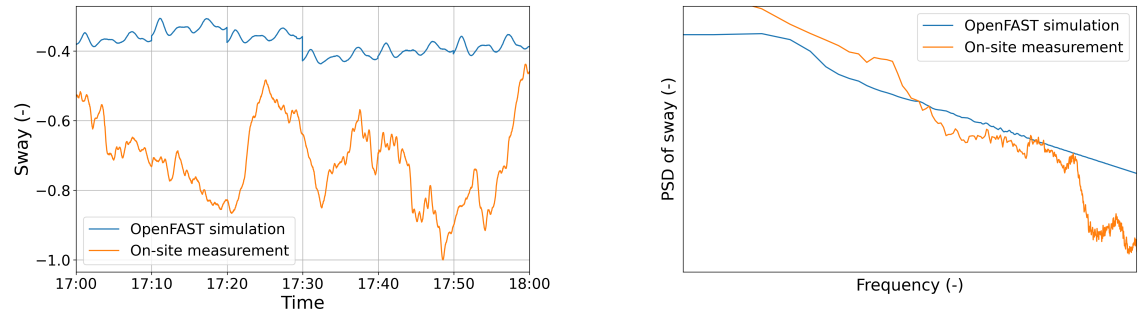

(a) Normalised sway time series

(b) Power spectral density of sway

Figure 6.6: Comparison of normalised platform sway time series (a) and power spectral density (b) between OpenFAST and on-site measurement in cut-in region.

Regarding rotational motions, specifically roll and pitch, the time series from OpenFAST simulations are closer to the measurements compared to the translational motions, as shown in Figure 6.7a and Figure 6.8a. For pitch, OpenFAST appears to underestimate the motion, while for roll, it tends to overestimate compared to the measurements. The absence of high peaks and excessive oscillations in both pitch and roll suggests that the platform is relatively stable.

In the frequency domain, the fluctuations and overall patterns for roll and pitch, as depicted in Figure 6.7b and Figure 6.8b, respectively, are more similar to those observed in the on-site measurements than the translational motions. This indicates a better agreement between the OpenFAST simulations and the actual data for these rotational motions.

After presenting the motion of the TetraSpar, the difference between produced power is given in Figure 6.9. It is evident that OpenFAST underestimates the mean power. This difference arises from

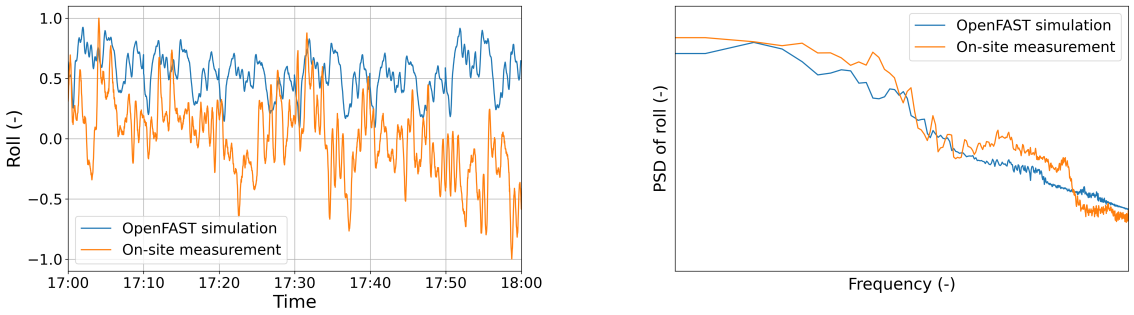

(a) Normalised roll time series

(b) Power spectral density of roll

Figure 6.7: Comparison of normalised platform roll time series (a) and roll spectral density (b) between OpenFAST and on-site measurement in cut-in region.

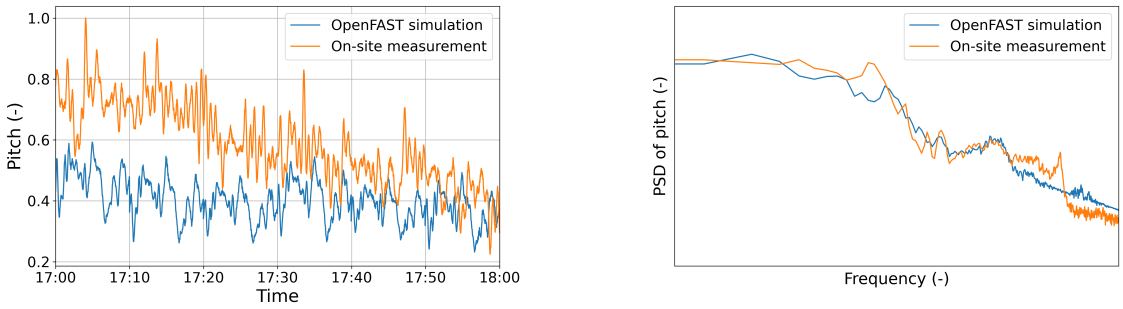

(a) Normalised pitch time series

(b) Power spectral density of pitch

Figure 6.8: Comparison of normalised platform pitch time series (a) and pitch spectral density (b) between OpenFAST and on-site measurement in cut-in region.

the lack of information about the controller, which led to an unknown start-up procedure. Given that this discrepancy in power output occurs only in the cut-in region and within a very narrow range of wind speeds with low probability and minimal impact on the AEP estimation, the primary focus of this project, it was decided not to explore different tuning techniques to improve the power output in this region and further investigation was not pursued.

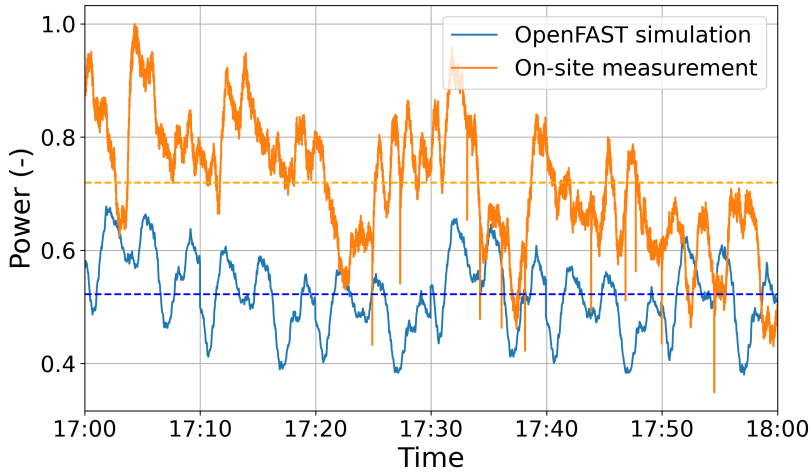

Figure 6.9: Comparison of generated power between OpenFAST and on-site measurement in cut-in region.

Overall, the rotational motions were estimated more accurately compared to the translational motions. The difference in mean power has a negligible effect on the AEP due to its occurrence in a low wind speed region with a low probability of occurrence. The discrepancies between OpenFAST and the measurements are primarily attributed to factors such as weather conditions (particularly wind and waves), hydrodynamic coefficients, mooring system and the lack of information about the controller and wind turbine. For completeness, results for heave and yaw are provided in subsection B.2.1.

6.2.2. Below rated region

For the second simulation, the region below the rated wind speed was examined. Due to confidentiality, the exact rated wind speed is not disclosed. Therefore, an hour with mean wind speed approximately 8.5 m/s was used. The exact input parameters for this simulation are presented in Table 6.3 and the statistical analysis of the mean values and margins of platform motions is presented in Figure 6.10.

Time	Wind speed (m/s)	TI (%)	Wind direction (°)	Wave direction (°)	Nacelle yaw (°)	Current speed (m/s)	Current direction (°)	Air density (kg/m³)
19:30:00	8.60	5.60	346.20	334.70	345.50	0.14	188.80	1.27
19:40:00	8.80	4.70	340.30	335.40	340.40	0.13	159.90	1.27
19:50:00	8.80	6.20	343.30	333.30	342.90	0.12	168.20	1.27
20:00:00	8.40	6.70	342.90	329.80	342.60	0.11	147.10	1.27
20:10:00	8.30	5.90	344.50	330.50	344.90	0.10	176.10	1.27
20:20:00	8.20	6.80	346.40	332.60	345.30	0.10	150.70	1.27

Table 6.3: Input parameters for OpenFAST simulations in below rated region.

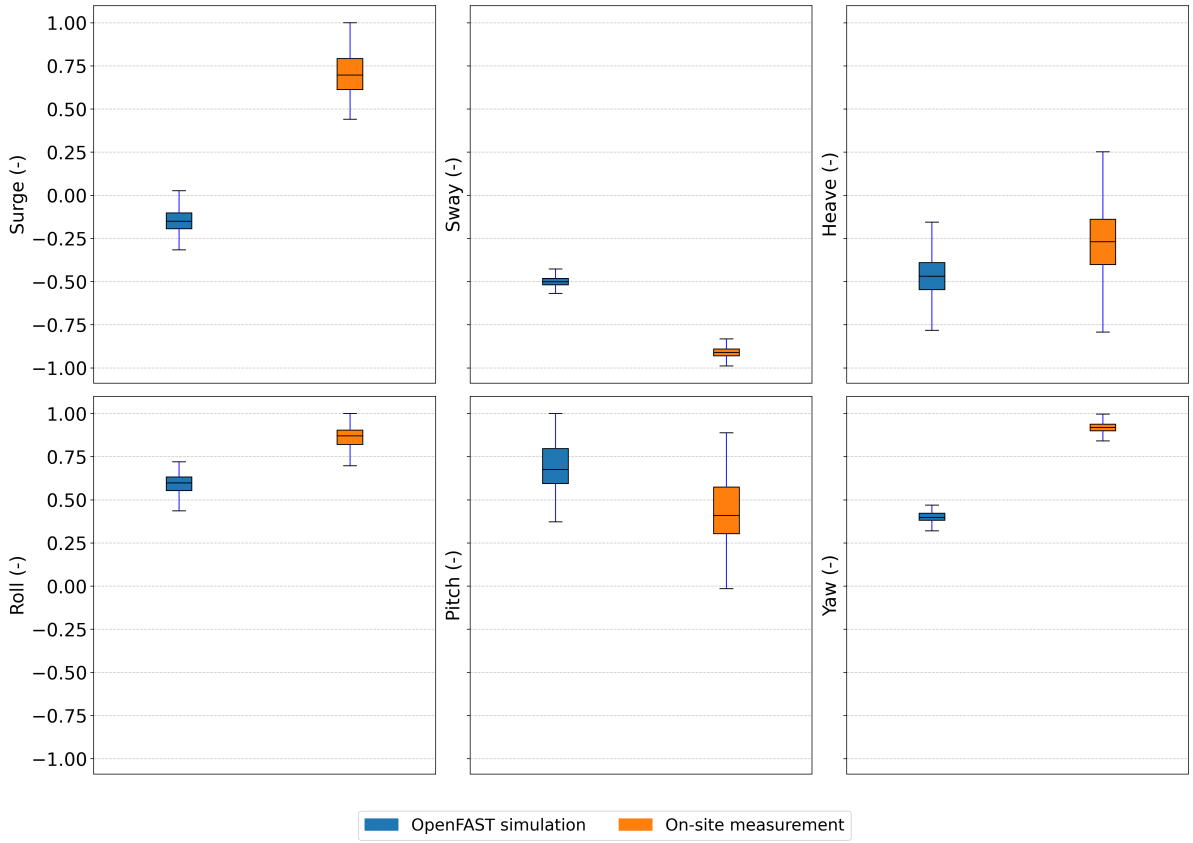

Figure 6.10: Normalised comparison between OpenFAST simulation and on-site measurement for all platform motions in below rated region.

It is evident that despite the harsher wind and wave conditions in this case compared to the cut-in region, which could potentially lead to greater deviations in the motion differences between OpenFAST and on-site measurement, the agreement appears to be satisfactory. Among all the motions, surge and sway show the greatest differences, with OpenFAST underestimating the motions in both cases. Similar findings were also observed in the cut-in region, which can be primarily attributed to discrepancies in the mooring system. For all other motions, the differences in mean values and standard deviations are minimal considering the uncertainties in the modelling of the wind turbine and the simulation of metocean conditions.

For the translational motions, surge and sway, the power spectral densities are presented in Figure 6.11a and Figure 6.11b, respectively. It can be observed that there is better agreement between OpenFAST model and on-site measured data compared to the cut-in region. More specifically, the peaks occur at the same frequencies and the PSD of OpenFAST overlaps with that of the measured data. The time series for surge and sway are presented in Figure B.7a and Figure B.7b, respectively, for completeness.

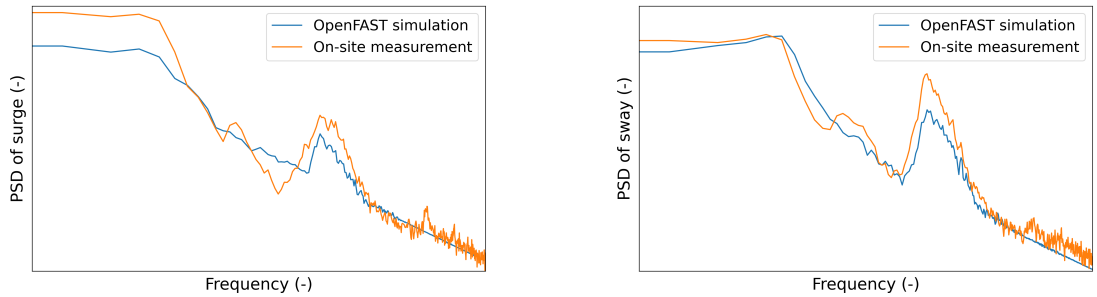

(a) Power spectral density of surge

(b) Power spectral density of sway

Figure 6.11: Comparison of normalised power spectral densities of platform surge (a) and sway (b) between OpenFAST and on-site measurement in below rated region.

As far as the rotational motions are concerned, OpenFAST underestimated the roll motion, while for pitch, the simulation is closer to measurements, as can be seen in Figure 6.12a and Figure 6.13a, respectively. In addition, the OpenFAST simulation for PSD for both roll and pitch, Figure 6.12b and Figure 6.13b, follows the shape of the measurements and is able to capture the peak happening at higher frequencies, which corresponds to the wave frequencies. For completeness, time series and power spectral densities for the other motions are presented in subsection B.2.2.

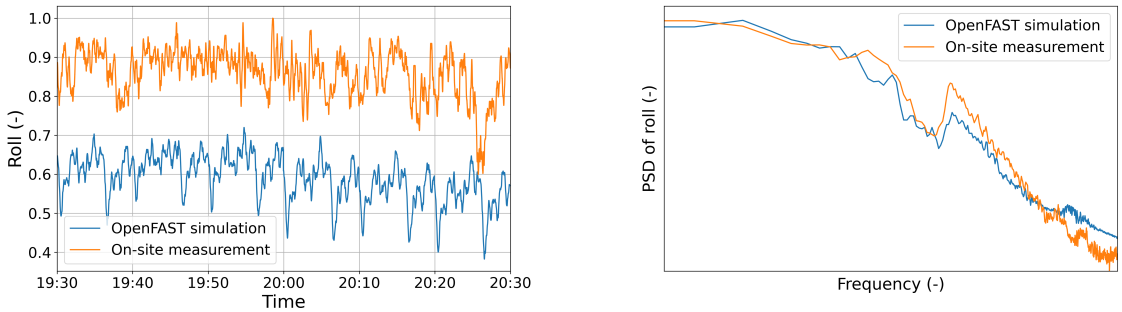

(a) Normalised roll time series

(b) Power spectral density of roll

Figure 6.12: Comparison of normalised platform roll time series (a) and power spectral density (b) between OpenFAST and on-site measurement in below rated region.

The generated power is presented in Figure 6.14. To begin with, the mean power is more accurately estimated compared to the cut-in region; however, there is still a difference. This can be attributed to the torque controller used in this region. As described in section 5.3, the same airfoils as the reference

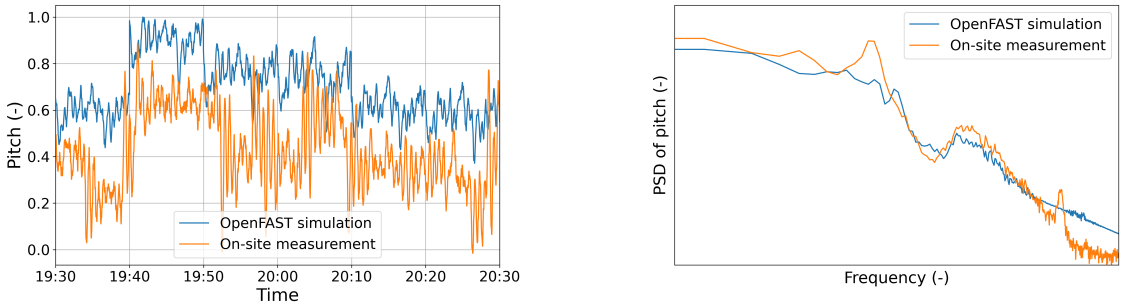

(a) Normalised pitch time series

(b) Power spectral density of pitch

Figure 6.13: Comparison of normalised platform pitch time series (a) and power spectral density (b) between OpenFAST and on-site measurement in below rated region.

NREL wind turbine were used. However, in the torque region, the power output is influenced by the rotor performance, as the controller tries to operate the wind turbine at the optimum tip speed ratio. The influence of this discrepancy on the total AEP will be further investigated in section 6.3.

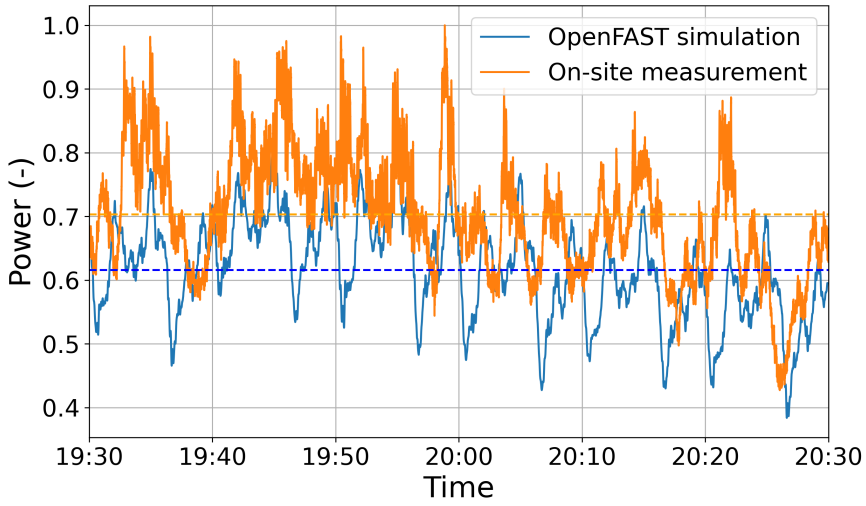

Figure 6.14: Comparison of generated power between OpenFAST and on-site measurement in below rated region.

6.2.3. Above rated region

The last region examined is the above rated region. The exact input parameters for this simulation are presented in Table 6.4.

Time	Wind speed (m/s)	TI (%)	Wind direction (°)	Wave direction (°)	Nacelle yaw (°)	Current speed (m/s)	Current direction (°)	Air density (kg/m³)
13:00:00	17.70	5.60	332.90	330.50	330.40	0.45	196.90	1.20
13:10:00	17.70	6.50	333.60	327.70	331.10	0.42	179.10	1.20
13:20:00	17.30	6.70	336.30	328.40	333.80	0.43	188.10	1.20
13:30:00	17.80	7.00	336.30	332.60	333.80	0.43	182.30	1.20
13:40:00	18.50	6.00	339.60	331.90	337.10	0.45	180.20	1.20
13:50:00	18.40	6.90	337.70	329.10	335.20	0.49	185.30	1.20

Table 6.4: Input parameters for OpenFAST simulations in above rated region.

In Figure 6.15 the average results for the time series comparison of all motions in the above rated region are presented. As can be observed, the standard deviations for OpenFAST model are similar with on-site measurements except for yaw motion where the on-site TetraSpar demonstrator seems to have a more stable behaviour. The highest difference for mean values happens for the sway motion.

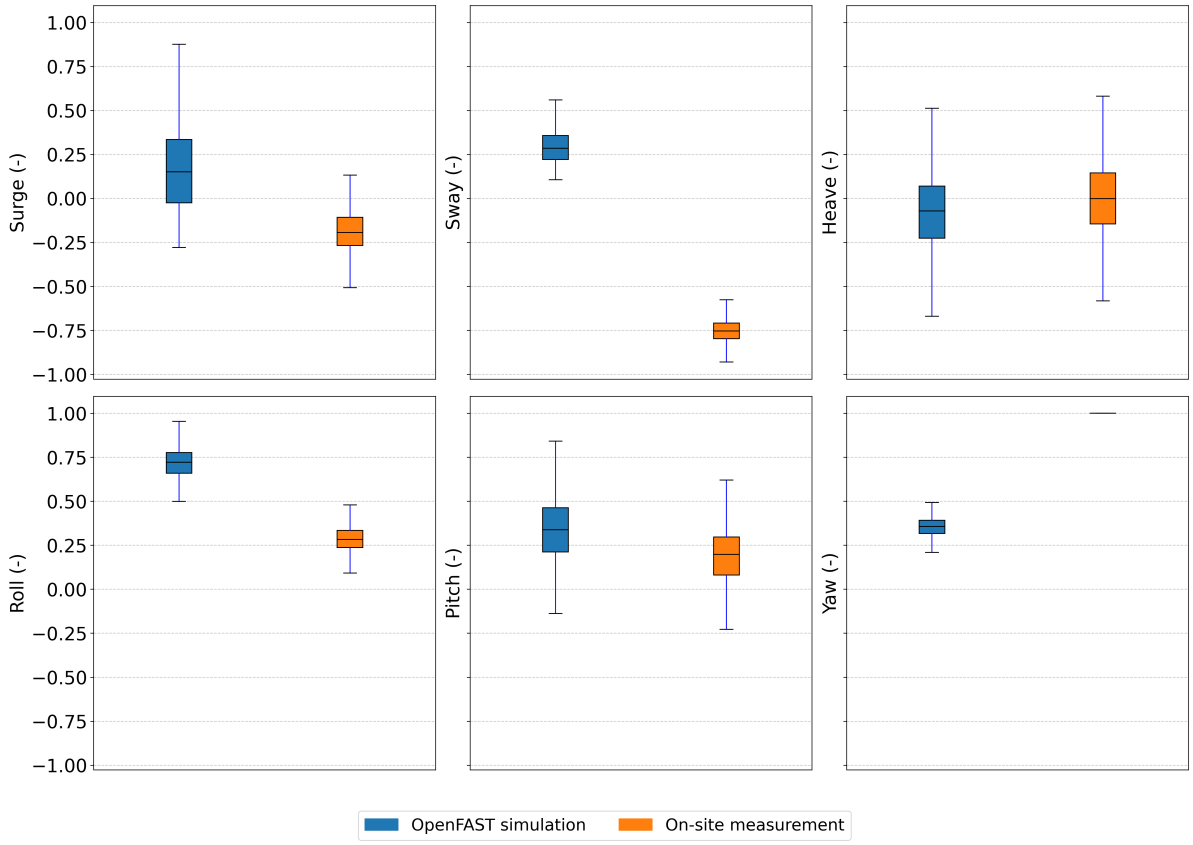

Figure 6.15: Normalised comparison between OpenFAST simulation and on-site measurements for all platform motions in above rated region.

As far as the spectral densities of translational motions are concerned, it is clear that the OpenFAST signal for surge (Figure 6.16a) and sway (Figure 6.16b) shows higher power spectral density at both low and high frequencies compared to the on-site measurements. Additionally, the OpenFAST signal is more stable in these regions. For the middle frequencies, the OpenFAST signal aligns more closely with the on-site measurements.

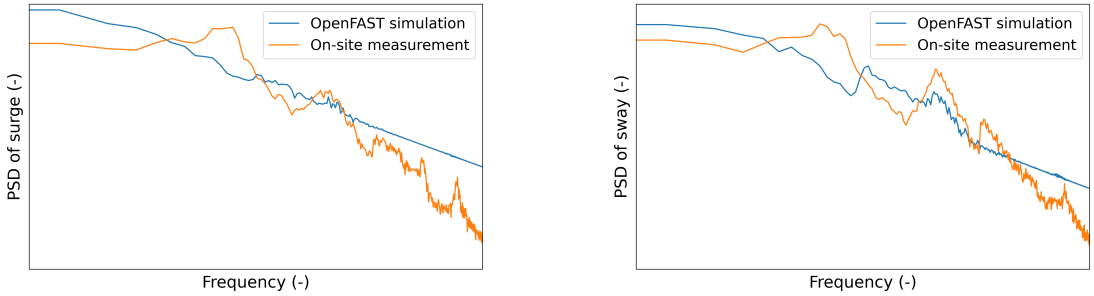

(a) Power spectral density of surge

(b) Power spectral density of sway

Figure 6.16: Comparison of power spectral density of surge (a) and sway (b) between OpenFAST and on-site measurement in above rated region.

As far as the rotational motions are concerned, OpenFAST overestimates the roll motion, while for pitch, the simulation is closer to measurements, as can be seen in Figure 6.17a and Figure 6.18a, respectively. In addition, the OpenFAST simulation for power spectral density of both roll and pitch, Figure 6.17b and Figure 6.18b, precisely follows the shape of the on-site measurements and captures the peak at higher frequencies corresponding to the wave frequencies. For the other platform motions results are given in subsection B.2.3.

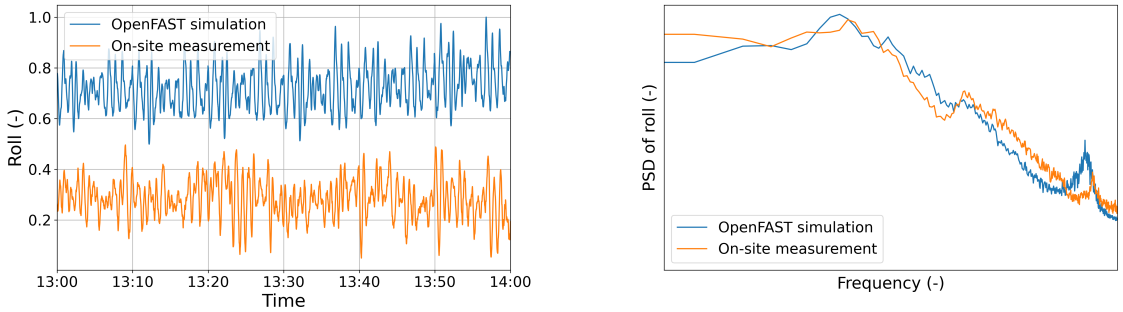

(a) Normalised roll time series

(b) Power spectral density of roll

Figure 6.17: Comparison of normalised platform roll time series (a) and power spectral density (b) between OpenFAST and on-site measurement in above rated region.

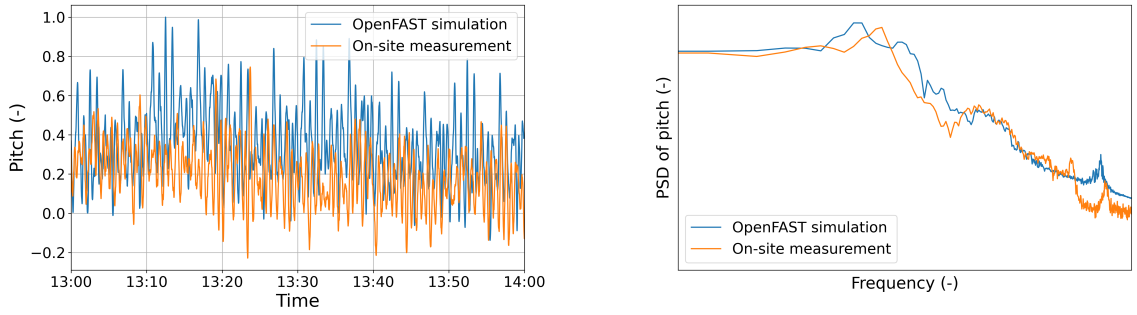

(a) Normalised pitch time series

(b) Power spectral density of pitch

Figure 6.18: Comparison of normalised platform pitch time series (a) and power spectral density (b) between OpenFAST and on-site measurement in above rated region.

The generated power in the above rated region is presented in Figure 6.19. To begin with, the mean power is accurately estimated by the model. However, there are higher deviations compared to the measurements. The most important reason for this is the controller. As has been explained before, the unavailability of information for the TetraSpar controller due to confidentiality by the wind turbine manufacturer makes it difficult to tune the model to match exactly the on-site demonstrator. In addition, the TurbSim files used in the simulations impact the wind energy production rate, leading to variations in power generation per simulation time step. However, the mean wind speed is the same, resulting in the same power production when looking at average conditions. These average conditions are of greater interest for energy yield estimation rather than the per-second variations. To sum up, the mean power is accurately predicted by OpenFAST, even though it has higher deviations which can be attributed to the unknown information about the controller and the generated TurbSim file.

6.3. Power curve and AEP estimation

The previous section was useful for estimating the motion and power output of the TetraSpar demonstrator over a specific time period with certain metocean conditions. However, the main scope of this project is to estimate the AEP and compare it with on-site measurements. For this reason, the measured data at 25 Hz were averaged over 10-minute periods for an entire year. As reference

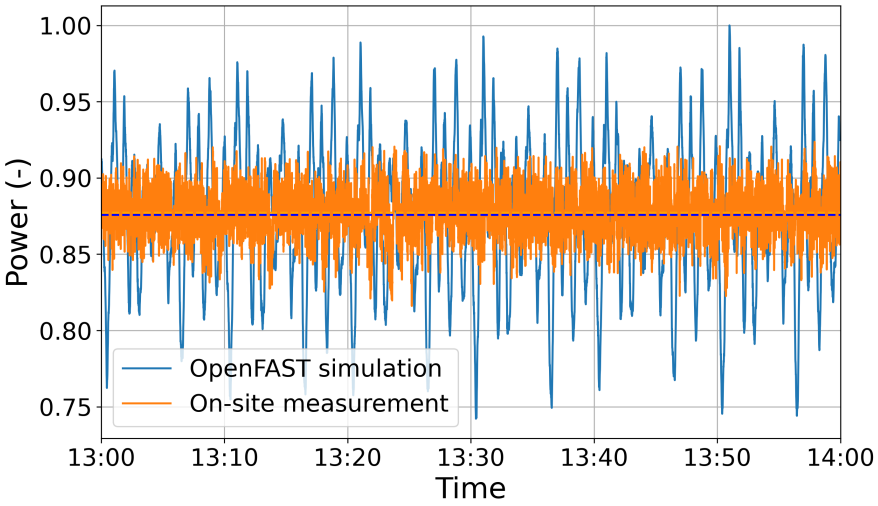

Figure 6.19: Comparison of generated power between OpenFAST and on-site measurement in above rated region.

year 2023 was used, when the TetraSpar demonstrator is in full operation. To estimate the AEP, the probability of occurrence for each wind speed needs to be determined. Therefore, the averaged 10-minute periods were categorised into wind speed bins, for the entire operating range of the wind turbine. Consequently, the probability of occurrence for each wind speed bin is presented in Figure 6.20. Due to confidentiality, x-axis has been normalised.

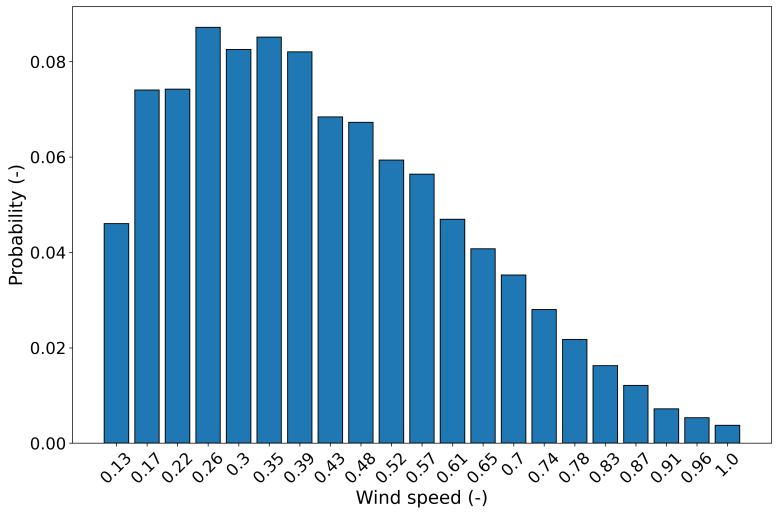

Figure 6.20: Probability distribution for each normalised wind speed at the TetraSpar location.

To perform simulations in OpenFAST for each wind speed, specific parameters such as wind direction, significant wave height, wave period, TI and others should be given as inputs. These data should be the most representative for each wind speed. Thus, the averaged data were grouped into wind speed bins covering the entire operating region of the wind turbine. Next, for each dataset, the most representative value was identified for each wind speed bin by counting the number of occurrences and transforming them into probabilities. An example of the above method is presented in Figure 6.21 for the significant wave height (H_s) and a specific wind speed bin. Due to confidentiality, the x-axis has been normalised. After estimating the most frequent value of occurrence for each parameter and wind speed, the values were extracted and used as inputs in OpenFAST in order to simulate the average conditions of the location of TetraSpar and estimate the AEP.

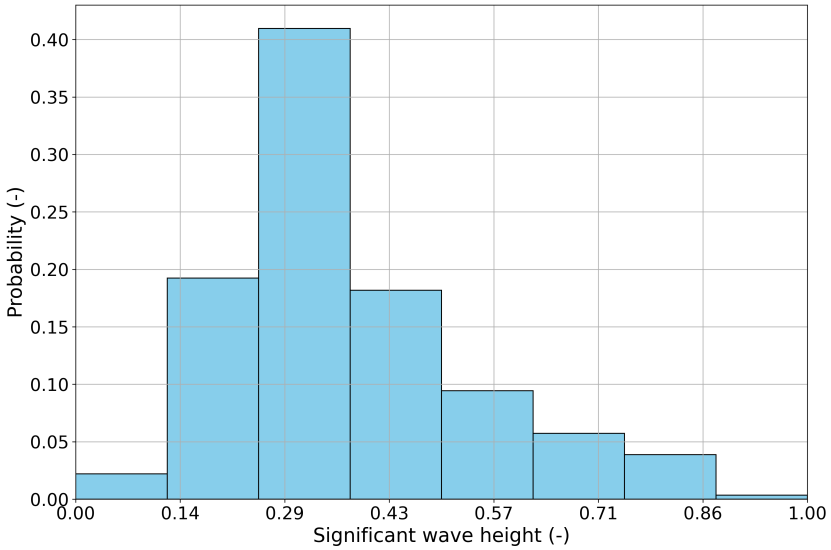

Figure 6.21: Probability distribution of significant wave height for a specific wind speed bin.

In order to compare the OpenFAST power curve with the on-site power curve, the measured data of generated power for the entire 2023 were filtered. Firstly, the dataset was cleaned by removing any 10-minute period with missing values for wind speed or power. Secondly, specific filtering was applied to filter unrealistic or erroneous data points based on thresholds for wind speed and power output. These conditions excluded points where the relationship between power and wind speed was out of the expected operating ranges, for instance, extremely low power in above rated conditions. Thirdly, another filtering was applied to filter outliers based on standard deviation. To achieve this, the average power and standard deviation at each wind speed were estimated. Power values that deviated more than two standard deviations from the calculated average were excluded. To summarise, the averaged 10-minute periods for the entire year of 2023 were further filtered in order to exclude erroneous or unrealistic power values and outliers with a great standard deviation from the mean power. The resulting power curve is illustrated in Figure 6.22.

Additionally, the power curve for the OpenFAST model is also presented in Figure 6.22, both for the FOWT, which corresponds to the TetraSpar demonstrator model, and the fixed-bottom wind turbine, to compare the AEP. The power curve for the fixed-bottom wind turbine was produced by disabling all platform motions in OpenFAST. Moreover, not the full operating region is depicted and the axes were normalised due to confidentiality. As can be observed when comparing the power curves for the FOWTs, the model simulates the above rated region effectively. However, in the below rated region and near cut-in, there is a noticeable difference between the power curves. This can be attributed to the fact that in the below rated region, the torque controller is applied and the power production is influenced by the rotor characteristics. As explained in subsection 5.3.4, the same airfoils and the same C_p, C_t and C_q tables were applied as the NREL 5 MW due to limited information about the TetraSpar wind turbine. As a result, this region is expected to have the largest differences. On the other hand, in above rated conditions, the controller maintains the rated power by pitching the blades. Consequently, this region is less influenced by the uncertainties of the wind turbine.

For the OpenFAST simulation (FOWT) curve, a peak shaving level of 80% was applied. This level was chosen based on the simulated OpenFAST power curve to achieve a similar power reduction in the near rated region as the on-site power curve. This comparison was made for the OpenFAST fixed-bottom power curve and the actual power curve provided by the wind turbine manufacturer, which is not disclosed due to confidentiality

To compare the annual energy yield for the three cases, AEP produced at each wind speed is presented in Figure 6.23. Due to confidentiality, the axes are presented without values and not all operating wind speeds of the turbine are shown. When comparing the model with the on-site demonstrator, the OpenFAST model underestimates the annual energy yield production, a result that is expected based

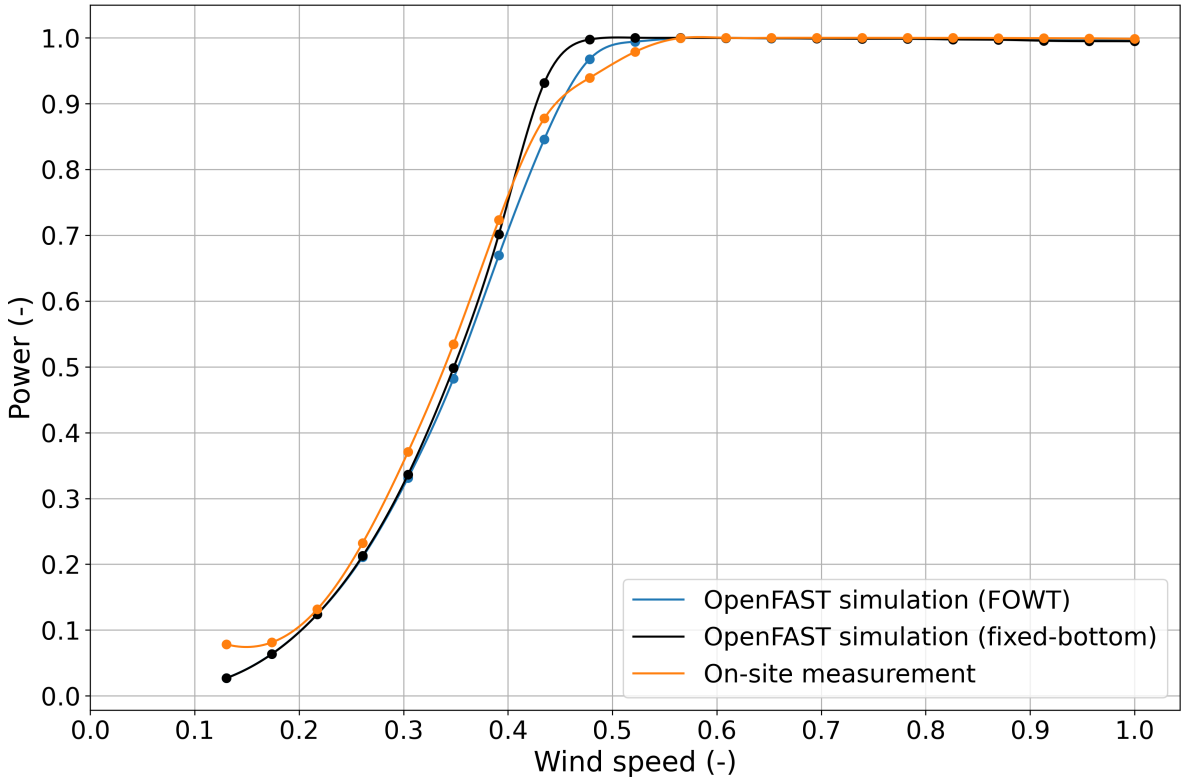

Figure 6.22: Power curve comparison between the OpenFAST simulation (blue) and on-site measurement (orange). The fixed-bottom wind turbine power curve (black) is also depicted for comparison.

on the power curve. In near rated conditions and above rated, similar AEP is produced in both cases. For the comparison of AEP between the TetraSpar demonstrator and the fixed-bottom turbine, the fixed-bottom turbine produces more energy yield in the range below rated and up to rated wind speeds. After rated wind speed, similar AEP is expected.

Finally, by summing the AEP at each wind speed, the total AEP can be estimated. In Table 6.5 the total AEP estimated by the OpenFAST model is compared with on-site measurement and the fixed-bottom simulation. As can be seen, the OpenFAST TetraSpar model underestimates the AEP produced by 2.8%, while the AEP produced by the OpenFAST model is 3.6% lower compared to the fixed-bottom wind turbine.

Comparison of OpenFAST TetraSpar model	Percentage difference (%)
On-site measurement	-2.8
OpenFAST simulation (fixed-bottom)	-3.6

Table 6.5: AEP percentage differences between the OpenFAST TetraSpar model and on-site measurement, as well as between the OpenFAST TetraSpar model and the fixed-bottom wind turbine simulation.

6.3.1. Effect of controller tuning on the power curve and AEP

In previous section, the AEP of the OpenFAST model was estimated based on tuning the ROSCO controller with peak shaving level of 80%. Since there was not information provided about the controller tuning techniques followed by the wind turbine manufacturer, different peak shaving levels were utilised to examine how the power generation changes. The peak shaving levels implemented apart from the 80% were 75%, 90% and without peak shaving. The results for the power curves are presented in Figure 6.24.

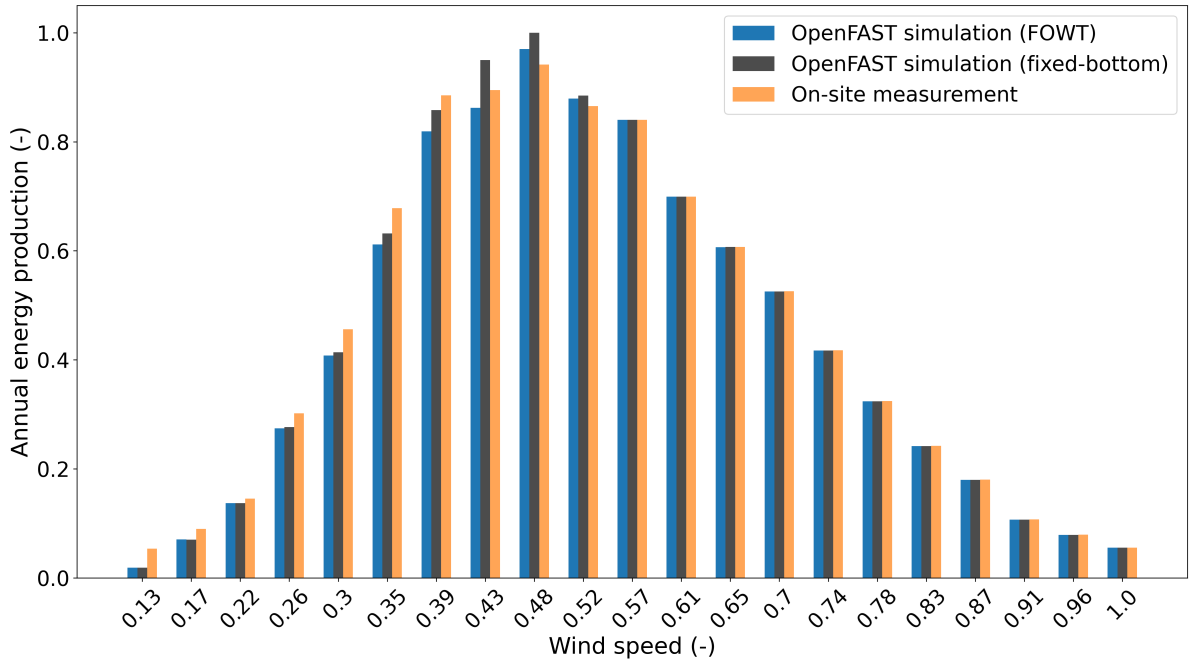

Figure 6.23: Annual energy yield comparison per wind speed bin between the OpenFAST simulation and on-site measurement. The fixed-bottom wind turbine is also depicted for comparison.

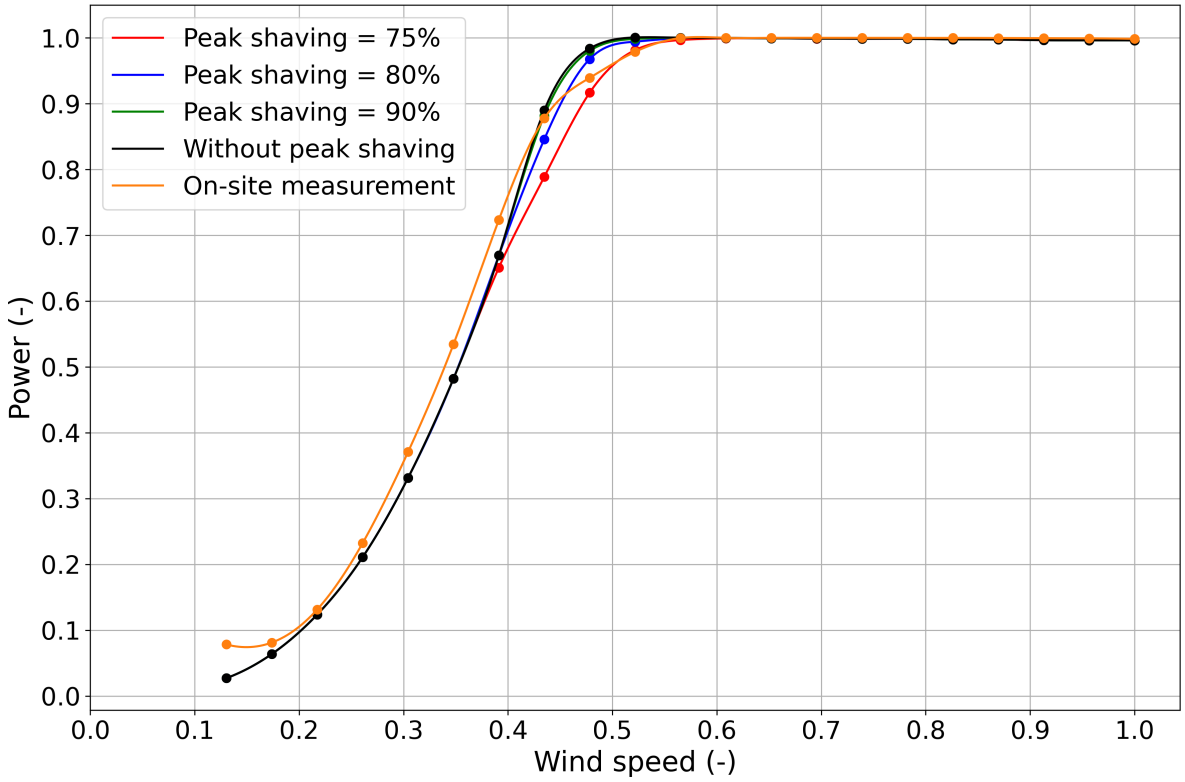

Figure 6.24: Power curve comparison between OpenFAST model and on-site measurement for different peak shaving levels.

As can be observed, peak shaving affects the power curve near the rated wind speed, while above and below the rated wind speed, the generated power remains unchanged. Additionally, the 90% peak shaving level has no significant influence on the produced power compared to the case when

no peak shaving is used. From 80%, the influence of peak shaving becomes more apparent, while using a peak shaving level of 75% leads to significant power reduction. The percentage difference in generated power between the different peak shaving levels and the on-site measured data is shown in Figure 6.25.

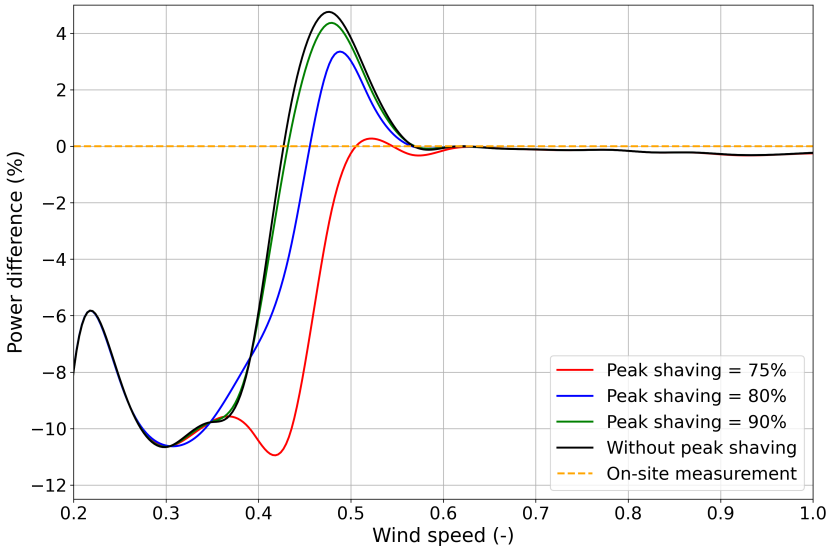

Figure 6.25: Power percentage difference between on-site measurement and OpenFAST simulation for different peak shaving levels.

The effect of peak shaving is also illustrated in Figure 6.26 for simulations at wind speed near the rated value. The figure reveals that a 75% level of peak shaving results in a lower mean power output compared to the other levels of peak shaving. The general trend of power fluctuations remains unchanged, though there is a shift in the power curve to lower values.

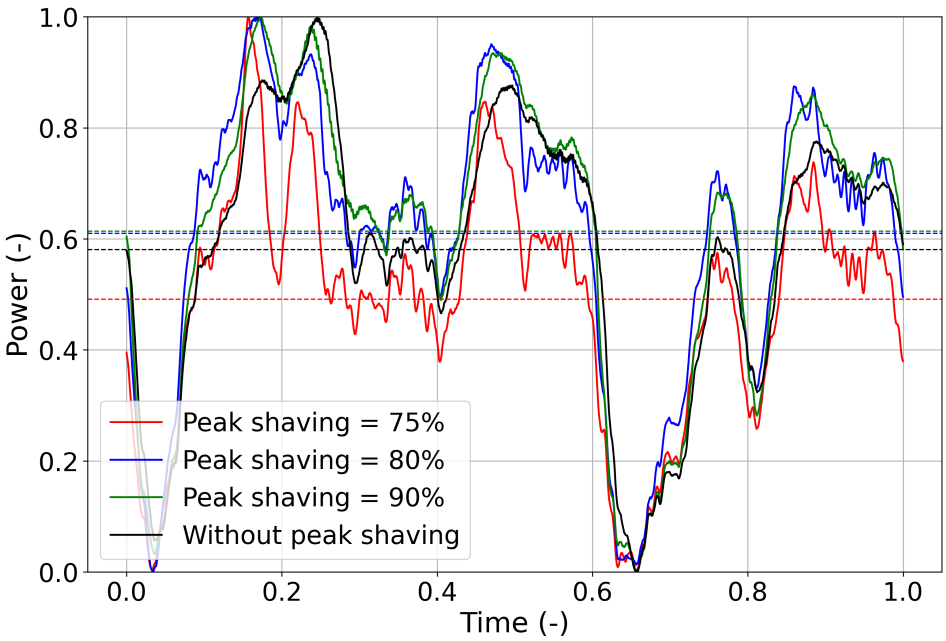

Figure 6.26: Comparison of generated power time series for different peak shaving levels near the rated wind speed.

After the estimation of power curve, the AEP was calculated for the different peak shaving levels and compared with on-site measurements. The results are summarised in Table 6.6, which shows the percentage difference in AEP between on-site measurements and simulations with peak shaving

levels of 75%, 80%, and 90%, as well as a scenario without peak shaving. The scenario with 75% underestimates the AEP by 4.4%, while the scenario without peak shaving shows the lowest difference with underestimation of 2.1%. For the other two levels, 80%, and 90%, the underestimation percentage is 2.8% and 2.3%, respectively.

	Peak shaving level	Difference (%)
On-site measurement	Peak shaving = 75%	-4.4
	Peak shaving = 80%	-2.8
	Peak shaving = 90%	-2.3
	Without peak shaving	-2.1

Table 6.6: Percentage difference between the AEP of on-site measurement and different peak shaving levels.

Apart from the influence of the peak shaving level on power production, the effect of the floating feedback and the wind speed estimator were also investigated by simulating a case without floating feedback and no wind speed estimator. For both simulations the same peak shaving level of 80% was used. The absence of wind speed estimator lead to a decrease in AEP by 1%, while the absence of floating nacelle feedback lead to minor change in AEP less than 0.5%.

6.4. Platform motions

In the previous section, the AEP was estimated based on different peak shaving levels. This section focuses on analysing platform motions. As previously explained, OpenFAST simulations were conducted with average conditions for each wind speed. Consequently, the wind direction varied for each wind speed simulation, covering the representative wind direction for each wind speed. However, wind direction significantly influences the excitation of platform motions. For instance, wind coming from the east, which aligns with the OpenFAST surge axis, primarily excites surge and pitch motions, while other motions are less affected. Conversely, wind from the south, corresponding to the sway axis, mainly excites sway and roll motions. Thus, simulating average on-site conditions with varying wind directions can yield different pitch motion results for the same wind speed.

For the estimation of average pitch motion based on the on-site measurements, all 10-minute periods over the entire 2023 were used. These measurements were based on wind speeds from various directions, which did not only excite the pitch motion. To estimate the mean pitch motion for every wind speed in OpenFAST, all 10-minute periods would need to be used. However, this is impractical, so an alternative approach was adopted to compare the average response of the on-site TetraSpar demonstrator with the OpenFAST model. More specifically, the magnitude of roll and pitch angles, θ_{roll} and θ_{pitch}, was used (Equation 6.1). Since roll and pitch are orthogonal (90 degrees apart) and their magnitude is independent of wind direction, using this magnitude provides a suitable basis for comparing the OpenFAST model's motion with the TetraSpar demonstrator.

$$\text{Magnitude} = \sqrt{\theta_{\text{roll}}^2 + \theta_{\text{pitch}}^2} \tag{6.1}$$

As can be observed from Figure 6.27a, if no peak shaving is applied, the platform experiences higher motion in the region before the rated wind speed. In the regions both below and above rated wind speed, different peak shaving levels have no significant effect on the platform motion. Among the various peak shaving levels, the 90% peak shaving level shows the smallest difference in the maximum roll and pitch magnitude when compared to the on-site measurement. In the region below rated wind speed, the model tends to slightly underestimate the motion, while in the region above the rated wind speed, the OpenFAST model overestimates it. Specifically, it appears that the model's magnitude remains nearly constant, whereas the on-site demonstrator shows a decreasing trend. This discrepancy can primarily be attributed to differences in the controller and the wind turbine's shutdown mechanism. Overall, the OpenFAST model exhibits a similar roll and pitch magnitude compared to the on-site measurement, with the greatest differences occurring in the region above rated wind speed.

Apart from mean magnitude, the standard deviation is is also presented in Figure 6.27b. As shown, the effect of peak shaving levels on the standard deviation is similar to that on the mean magnitude.

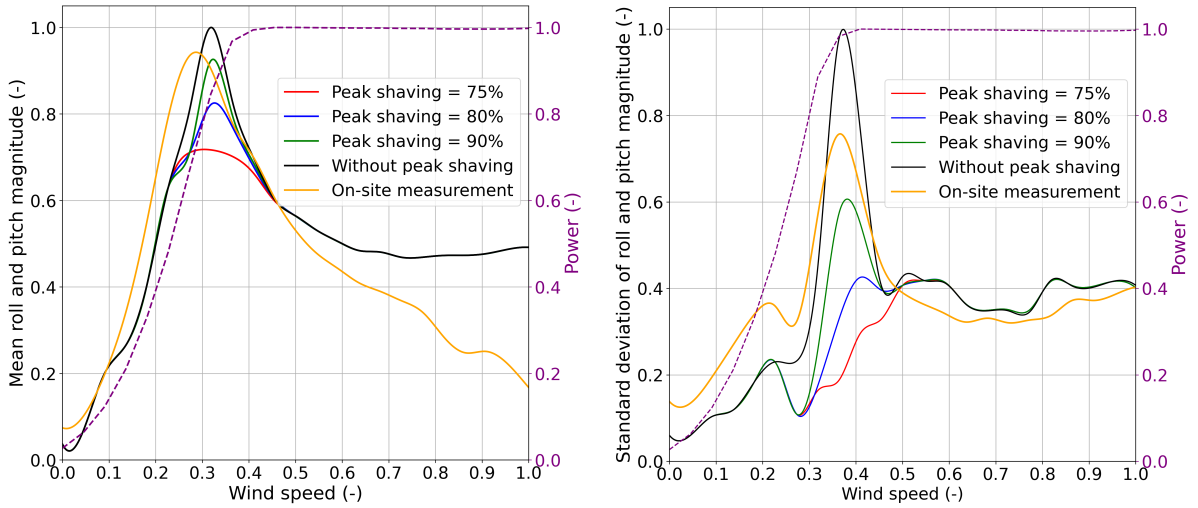

(a) Mean roll and pitch magnitude

(b) Standard deviation of roll and pitch magnitude

Figure 6.27: Comparison of normalised mean roll and pitch magnitude (a) and standard deviation of roll and pitch magnitude (b) between OpenFAST model and on-site measurement for different peak shaving levels. The normalised power curve is also displayed.

For the OpenFAST model, the standard deviation is underestimated in the region below the rated wind speed and overestimated in the region above the rated wind speed. Despite these discrepancies, the overall trend remains consistent: the standard deviation increases up to the rated wind speed, then decreases abruptly and remains constant until the cut-out wind speed. To summarise, the OpenFAST model exhibits similar trends in standard deviation compared to the on-site platform.

The above method was used to compare the platform motion of model with the on-site demonstrator. However, to investigate the influence of wind speed on each platform motion separately, especially on the surge and pitch motions, OpenFAST simulations with wind direction aligned with the positive surge axis were performed for each wind speed. The results for the surge and pitch platform motions, which are dominant in power generation, are presented in Figure 6.28 and Figure 6.29, respectively. Due to confidentiality, only the mean values of on-site measurements are depicted for comparison.

It can be observed that the model underestimates the mean surge motion. However, the general trend is similar, with surge reaching its maximum near the rated wind speed and then decreasing. As for the pitch motion, the model agrees better in conditions below the rated wind speed. However, after the rated wind speed, the pitch motion of the on-site demonstrator decreases, while the OpenFAST model tends to be more stable.

6.5. Inconsistencies in OpenFAST model performance

In this chapter, the AEP and the motion of the OpenFAST model were investigated and compared to the on-site measurements. Even though the model approximates both the AEP and platform motion effectively, there are some inconsistencies. These arise mainly from assumptions made for the unknown data and the simplifications employed in OpenFAST itself. These limitations, collectively attributed to a reduction in the precision of the developed model, are analytically addressed below.

To begin with, the confidentiality regarding the wind turbine of the TetraSpar demonstrator led to significant assumptions. The most important parameters that influence the performance of the model are the airfoil profile and distribution. Thus, the same airfoils as the NREL 5 MW wind turbine were used. In addition, specific parameters regarding gearbox and generator efficiencies were also assumed to be the same as the reference wind turbine. Mass and stiffness of the blades and tower were based on internal data, leading to variations in their center of gravity and affecting the response of the model.

A high influence on the generated power and the platform stability also comes from the controller, for which no information was available. For this reason, different tuning techniques, such as the peak

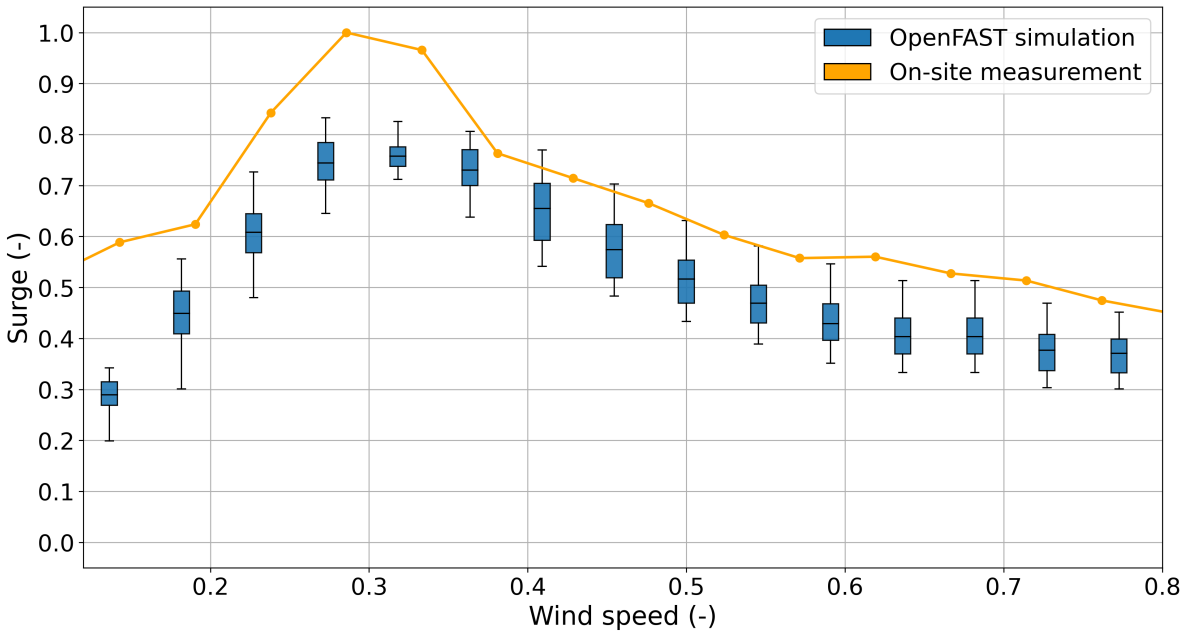

Figure 6.28: Comparison of normalised surge platform motion between the OpenFAST model and on-site measurement for different wind speeds. Zero incoming wind used for OpenFAST simulation.

shaving level, were examined to assess their influence on the model. For the estimation of the floating nacelle feedback, the generic tuning procedure provided by ROSCO was followed, an area that could be further investigated. Another limitation of the controller is the absence of yaw control. In addition, the startup and shutdown procedures may differ from those used on the on-site TetraSpar demonstrator. However, these aspects were not examined in detail, as they have a negligible impact on the estimation AEP, which is the primary focus of this project.

Apart from the wind turbine itself, simulating metocean conditions also affects the model's behaviour. First, for wind simulation, the 10-minute average wind speed and mean turbulence were used to generate turbulent time series, resulting in a wind profile that cannot match exactly the same as the on-site location. Additionally, LiDAR can overestimate the average wind speed if no motion compensation is applied, due to the upward displacement of the LiDAR beams (Garcia-Sagrado et al., 2024). Second, wave and current modelling can introduce inconsistencies into the model. For waves, the measured elevation time series were used with a 10-minute average direction for the one-hour simulations. However, for estimating the power curve, statistical data such as significant wave height and wave period were used to generate irregular waves based on the JONSWAP spectrum. For currents, a simple subsurface model (power law profile) was implemented in OpenFAST. Creating a depth-varying current profile based on measurements would require recompiling OpenFAST, a time consuming procedure. Therefore, this simplification was adopted to include current effects in the model.

Furthermore, the exclusion of potential flow theory and the use of strip theory in the OpenFAST HydroDyn module results in significant inaccuracies. Potential flow theory is essential for capturing complex wave-body interactions and the resulting hydrodynamic forces on the FOWT structure. Neglecting these interactions leads to less accurate estimates of motion and loading, causing potential errors in model predictions. Additionally, neglecting second-order effects, such as drift and nonlinear wave forces, can lead to discrepancies in the model. Drift describes the gradual movement of a floating structure in the direction of wave propagation, driven by the cumulative impact of the waves. This response is influenced by higher-order wave amplitudes and is essential for accurately forecasting the behaviour of floating platforms.

Another limitation is that the floating platform, consisting of the floater, suspension lines and the keel, was modelled as a six DOF rigid body in the HydroDyn module. However, in reality, the keel and floater can move independently due to the connection of the suspension lines. Since this report does not focus

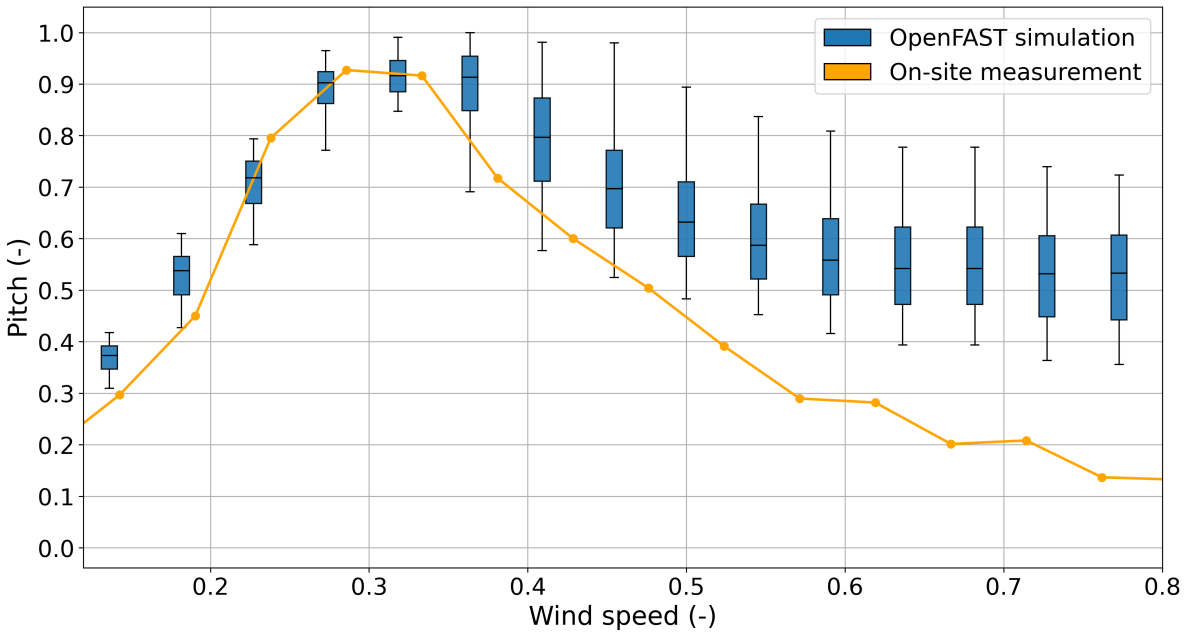

Figure 6.29: Comparison of normalised pitch platform motion between the OpenFAST model and on-site measurement for different wind speeds. Zero incoming wind used for OpenFAST simulation.

on estimating loads within the structure's beams, such as bending moments, and because there are no significant deviations in response between the rigid body and flexible model, as found by Thomsen et al. (2021), the rigid body assumption was used for the entire floating platform. In addition, marine growth, which affects hydrodynamic behaviour, was neglected. Last but not least, the complexity of the mooring system, consisting of six different segments and four different line types, combined with the limitations of OpenFAST regarding the absence of nonlinear elastic properties, can also impact the accuracy of the model (Hall, 2015).

To summarise, the comparison of motion of the OpenFAST model with on-site TetraSpar demonstrator, revealed some inconsistencies primarily due to assumptions and simplifications. Key assumptions include the use of NREL 5 MW wind turbine for missing data in the wind turbine modelling and the use of ROSCO controller, since no information was available due to confidentiality. Additionally, modelling limitations, such as the use of a rigid body for the floating platform and simplified waves and currents conditions, contributed to discrepancies in the model's predictions.

7

Impact of waves and currents on the TetraSpar demonstrator motion and power production

In this chapter, the effect of different sea states on the generated power and motion of the TetraSpar demonstrator is presented. Firstly, in section 7.1, the effect of waves with different significant wave heights, periods and directions is investigated, while in section 7.2, the effect of currents is examined.

7.1. Impact of waves

The characteristics of waves such as the significant wave height and wave period influence the motion of FOWTs and as a result the generated power. In subsection 7.1.1 the effect of three different significant wave heights with same period is investigated, while in subsection 7.1.2 three different wave periods are examined. To account for the influence of wind-wave misalignment on the power production, an analysis is made in subsection 7.1.3.

For the analysis, the TetraSpar OpenFAST model was subjected to different steady winds for all operating wind speeds. The reason for not using turbulent wind, despite its prevalence in real conditions, was to minimise the influence of wind and focus on the effect of sea states. Additionally, the direction of the steady wind, waves and currents was set to 0° in order to examine the effects on surge and pitch motion, which affect power production the most, as found in chapter 3. For this reason, the primary focus of the results will be on these two motions. Furthermore, a controller with peak shaving level of 80% was implemented for the simulations and the JONSWAP spectrum was utilised for generating irregular waves in OpenFAST. The results were normalised due to confidentiality. The normalisation process scales data values to a range between 0 and 1 using global minimum and maximum values across all datasets, ensuring consistent comparison. Wind speeds were similarly normalised to adjust their positions on the plot.

7.1.1. Wave height

For the investigation of the influence of wave height, three different cases were examined with significant wave heights (H_s) of 2 m, 4 m and 8 m. All cases have the same wave period (T_p) of 8 seconds, which is the representative of the location of TetraSpar (Garcia-Sagrado et al., 2024). For the current, a subsurface profile was used in OpenFAST with a representative value of the location, which is not disclosed due to confidentiality.

As can be observed from Figure 7.1a, the mean values of surge motion follow an almost linear increase for all wave heights until the rated wind speed of around 0.4 on the normalised wind speed axis. This trend occurs because, until this point, the wind turbine experiences the greatest thrust, as can be seen from the dashed lines. Following this, the mean values decrease until the normalised wind speed of

around 0.8 and then remain almost constant. One cause for this is the activation of the pitch controller after the rated wind speed, leading to a reduction in the aerodynamic load. As far as the effect of significant wave height is concerned, the higher the significant wave height, the higher the mean value and standard deviation of platform surge.

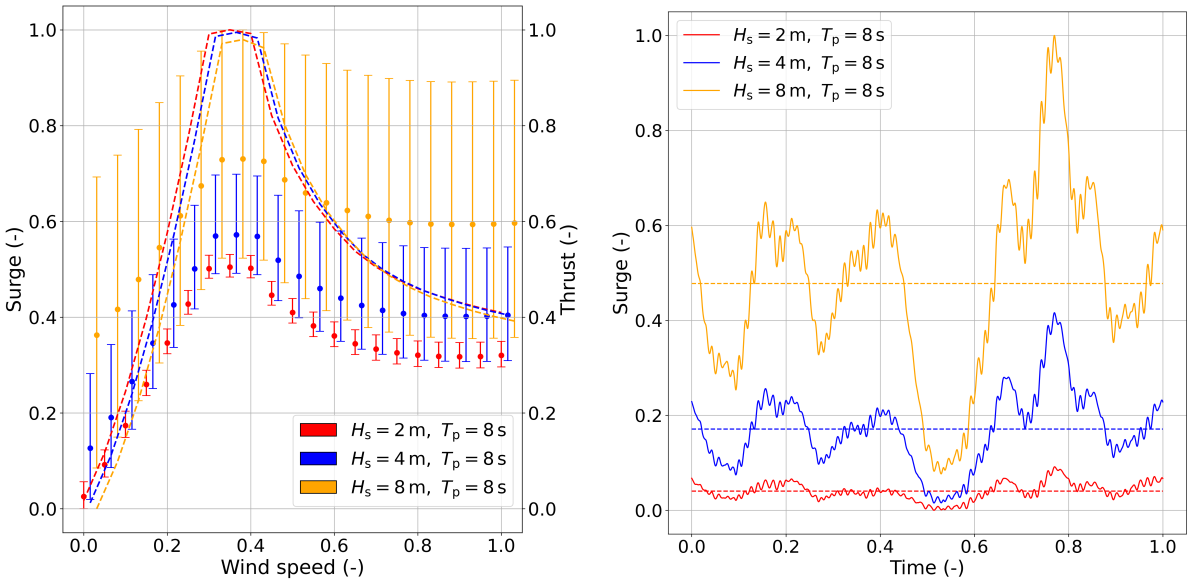

(a) Platform surge statistical analysis

(b) Platform surge time series

Figure 7.1: Statistical analysis of platform surge (a) and time series (for near rated wind speed) (b) for significant wave heights of $H_s = 2$ m, $H_s = 4$ m and $H_s = 8$ m with $T_p = 8$ s. The thrust is also shown in (a) with dashed lines.

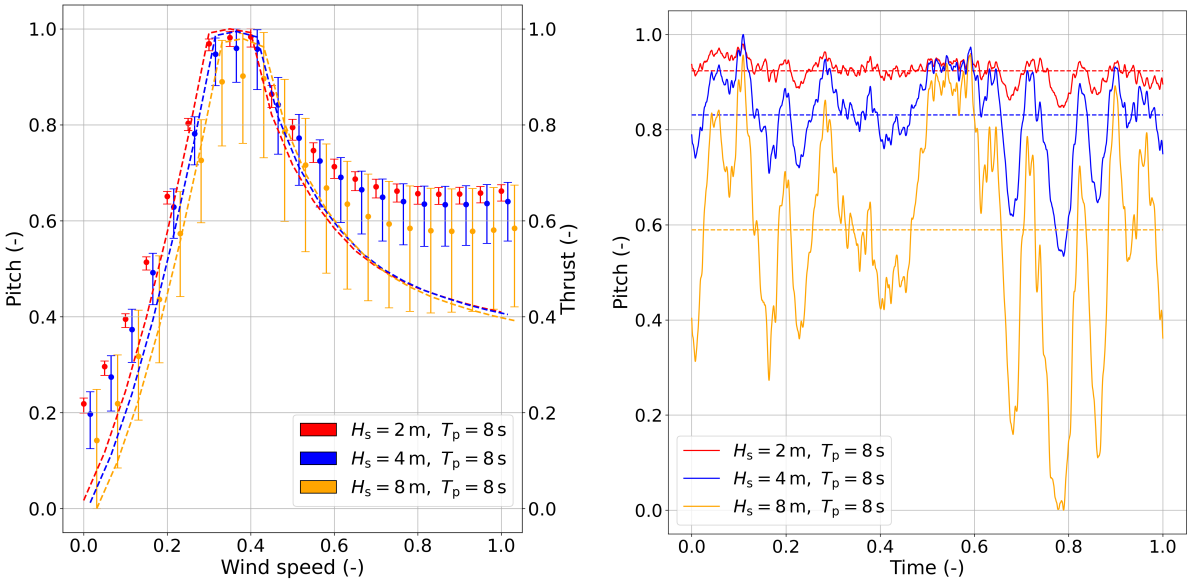

(a) Platform pitch statistical analysis

(b) Platform pitch time series

Figure 7.2: Statistical analysis of platform pitch (a) and time series (for near rated wind speed) (b) for significant wave heights of $H_s = 2$ m, $H_s = 4$ m and $H_s = 8$ m with $T_p = 8$ s. The thrust is also shown in (a) with dashed lines.

A similar pattern follows the pitch motion as can be seen in Figure 7.2a. However, in pitch motion, the lower wave height leads to higher values of mean pitch. This happens because as waves move toward the surge direction, the platform encounters increased hydrodynamic loads. These stronger wave-induced forces create a counteracting moment that partially balances the wind thrust-induced

moments around the floating offshore wind turbine structure's center of rotation. This counteracting torque mitigates the aerodynamic torque resulting from rising wind speeds, leading to a decrease in the platform's pitch. The above are also visible in Figure 7.1b and Figure 7.2b.

As far as the generated power is concerned, the mean values of generated power remain almost constant across all wave heights. However, the standard deviation of the generated power increases with rising wave height, as can be observed from Figure 7.3a. In addition, the oscillations shown in Figure 7.3b are caused mainly by the platform motion, as the wind speed is steady. This behaviour can be attributed to the fact that higher wave heights induce greater oscillations in both the surge and pitch motions of the platform. These increased oscillations lead to larger variations in the platform's position and orientation, resulting in a reduction in the apparent wind speed to the turbine due to negative velocities in pitch or surge, which in turn leads to a higher standard deviation in the produced power. Essentially, the higher the significant wave height, the more pronounced the fluctuations in the platform's motion, causing greater variability in the power output.

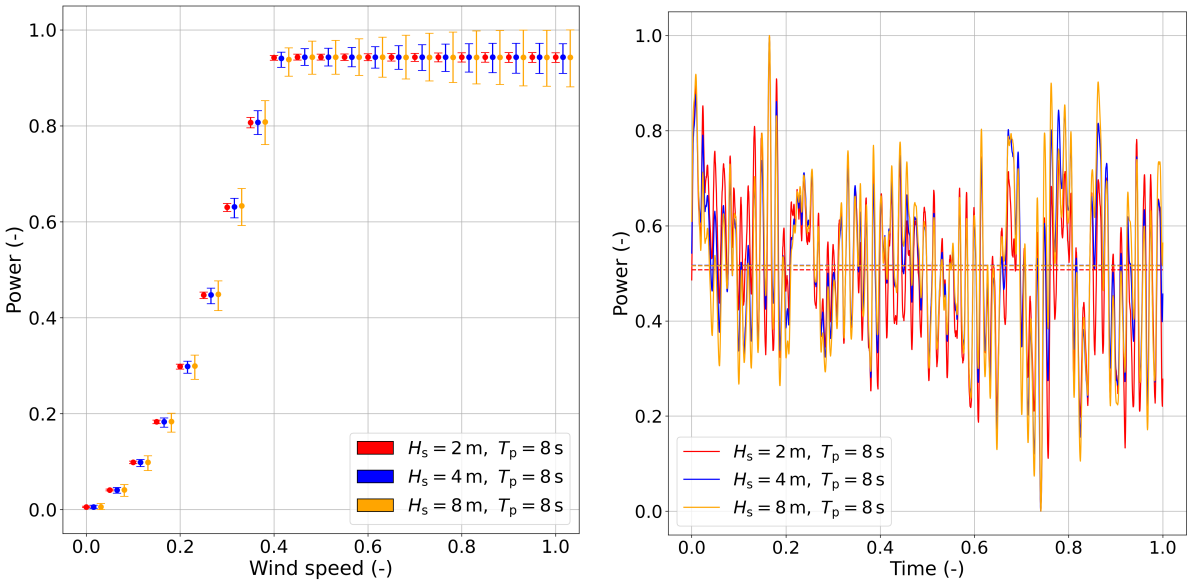

(a) Generated power statistical analysis

(b) Generated power time series

Figure 7.3: Statistical analysis of generated power (a) and time series (for near rated wind speed) (b) for significant wave heights of $H_s = 2$ m, $H_s = 4$ m and $H_s = 8$ m with $T_p = 8$ s.

To summarise, the effects of significant wave heights (H_s) of 2 m, 4 m and 8 m on TetraSpar motion and generated power with a wave period (T_p) of 8 s were examined. Higher wave heights led to increased mean values and standard deviations in platform surge, while in pitch motion, the mean values decreased with higher wave heights. The generated mean power remained almost constant across wave heights, but its standard deviation increased due to greater oscillations in platform motions.

7.1.2. Wave period

After investigating the influence of wave height on platform motion and generated power, the effect of wave period was also examined. For this purpose, three different wave periods were investigated, $T_p = 4\,s$, $T_p = 8\,s$ and $T_p = 10\,s$, with a significant wave height of $H_s = 2\,m$, which is representative of the TetraSpar location (Garcia-Sagrado et al., 2024). The results for surge and pitch motions are presented in Figure 7.4a and Figure 7.4b, respectively.

The observed trends for different wave periods are similar to those for varying significant wave heights. For both platform surge and pitch, the mean values increase until reaching the rated wind speed, then decrease, stabilising after the midpoint of the above rated wind speed region. As the wave period increases, both the mean value and standard deviation of surge also increase. In contrast, for platform pitch, the mean value decreases with longer wave periods, while the standard deviation increases, mirroring the trends observed with increasing significant wave heights.

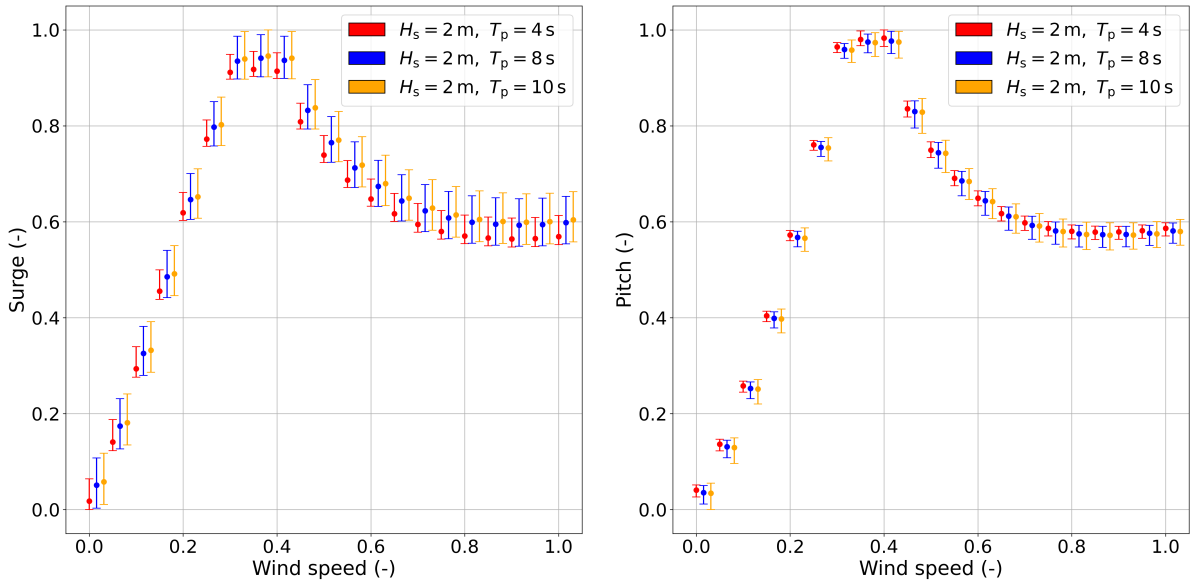

(a) Platform surge statistical analysis

(b) Platform pitch statistical analysis

Figure 7.4: Statistical analysis of platform surge (a) and pitch (b) for wave periods of $T_p = 4$ s, $T_p = 8$ s and $T_p = 10$ s with $H_s = 2$ m.

Regarding the generated power, the mean values exhibit a consistent behaviour across different wave periods, indicating that the average power output does not significantly vary with changes in wave period (Figure 7.5). However, while the mean values are stable, the variability in power output, as indicated by the standard deviation, increases. Moreover, compared to cases with varying significant wave heights, the increase in standard deviation across different wave periods is less. This suggests that the influence of wave period on the fluctuations in power output is not as significant as the impact of wave height.

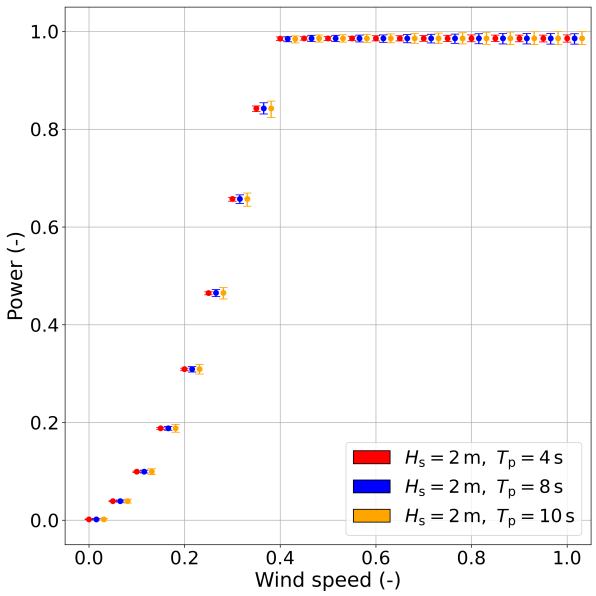

Figure 7.5: Statistical analysis of generated power for wave periods of $T_p = 4$ s, $T_p = 8$ s and $T_p = 10$ s with $H_s = 2$ m.

Overall, the effect of significant wave height and wave period on TetraSpar motion and generated power have similar effect. Larger wave heights and periods resulted in higher mean values and greater standard deviations for platform surge. In contrast, for pitch motion, higher wave heights

were associated with lower mean values. Although the generated power was nearly consistent across varying wave heights, its standard deviation grew due to increased oscillations in the platform's movements. Last but not least, the effect of increasing significant wave height with a period of $T_p = 8$ s is greater than the effect of increasing wave period with a constant wave height $H_s = 2$ m. The above is illustrated in Figure 7.6.

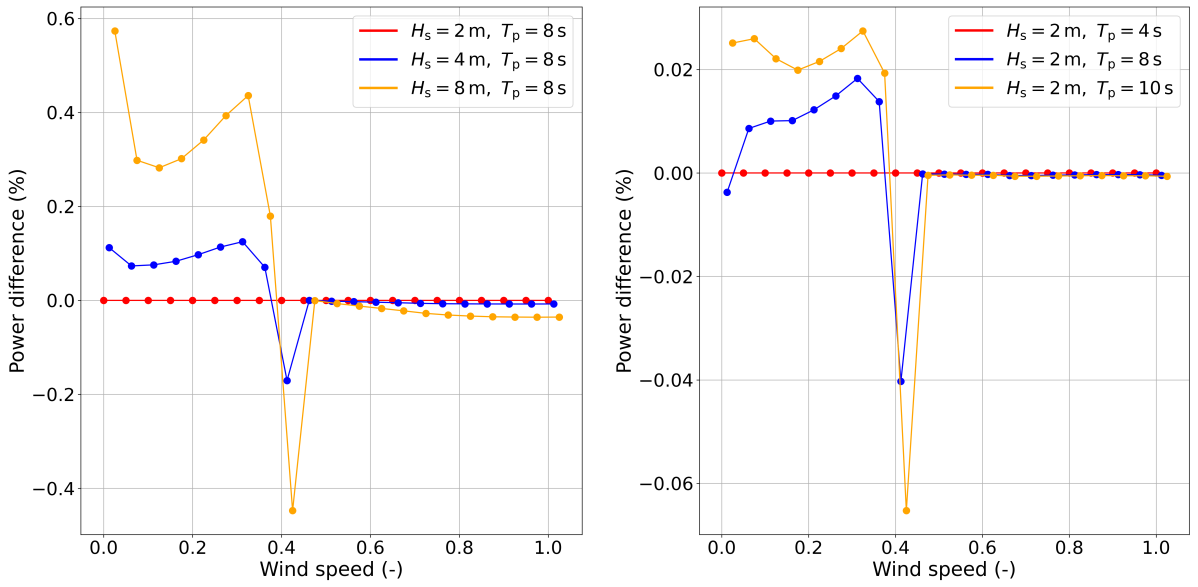

(a) Generated power difference for increasing H_s

(b) Generated power difference for increasing T_p

Figure 7.6: Comparison between generated power for different significant wave heights (a) and wave periods (b).

The effect on the AEP in the case of different wave heights with $T_p = 8$ s translates to a negligible difference of 0.01% and 0.06% for $H_s = 4$ m and $H_s = 8$ m, respectively, compared to $H_s = 2$ m. When investigating the influence of the wave period with a constant wave height of $H_s = 2$ m, both wave periods of $T_p = 8$ s and $T_p = 10$ s lead to an insignificant increase in AEP of less than 0.01% when compared to $T_p = 4$ s. It should be noted that this AEP estimation is purely for comparison purposes, as it is based on steady winds coming from $0°$, with waves and currents aligned in the same direction.

7.1.3. Wind-wave directionality

After investigating the effect of different sea states on response and power output, the influence of wind-wave directionality is now considered. For a steady wind speed of 8 m/s coming from 0° and irregular waves with a period of $T_p = 8$ s coming from directions (0°, 30°, 60°, 90°, 120°), along with two different significant wave heights $H_s = 2, 4$ m, the results are compared. The comparison is made with the case of no wind-wave misalignment and the difference in generated power is presented in Figure 7.7.

It is evident that the reduction in power increases as the wind-wave misalignment increases. When wind and waves are aligned, the maximum power is produced because the wave forces the floating platform to move along the wind direction. On the other hand, as the wind-wave misalignment increases, the waves tend to be perpendicular to the wind, exciting sway and roll motions. However, these motions have a minor effect on the generated power. This trend is observed for both wave heights. Similar results have been also found by Fontanella et al. (2023). To summarise, an increase in wind-wave misalignment has a negative effect on the generated power.

7.2. Impact of currents

The effect of currents on motion and power production was examined for three different current velocities, $U_{current} = 0.1$ m/s, $U_{current} = 0.5$ m/s and $U_{current} = 0.8$ m/s. For the simulation of waves, the representative significant wave height $H_s = 2$ m and wave period $T_p = 8$ s were adopted. The results for surge and pitch motions are shown in Figure 7.8a and Figure 7.8b, respectively.

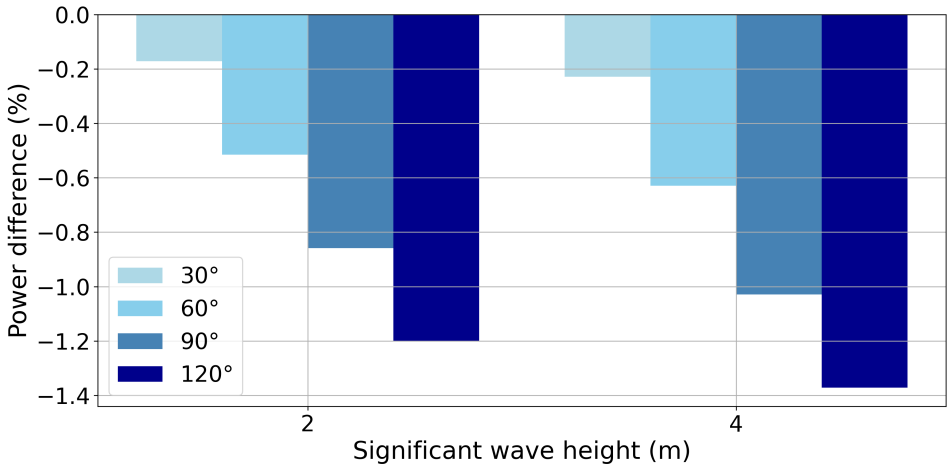

Figure 7.7: Comparison of difference in generated power due to irregular waves with a frequency of 0.125 Hz at a wind speed of 8 m/s, with four values of the wind-wave misalignment angle (30°, 60°, 90°and 120°). For comparison, the reference power is defined as the power produced with no wind-wave misalignment.

Similar to the trend observed in waves, surge and pitch reach their maximum values at the rated wind speed and then decrease. However, in waves, the mean values were approximately the same for the different wave heights and periods. In the case of currents, there is more than a 0.3 normalised difference in surge between the different current speeds, with the current having the greatest velocity causing the highest surge amplitude. For pitch motion, the opposite is true, where the current with the lowest velocity causes the highest pitch. The difference in pitch for each wind speed is about 0.2 in normalised values. The explanation for this is similar to waves: as the current flows toward the surge direction, the TetraSpar demonstrator is subjected to increased hydrodynamic forces. This generates a counteracting moment that reduces some of the wind-induced moments around the center of rotation of the floating platform. This opposing torque mitigates the aerodynamic torque created by rising wind speeds, leading to a reduction in the platform's pitch. As far as the standard deviations are concerned, they are smaller compared to the waves.

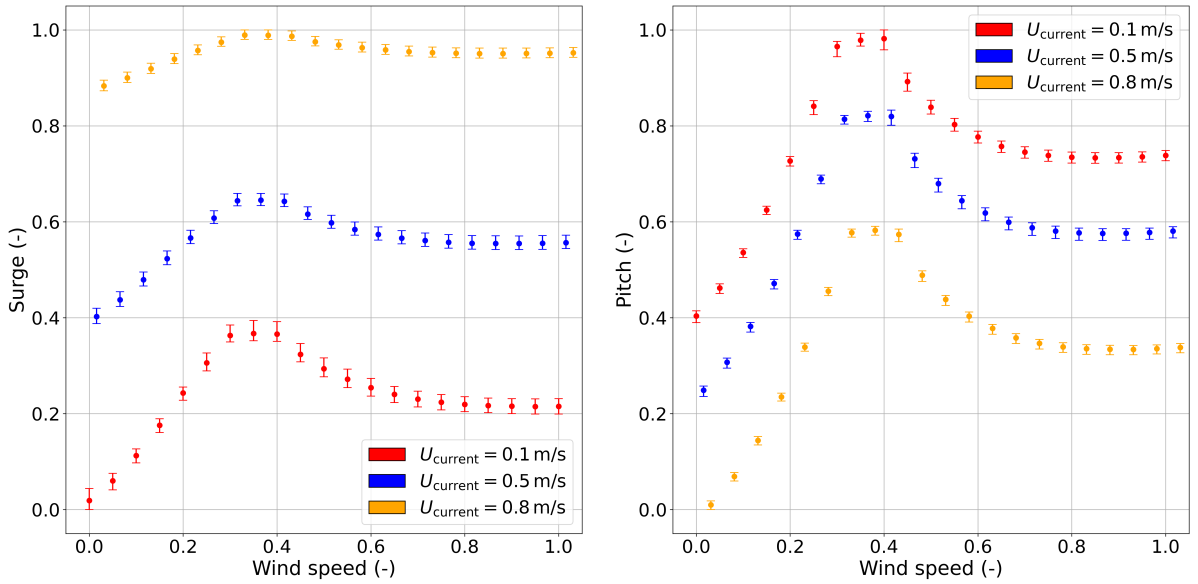

(a) Platform surge statistical analysis

(b) Platform pitch statistical analysis

Figure 7.8: Statistical analysis of platform surge (a) and pitch (b) for sub-surface current speed of 0.1 m/s, 0.5 m/s and 0.8 m/s.

As far as the generated power is concerned, it is evident from Figure 7.9 that the current with higher velocity generates more mean power due to the reduced pitch platform motion in the below rated region.

In the above rated region, there is no difference in the generated power. The standard deviations are approximately the same for all current velocities. The effect on the AEP based on the difference in generated power (Figure 7.9b) corresponds to 0.4% and 0.78% for $U_{\text{current}} = 0.5\,\text{m/s}$ and $U_{\text{current}} = 0.8\,\text{m/s}$, respectively, when compared to $U_{\text{current}} = 0.1\,\text{m/s}$. An overview of the influence on the AEP of significant wave height and period described in subsection 7.1.2, and the current velocity is presented in Figure 7.10. It is clear that current velocity has the greatest effect on the AEP, while the influence of wave period is the smallest compared to wave height and current velocity.

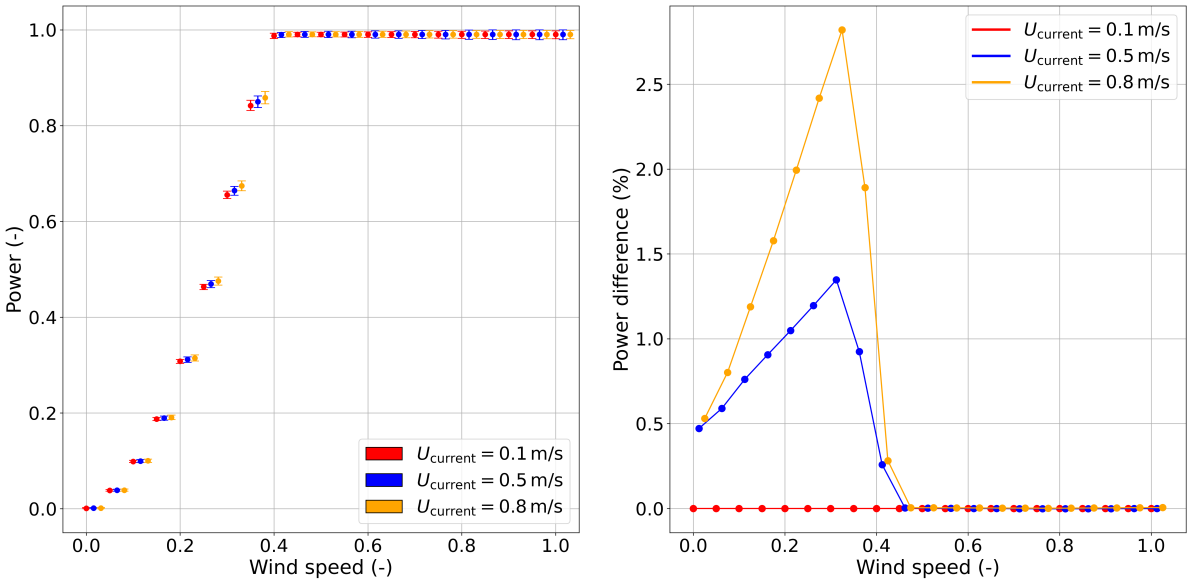

(a) Generated power statistical analysis

(b) Generated power difference

Figure 7.9: Statistical analysis (a) and difference in generated power (b) for sub-surface current speed of 0.1 m/s, 0.5 m/s and 0.8 m/s.

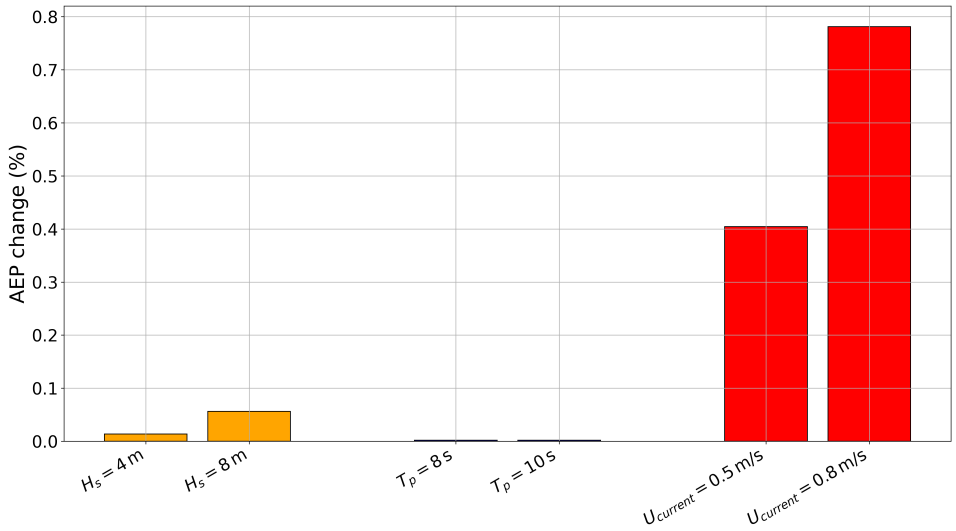

Figure 7.10: Comparison of AEP change for different wave heights (H_s) with $T_\text{p} = 8\,\text{s}$, wave periods (T_p) with $H_\text{s} = 2\,\text{m}$ and current velocities (U_current) with respect to the reference cases, which are those with $H_\text{s} = 2\,\text{m}$, $T_\text{p} = 4\,\text{s}$ and $U_\text{current} = 0.1\,\text{m/s}$.

To sum up, the effect of currents on surge and pitch motions is similar to that of waves, with an increase until the rated wind speed and then a decrease. However, there is a significant difference in the mean values. For power, the mean values and standard deviations follow the pattern observed with waves, with higher current velocities producing more power due to reduced pitch motion.

8

Conclusions and recommendations

In this chapter, the main conclusions of this project are summarised in section 8.1, while in section 8.2 recommendations for further improvements are presented.

8.1. Conclusions

The main purpose of this report was to investigate the power performance of the TetraSpar demonstrator. The TetraSpar demonstrator is a floating offshore wind turbine platform consisting of ten cylinders that form the floater and three for the keel. The keel and floater are connected by six suspension lines. The cylinders create a tetrahedral shape and are anchored to the seabed using three catenary mooring lines. For power generation, a 3.6 MW wind turbine with a 130 m rotor radius is mounted on the top.

In order to do this, a model of the TetraSpar was developed using the open-source software OpenFAST. The modelling was based on proprietary data provided by RWE and by scaling the unknown parameters, especially for the wind turbine, based on the NREL 5 MW wind turbine. To begin with, the tower was modelled with eleven nodes in AeroDyn, while their structural properties, based on internal data, were entered in the ElastoDyn module. In addition, the open-source software BModes was utilised to estimate the first and second fore-aft and side-to-side mode shapes. For the modelling of the blades, the structural properties adopted in OpenFAST were based on internal data, and edgewise and flapwise natural mode shapes were estimated based on similar procedure followed for the tower. The uncertainties regarding the airfoils used in the 3.6 MW wind turbine led to the decision to use the same airfoils as the NREL 5 MW wind turbine, with adjustments on blade distribution to cover the 65 m length instead of the 63 m in the 5 MW wind turbine. In addition, the ROSCO controller was employed in this project due to the unavailability of information about the controller used in the on-site demonstrator. The controller, apart from the typical torque and pitch control used in fixed-bottom wind turbines, was tuned with peak shaving and floating feedback techniques that are implemented in FOWTs. For the modelling of the floating platform and mooring lines, the uncertainties were less compared to the wind turbine. The entire platform was treated as a rigid body with six degrees of freedom using the strip theory. For the modelling of the mooring system, the MoorDyn module was employed, where the different segments of each mooring line were defined.

For the purpose of comparing the OpenFAST model with the on-site demonstrator, various data were provided by RWE at a frequency of 25 Hz. The relevant data for this project, such as those related to wind, waves, currents, motions and power generation, were further handled and averaged over 10-minute periods for an entire year. The year used as reference is 2023. In addition, they were further processed to match the differences that arise from the different coordinate systems of the OpenFAST and the on-site location.

Next, the model was tested under one-hour simulations for cut-in, below rated and above rated region. For the inputs in OpenFAST, the same 10-minute average conditions as the on-site data were used. Based on the time series results and power spectral densities, the rotational motions were

simulated better than the translational motions. As far as the generated power is concerned, the model underestimated the mean generated power in the cut-in and below rated regions, while there was agreement in the above rated region.

Following this, to construct the power curve and estimate AEP, the wind speed probability distribution for each wind speed in the operating region of the wind turbine was found. In addition, for each wind speed, the representative wind direction, significant wave height, wave period, etc., were determined by categorising these data in bins and estimating the number of occurrences. As a result, the most representative conditions were found for each wind speed. Running OpenFAST simulations with an 80% peak shaving level for each wind speed, the power was estimated and compared to the on-site power curve. The highest differences were observed near the cut-in region and near the rated wind speed. The AEP estimation for the model showed an underestimation of 2.8% compared to the on-site measurement.

The effect of different peak shaving levels was also investigated by comparing peak shaving levels of 75%, 80%, 90% and without peak shaving. The results revealed that the scenario with 75% showed the largest difference in AEP compared to on-site measurements, at 4.4%. For all the other cases, the underestimation in AEP was between 2.1% and 2.8%. Furthermore, if no wind speed estimator was implemented in the case of 80%, there was a decrease in AEP by 1%.

To compare the response of the floating platform between the model and on-site data under average conditions, the magnitude of roll and pitch motions was analysed. The magnitude is independent of the different wind directionality in the average data. Overall, the same general trend was observed for all peak shaving levels, with underestimation of mean roll and pitch magnitude in the below rated region. After the rated region, where the magnitude reaches its maximum values, the on-site data showed a gradual reduction, but for the model, it decreases until the middle of the above rated region and then remains constant. As far as the standard deviation is concerned, it increases until the rated wind speed and then abruptly decreases, remaining almost constant for the above rated region.

To investigate solely the surge and pitch motions, OpenFAST simulations with average conditions were performed, but with wind propagation direction along the x-axis to excite only these two motions. The model slightly underestimated the surge amplitude, but the general trend was the same. For pitch motion, there was good agreement in the below rated region and an overestimation in the above rated region.

Furthermore, the effect of metocean conditions on the motion of the TetraSpar demonstrator was examined. For this purpose, platform pitch and surge motions under different wave heights and periods were analysed, along with the effect of current velocity. Regarding the wave effect, it was found that increasing wave heights and larger periods led to similar results, with higher mean values for platform surge and standard deviation. On the other hand, for pitch motion, higher mean values were observed for low wave heights and periods, while the standard deviations were similar to those of surge. Overall, the general trend for both motions showed an increase until the rated wind speed, followed by a reduction and stabilisation in the mid-range of the above rated region. As far as generated power is concerned, the mean values slightly increased in the below rated region while in the above rated region the difference was insignificant, compared to the case with the lowest wave height and wave period. Furthermore, the standard deviations were larger for higher waves and periods. The effect of current velocity on the motions followed the same trend but showed a greater difference in mean values, while the standard deviations were smaller compared to those caused by waves. Higher current velocity also led to a slightly improved mean power generation, due to the reduced pitch motion.

Lastly, the wind-wave misalignment effect on power generation was examined. The results showed that maximum power is produced when wind and waves are aligned and an increase in misalignment angle has a negative effect on the generated power. Additionally, the higher the wave height, the greater the reduction in power generation as the misalignment angle increases.

8.2. Recommendations

The developed model can serve as a valuable tool for estimating the response and power production of the TetraSpar demonstrator. However, further improvements could be implemented to enhance the

model's accuracy.

Firstly, for a more accurate AEP estimation and response of the floating platform, it is advised to use as much the on-site wind turbine data as possible, which were not available due to confidentiality. The most important missing data were those related to the rotor performance, such as the airfoils and information about the controller. In addition, an optimisation of energy production and load reduction when tuning the controller could also be investigated. Extensive knowledge of these could enhance the precision of the model.

Secondly, instead of strip theory, the potential flow theory could be implemented, which was excluded due to time constraints and the need for third-party software. By using the potential flow theory, the limitations of strip theory, such as the lack of second-order hydrodynamic phenomena, could be overcome. Adopting this theory in the model and comparing it with the existing one could also lead to a better understanding of power performance and platform motion. Additionally, it is advised to model the floating platform in OpenFAST as a flexible structure. This approach would also be helpful in load estimation at connection points, if needed.

Thirdly, to further investigate the influence of metocean conditions, waves and currents, additional simulations could be performed for a wider range of significant wave heights, periods and current velocities to further validate the results with existing test cases.

Last but not least, regarding the weather conditions used in the simulation for modelling currents, it is advised to create a full current profile based on the current velocity and direction measurements at different depths. This could be achieved by recompiling OpenFAST. Moreover, the examination of different turbulence models is recommended for the generation of turbulent time series in OpenFAST, in order to investigate the influence of the wind time series on the AEP and the platform motion.

References

Abbas, N., Zalkind, D., Pao, L., & Wright, A. (2021). A reference open-source controller for fixed and floating offshore wind turbines. *Wind Energy Science Discussions*, *2021*, 1–33. https://doi.org/10.5194/wes-2021-19

Adiputra, R., Fauzi, F. N., Firdaus, N., Suyanto, E. M., Kasharjanto, A., Puryantini, N., Erwandi, E., Rasgianti, R., & Prabowo, A. R. (2023). Roundness and slenderness effects on the dynamic characteristics of spar-type floating offshore wind turbine. *Curved and Layered Structures*, *10*. https://doi.org/10.1515/cls-2022-0213

Barooni, M., Ashuri, T., Sogut, D. V., Wood, S., & Taleghani, S. G. (2023). Floating offshore wind turbines: Current status and future prospects. *Energies*, *16*. https://doi.org/10.3390/en16010002

Bir, G. (2005, December). *User's Guide to BModes (Software for Computing Rotating Beam Coupled Modes)* (tech. rep. No. Technical Report NREL/TP-500-39133). National Renewable Energy Laboratory.

Borg, M., Jensen, M. W., Urquhart, S., Andersen, M. T., Thomsen, J. B., & Stiesdal, H. (2020). Technical definition of the tetraspar demonstrator floating wind turbine foundation. *Energies*, *13*. https://doi.org/10.3390/en13184911

Byrne, B. W., & Houlsby, G. T. (2003). Foundations for offshore wind turbines. *Philosophical Transactions of the Royal Society of London. Series A: Mathematical, Physical and Engineering Sciences*, *361*(1813), 2909–2930. https://doi.org/10.1098/rsta.2003.1286

Collu, M., & Borg, M. (2016, January). *Design of floating offshore wind turbines*. https://doi.org/10.1016/b978-0-08-100779-2.00011-8

Cradden, L., Weywada, P. L., & Atcheson, M. (2016, January). *The offshore environment*. https://doi.org/10.1007/978-3-319-29398-1_2

Edwards, E. C., Holcombe, A., Brown, S., Ransley, E., Hann, M., & Greaves, D. (2023). Evolution of floating offshore wind platforms: A review of at-sea devices. *Renewable and Sustainable Energy Reviews*, *183*. https://doi.org/10.1016/j.rser.2023.113416

Farrugia, R., Sant, T., & Micallef, D. (2016). A study on the aerodynamics of a floating wind turbine rotor. *Renewable Energy*, *86*, 770–784. https://doi.org/10.1016/j.renene.2015.08.063

Fischer, T., De Vries, W., & Cordle, A. (2011). Executive summary (wp4: Offshore foundations and support structures).

Fontanella, A., Colpani, G., De Pascali, M., Muggiasca, S., & Belloli, M. (2023). Assessing the impact of waves and platform dynamics on floating wind turbine energy production. *Wind Energy Science Discussions*, *2023*, 1–33.

Garcia-Sagrado, A., Schlipf, D., Brovia, S. P., Burstein, J., & Yoshinaga, T. (2024). Impact of motions on floating wind turbine power production. *Journal of Physics: Conference Series*, *2767*(6), 062034.

GWEC. (2023a, March). Global Wind Report 2023. https://gwec.net/globalwindreport2023/

GWEC. (2023b, August). Global Offshore Wind Report 2023. https://gwec.net/gwecs-global-offshore-wind-report-2023/

Hall, M. (2015, December). *MoorDyn User's Guide* (tech. rep.). https://www.nrel.gov/wind/nwtc/assets/downloads/InflowWind/InflowWind_Manual.pdf

Huang, Y., & Wan, D. (2020). Investigation of interference effects between wind turbine and spar-type floating platform under combined wind-wave excitation. *Sustainability (Switzerland)*, *12*. https://doi.org/10.3390/SU12010246

Johlas, H. M., Martínez-Tossas, L. A., Churchfield, M. J., Lackner, M. A., & Schmidt, D. P. (2021). Floating platform effects on power generation in spar and semisubmersible wind turbines. *Wind Energy*, *24*, 901–916. https://doi.org/10.1002/we.2608

Jonkman, J., Butterfield, S., Musial, W., & Scott, G. (2009, February). *Definition of a 5-MW Reference Wind Turbine for Offshore System Development* (tech. rep. No. Technical Report

NREL/TP-500-38060). Golden, us, National Renewable Energy Laboratory. https://www.nrel.gov/docs/fy09osti/38060.pdf

Jonkman, J., Branlard, E., Hall, M., Hayman, G., Platt, A., & Robertson, A. (2020, August). *Implementation of substructure flexibility and Member-Level load capabilities for floating offshore wind turbines in OpenFAST* (tech. rep.). https://doi.org/10.2172/1665796

Karimirad, M., Moan, T., & Asce, F. (2012). Wave-and wind-induced dynamic response of a spar-type offshore wind turbine. https://doi.org/10.1061/(ASCE)WW.1943-5460

Koh, J. H., & Ng, E. Y. (2016). Downwind offshore wind turbines: Opportunities, trends and technical challenges. *Renewable and Sustainable Energy Reviews*, *54*. https://doi.org/10.1016/j.rser.2015.10.096

Larsen, T. J., & Hanson, T. D. (2007). A method to avoid negative damped low frequent tower vibrations for a floating, pitch controlled wind turbine. *Journal of Physics: Conference Series*, *75*(1), 012073.

Leble, V., & Barakos, G. (2016). Forced pitch motion of wind turbines. *Journal of Physics: Conference Series*, *753*. https://doi.org/10.1088/1742-6596/753/2/022042

Lee, H., & Lee, D. J. (2019). Effects of platform motions on aerodynamic performance and unsteady wake evolution of a floating offshore wind turbine. *Renewable Energy*, *143*, 9–23. https://doi.org/10.1016/j.renene.2019.04.134

Lerch, M., De-Prada-Gil, M., & Molins, C. (2019). The influence of different wind and wave conditions on the energy yield and downtime of a spar-buoy floating wind turbine. *Renewable Energy*, *136*, 1–14. https://doi.org/10.1016/j.renene.2018.12.096

Liu, B., & Yu, J. (2022). Dynamic response of spar-type floating offshore wind turbine under wave group scenarios. *Energies*, *15*. https://doi.org/10.3390/en15134870

Lyu, G., Zhang, H., & Li, J. (2019). Effects of incident wind/wave directions on dynamic response of a spar-type floating offshore wind turbine system. *Acta Mechanica Sinica/Lixue Xuebao*, *35*, 954–963. https://doi.org/10.1007/s10409-019-00884-9

Matha, D., Cruz, J., Masciola, M., Bachynski, E. E., Atcheson, M., Goupee, A. J., Gueydon, S., & Robertson, A. (2016, January). *Modelling of floating offshore wind technologies*. https://doi.org/10.1007/978-3-319-29398-1_4

Micallef, D., & Rezaeiha, A. (2021). Floating offshore wind turbine aerodynamics: Trends and future challenges. *Renewable and Sustainable Energy Reviews*, *152*. https://doi.org/10.1016/j.rser.2021.111696

Moriarty, P., & Hansen, A. (2005, January). *AeroDyn Theory Manual* (tech. rep. No. NREL/TP-500-36881). Golden, Colorado, USA, National Renewable Energy Laboratory. https://www.nrel.gov/docs/fy05osti/36881.pdf

Musial, W., Butterfield, S., & Boone, A. (2004). Feasibility of floating platform systems for wind turbines. *42nd AIAA aerospace sciences meeting and exhibit*, 1007.

NREL. (2021). ROSCO. Version 2.4.1. https://github.com/NREL/ROSCO

NREL. (2024, January). OpenFAST. https://www.nrel.gov/wind/nwtc/openfast.html

O'Kelly, B. C., & Arshad, M. (2016, March). Offshore wind turbine foundations - analysis and design. Elsevier Inc. https://doi.org/10.1016/B978-0-08-100779-2.00020-9

Platt, A., Jonkman, B., & Jonkman, J. (2016, July). *InflowWind User's Guide* (tech. rep.). National Wind Technology Center. https://www.nrel.gov/wind/nwtc/assets/downloads/InflowWind/InflowWind_Manual.pdf

Plodpradit, P., Dinh, V. N., & Kim, K. D. (2019). Tripod-supported offshore wind turbines: Modal and coupled analysis and a parametric study using x-sea and fast. *Journal of Marine Science and Engineering*, *7*. https://doi.org/10.3390/jmse7060181

Ramponi, R., Amaral, R., & Vire, A. (2023). Investigation of the effect of prescribed coupled motions on the power production of a floating offshore wind turbine. *Journal of Physics: Conference Series*, *2626*. https://doi.org/10.1088/1742-6596/2626/1/012029

Schallenberg-Rodríguez, J., & Montesdeoca, N. G. (2018). Spatial planning to estimate the offshore wind energy potential in coastal regions and islands. practical case: The canary islands. *Energy*, *143*. https://doi.org/10.1016/j.energy.2017.10.084

Seidel, M. (2007). Jacket substructures for the repower 5m wind turbine. *European Offshore Wind 2007*, 1–8.

Shen, X., Chen, J., Hu, P., Zhu, X., & Du, Z. (2018). Study of the unsteady aerodynamics of floating wind turbines. *Energy*, *145*, 793–809. https://doi.org/10.1016/j.energy.2017.12.100

Singh, D., Haugen, E., Laugesen, K., Chauhan, A., & Viré, A. (2024). Data analysis of the tetraspar demonstrator measurements. *Journal of Physics: Conference Series*, *2767*(6), 062025.

Stiesdal. (2021). The TetraSpar Full-scale Demonstration Project. https://www.stiesdal.com/offshore/the-tetraspar-full-scale-demonstration-project/

Thomsen, J. B., Bergua, R., Jonkman, J., Robertson, A., Mendoza, N., Brown, C., Galinos, C., & Stiesdal, H. (2021). Modeling the tetraspar floating offshore wind turbine foundation as a flexible structure in orcaflex and openfast. *Energies*, *14*. https://doi.org/10.3390/en14237866

Tran, T. T., & Kim, D.-H. (2015). The platform pitching motion of floating offshore wind turbine: A preliminary unsteady aerodynamic analysis. *Journal of wind engineering and industrial aerodynamics*, *142*, 65–81. https://doi.org/10.1016/j.jweia.2015.03.009

Tumewu, Y., Crescenzo, P., & Sivaselvan, M. (2017). Numerical simulation of the influence of platform pitch motion on power generation steadiness in floating offshore wind turbines. *International Journal of Environmental Science & Sustainable Development.*, *2*, 92. https://doi.org/10.21625/essd.v1i2.39

United Nations. (2015). *Paris Agreement* (tech. rep.). https://unfccc.int/sites/default/files/english_paris_agreement.pdf

WAMIT, Inc. & Massachusetts Institute of Technology. (2023). *WAMIT User Manual Version 7.5* (tech. rep.). https://www.wamit.com/manual7.x/v75_manual.pdf

Wang, S., Xing, Y., Karuvathil, A., & Gaidai, O. (2023). A comparison study of power performance and extreme load effects of large 10-mw offshore wind turbines. *IET Renewable Power Generation*, *17*, 2195–2214. https://doi.org/10.1049/rpg2.12721

Wen, B., Dong, X., Tian, X., Peng, Z., Zhang, W., & Wei, K. (2018). The power performance of an offshore floating wind turbine in platform pitching motion. *Energy*, *154*, 508–521. https://doi.org/10.1016/j.energy.2018.04.140

Wen, B., Tian, X., Dong, X., Peng, Z., & Zhang, W. (2017). Influences of surge motion on the power and thrust characteristics of an offshore floating wind turbine. *Energy*, *141*, 2054–2068. https://doi.org/10.1016/j.energy.2017.11.090

Wiser, R., Rand, J., Seel, J., Beiter, P., Baker, E., Lantz, E., & Gilman, P. (2021). Expert elicitation survey predicts 37% to 49% declines in wind energy costs by 2050. *Nature Energy*, *6*(5), 555–565.

A

TetraSpar properties

Table A.1: Properties of the floater (Borg et al., 2020).

Item	Unit	Value
Floater mass including ballast water and additional components	(t)	1340
Floater vertical center of gravity wrt. MWL	(m)	-9.2
Distance from MWL to bottom of floater	(m)	16.0
Floater roll mass moment of inertia wrt. CoG	(kg·m^2)	4.425×10^8
Floater pitch mass moment of inertia wrt. CoG	(kg·m^2)	4.422×10^8
Floater yaw mass moment of inertia wrt. CoG	(kg·m^2)	5.322×10^8

Table A.2: Definition of components positions and dimensions (Borg et al., 2020).

Item	Unit	Value
Center column diameter	(m)	4.3
Center column equivalent length	(m)	30.6
Center column coordinates wrt. MWL	(m)	(0.0; 0.0; -14.6)–(0.0; 0.0; 16.0)
Radial brace diameter	(m)	3.5
Radial brace equivalent length	(m)	32.8
Radial brace node coordinates wrt. MWL	(m)	(2.5; 0.0; -14.0)–(35.3; 0.0; -14.0) (-1.2; 2.2; -14.0)–(-17.6; 30.6; -14.0) (-1.2; -2.2; -14.0)–(-17.6; -30.6; -14.0)
Diagonal brace diameter	(m)	2.2
Diagonal brace equivalent length	(m)	38.9
Diagonal brace node coordinates wrt. MWL	(m)	(3.1; 0.0; 14.1)–(32.4; 0.0; -11.5) (-1.5; 2.7; 14.1)–(-16.2; 28.0; -11.5) (-1.5; -2.7; 14.1)–(-16.2; -28.0; -11.5)
Lateral brace diameter	(m)	4.0
Lateral brace equivalent length	(m)	49.2
Lateral brace node coordinates wrt. MWL	(m)	(30.5; 3.5; -14.0)–(-12.2; 28.1; -14.0) (-18.3; 24.6; -14.0)–(-18.3; -24.6; -14.0) (-12.2; -28.1; -14.0)–(30.5; -3.5; -14.0)

Table A.3: Properties of the keel (Borg et al., 2020).

Item	Unit	Value
Keel mass including ballast water	(t)	3696
Vertical distance from MWL to keel horizontal centerline	(m)	64.0
Keel roll mass moment of inertia wrt. CoG	(kg·m^2)	1.443×10^9
Keel pitch mass moment of inertia wrt. CoG	(kg·m^2)	1.443×10^9
Keel yaw mass moment of inertia wrt. CoG	(kg·m^2)	2.878×10^9
Keel equivalent cylinder length	(m)	56.4
Keel cylinder diameter	(m)	4.1
Keel brace node coordinates wrt. MWL	(m)	(20.0; -28.2; -64.0)–(20.0; 28.2; -64.0) (14.4; 31.4; -64.0)–(-34.4; 3.2; -64.0) (-34.4; -3.2; -64.0)–(14.4; -31.4; -64.0)

Table A.4: Mechanical properties of suspension lines with fairlead coordinates and line connectivity (Borg et al., 2020).

Item	Unit	Value
Linetype	(-)	Synthetic rope bundle
Buoyancy diameter	(mm)	119.0
Unstretched length	(m)	60.0
Submerged mass	(kg / m)	-0.44
Dry mass	(kg / m)	11.0
Axial stiffness	(kN)	506,667.0
Floater suspension (FS) fairlead coordinates (wrt. MWL)		
FS1	(m)	(35.6; -1.2; -15.8)
FS2	(m)	(-16.8; -31.5; -15.8)
FS3	(m)	(-18.8; -30.3; -15.8)
FS4	(m)	(-18.8; 30.3; -15.8)
FS5	(m)	(-16.8; 31.4; -15.8)
FS6	(m)	(35.6; 1.2; -15.8)
Keel fairlead (KF) coordinates (wrt. MWL)		
KF1	(m)	(19.8; -32.7; -64.0)
KF2	(m)	(18.4; -33.5; -64.0)
KF3	(m)	(-38.2; -0.8; -64.0)
KF4	(m)	(-38.2; 0.8; -64.0)
KF5	(m)	(18.4; 33.5; -64.0)
KF6	(m)	(19.8; 32.7; -64.0)
Connectivity		
Suspension line 1		FS1-KF1
Suspension line 2		FS2-KF2
Suspension line 3		FS3-KF3
Suspension line 4		FS4-KF4
Suspension line 5		FS5-KF5
Suspension line 6		FS6-KF6

Table A.5: Mooring system description (Borg et al., 2020).

Item	Unit	Value
Anchor radius	(m)	630.0
Anchor node coordinates wrt. MWL	(m)	(630.0; 0.0; -220.0) (-215.5; -592.0; -220.0) (-315.0; 545.6; -220.0)
Mooring fairlead node coordinates wrt. MWL	(m)	(36.3; 0.0; -12.4) (-18.1; -31.4; -12.4) (-18.1; 31.4; -12.4)
Segment lengths of each mooring line		
Fairlead	(-)	
Linetype1	(m)	80.0
Linetype2	(m)	6.0
Linetype1	(m)	140.0
Linetype3	(m)	145.5
Linetype4	(m)	30.0
Linetype2	(m)	270.0
Anchor	(-)	

Table A.6: Mechanical properties of the mooring system line types (Borg et al., 2020).

Item	Unit	Value	Linetype
Buoyancy diameter	(mm)	108.0	
Submerged weight	(N / m)	2.2	Synthetic rope (Linetype1)
Axial stiffness	(kN)	4.45×10^5	
Buoyancy diameter	(mm)	202	
Submerged weight	(N / m)	2139.6	Mooring chain (Linetype2)
Axial stiffness	(kN)	1.15×10^6	
Buoyancy diameter	(mm)	234	
Submerged weight	(N / m)	2872.0	Mooring chain (Linetype3)
Axial stiffness	(kN)	1.55×10^6	
Buoyancy diameter	(mm)	698	
Submerged weight	(N / m)	19,515.0	Mooring chain with clump weights (Linetype4)
Axial stiffness	(kN)	1.06×10^6	

B

OpenFAST simulation results

B.1. Free decay results

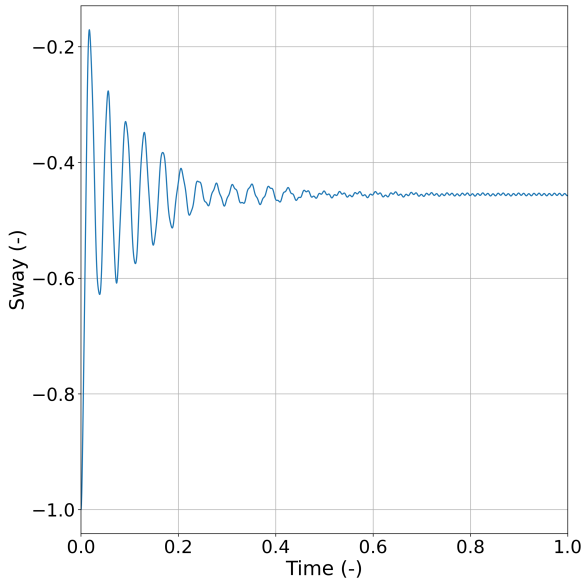

(a) Platform sway free decay time series

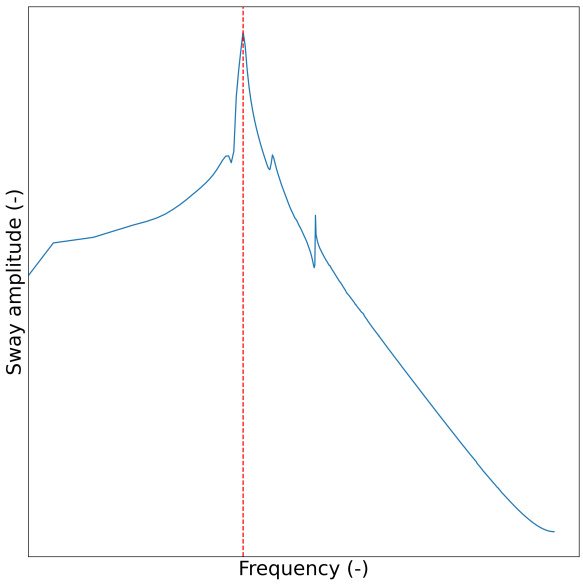

(b) Platform sway free decay in frequency domain

Figure B.1: Normalised platform sway free decay time series (a) and frequency domain representation (b), where the red dashed line indicates the natural frequency of sway motion.

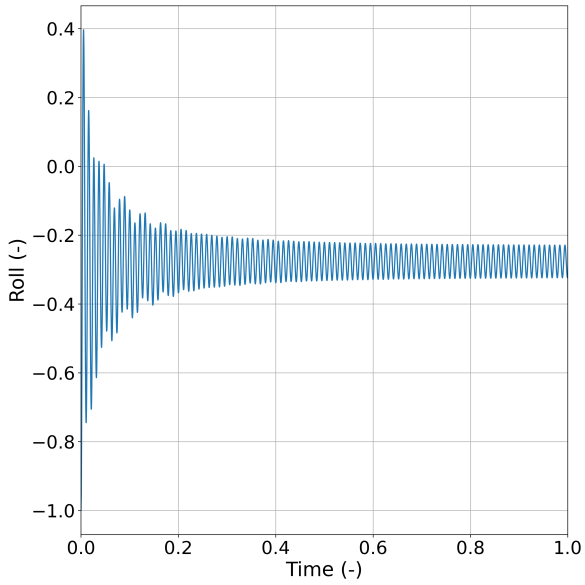

(a) Platform roll free decay time series

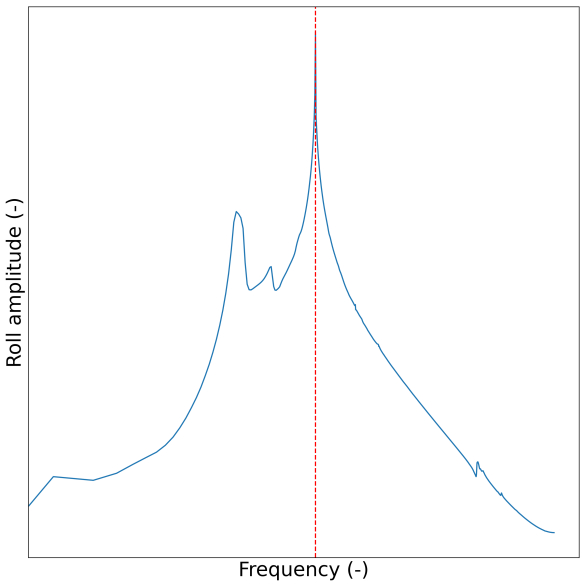

(b) Platform roll free decay in frequency domain

Figure B.2: Normalised platform roll free decay time series (a) and frequency domain representation (b), where the red dashed line indicates the natural frequency of roll motion.

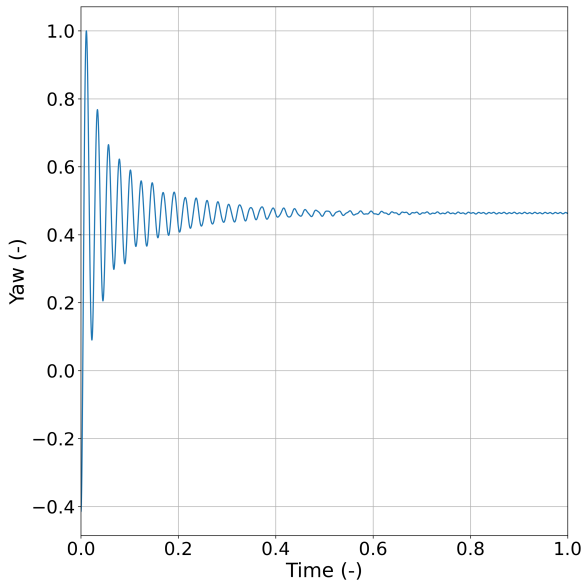

(a) Platform yaw free decay time series

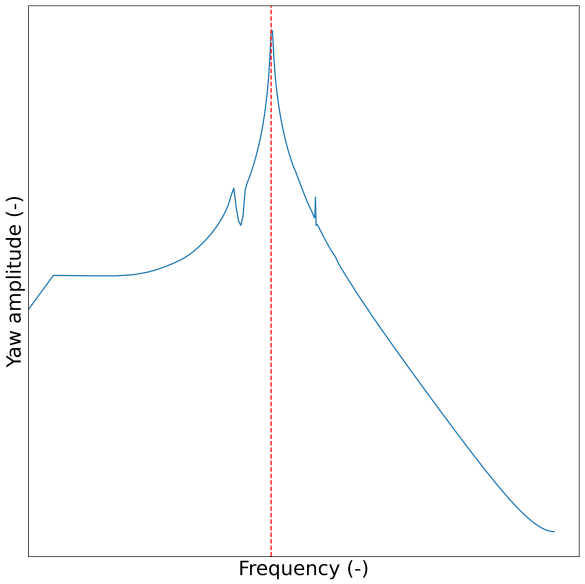

(b) Platform yaw free decay in frequency domain

Figure B.3: Normalised platform yaw free decay time series (a) and frequency domain representation (b), where the red dashed line indicates the natural frequency of yaw motion.

B.2. One-hour simulation results

B.2.1. Cut-in region

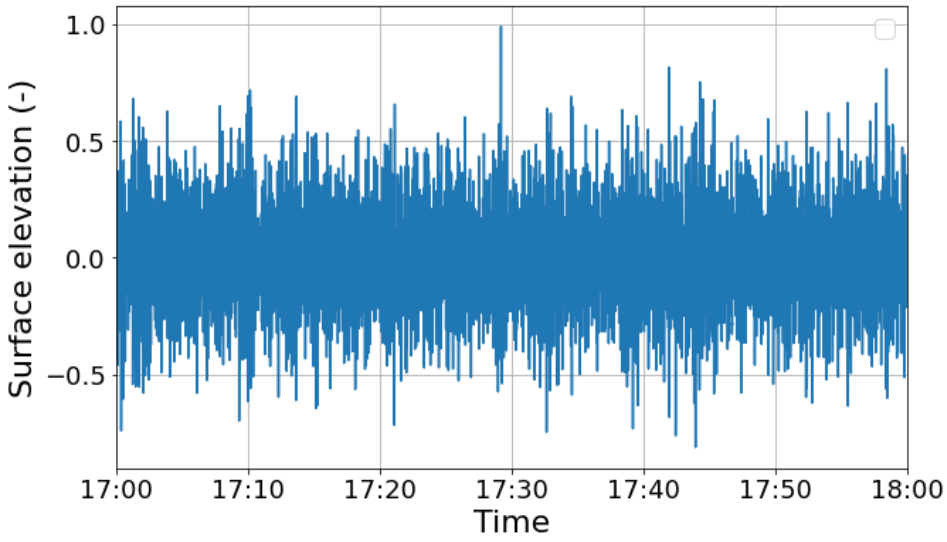

Figure B.4: Wave elevation time series used in cut-in region.

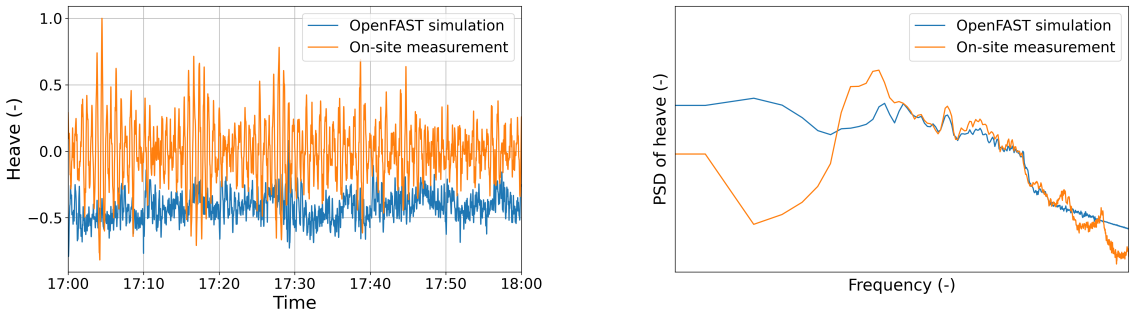

(a) Normalised heave time series

(b) Power spectral density of heave

Figure B.5: Comparison of normalised platform heave time series (a) and power spectral density (b) between OpenFAST and on-site measurement in cut-in region.

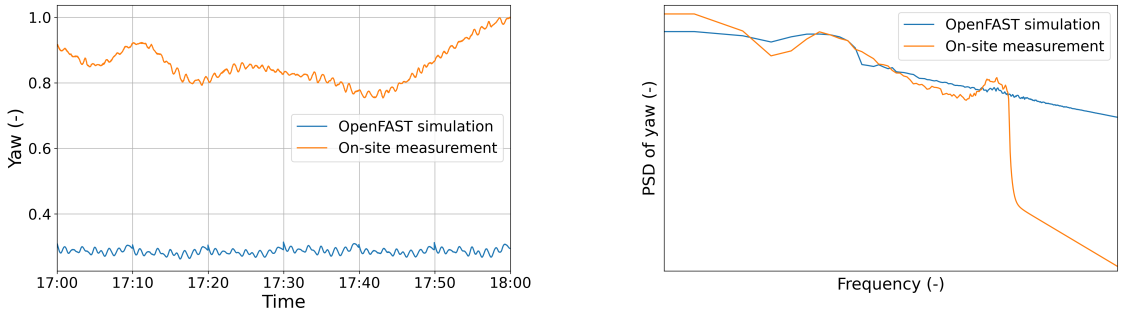

(a) Normalised yaw time series

(b) Power spectral density of yaw

Figure B.6: Comparison of normalised platform yaw time series (a) and power spectral density (b) between OpenFAST and on-site measurement in cut-in region.

B.2.2. Below rated region

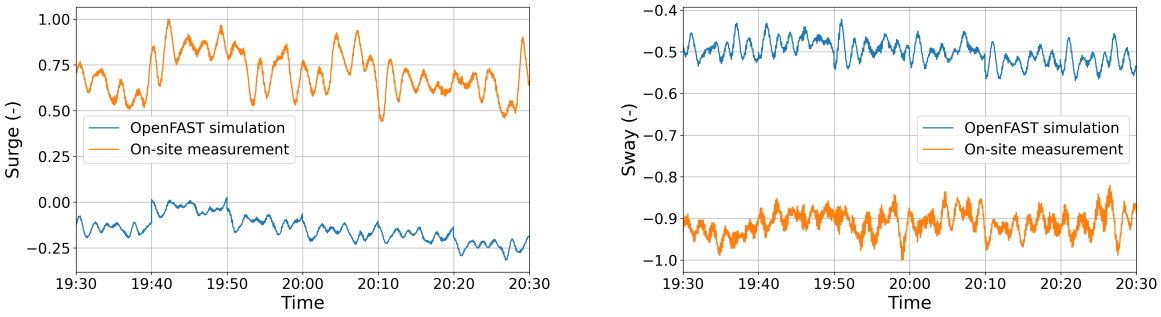

(a) Normalised surge time series

(b) Normalised sway time series

Figure B.7: Comparison of normalised platform surge (a) and sway time series (b) between OpenFAST and on-site measurement in below rated region.

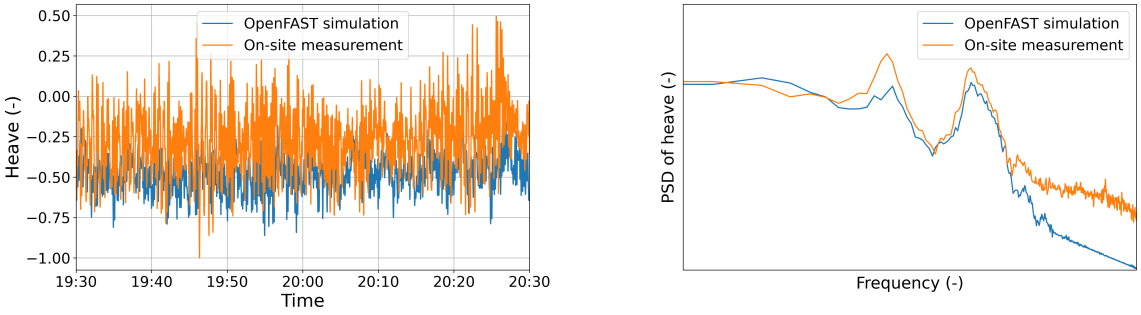

(a) Normalised heave time series

(b) Power spectral density of heave

Figure B.8: Comparison of normalised platform heave time series (a) and power spectral density (b) between OpenFAST and on-site measurement in below rated region.

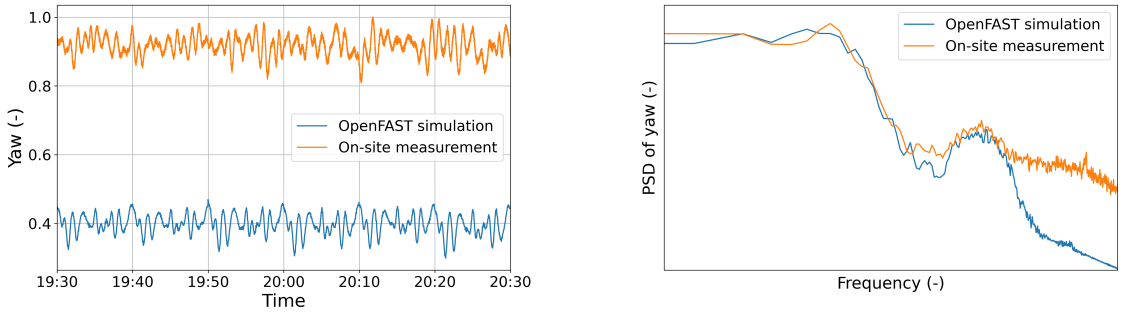

(a) Normalised yaw time series

(b) Power spectral density of yaw

Figure B.9: Comparison of normalised platform yaw time series (a) and power spectral density (b) between OpenFAST and on-site measurement in below rated region.

B.2.3. Above rated region

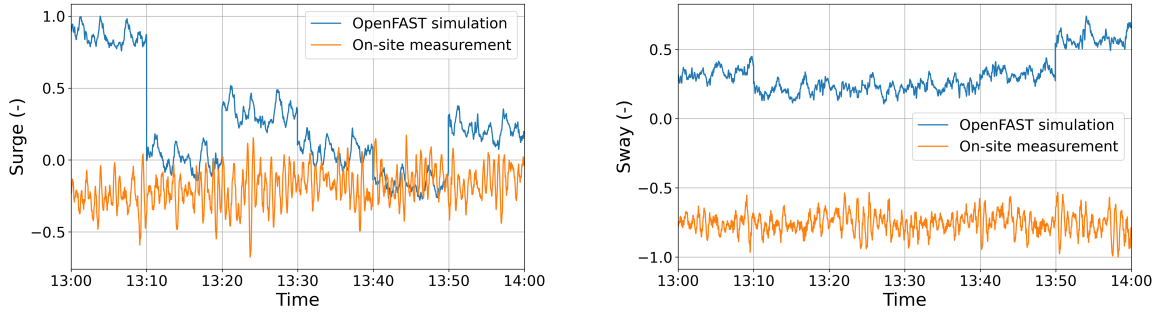

(a) Normalised surge time series

(b) Normalised sway time series

Figure B.10: Comparison of normalised platform surge (a) and sway time series (b) between OpenFAST and on-site measurement in above rated region.

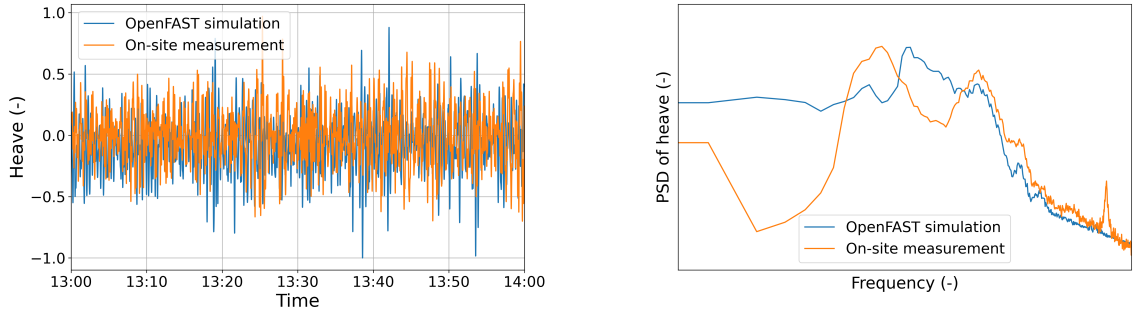

(a) Normalised heave time series

(b) Power spectral density of heave

Figure B.11: Comparison of normalised platform heave time series (a) and power spectral density (b) between OpenFAST and on-site measurement in above rated region.